ANNUAL REPORT

Center for Experimental Nuclear Physics and Astrophysics
University of Washington
May, 2005

Sponsored in part by the United States Department of Energy
under Grant #DE-FG02-97ER41020/A000.

Cover photos, clockwise from upper right: John Orrell assembling a Ge detector. The 21-fold symmetric short-range force pendulum. Tom Burritt with the wire frame for the KATRIN pre-spectrometer electrode.

INTRODUCTION

CENPA pursues a broad program of research in nuclear physics, astrophysics and related fields. Research activities are conducted locally and at remote sites. CENPA is a mojor participant in the Sudbury Neutino Observatory (SNO) and the KATRIN triuium experiment. The current program includes "in-house" research on nuclear collisions and fundamental interactions using the local tandem Van de Graaff, as well as local and remote non-accelerator research on fundamental interactions and user-mode research on relativistic heavy ions at large accelerator facilities in the U.S. and Europe.

Analysis of the complete 391-day data set with salt dissolved in the heavy water of the SNO detector to enhance its sensitivity to neutral-current interactions was carried out. Submission of the results in SNO's first long physics paper took place in February 2005. The neutral-current data directly constrain the mixing angle θ_{12}, which was found to be 33.9 ± 1.6^o for $\theta_{13} = 0$.

Limits on the solar antineutrino flux were derived using SNO's unique signature of two neutrons and a positron from the inverse beta decay of the deuteron. Less than 1% of the higher-energy ^{8}B flux is converted to antineutrinos. The limits, published in 2004, are comparable to ones obtained from SuperKamiokande and KamLAND.

Completion of the installation in SNO of the Neutral-Current Detector (NCD) array built at UW took place in 2004, and production data-taking with it began November 25. The array is performing well, with good sensitivity and low background.

The Data-Acquisition system for SNO has now been expanded to an integrated system that serves both the PMT array and the NCD array, providing "built" events for the two detector array separately and together. The new UW "ORCA" real-time code is now in successful use not only in SNO but also in the KATRIN prespectrometer data-acquisition system, in the ^{8}B decay experiment, and in a number of test stands.

Construction of an intricate internal grid assembly for the KATRIN prespectrometer was completed and the grid delivered to Germany in time for installation in the prespectrometer. The grid serves to suppress cosmic-ray and radioactivity generated backgrounds from the walls of the vessel.

We have successfully demonstrated the operation of a naked germanium detector in a bath of liquid argon. Scintillation light from the argon bath serves as a Compton veto. This technology is under consideration for use by the Majorana experiment and as a tool for low background counting.

Development of the tools needed for performing the full data analysis and for studying potential systematic uncertainties of the emiT data set are nearing completion. We expect to publish results before the end of the year.

With respect to our experiment to use ultra-cold neutrons (UCN) for measuring with precision the correlation parameters from polarized neutron beta decay, we have designed and built a modification for the UCN source. We expect this to bring an order-of-magnitude increase in UCN flux. We have also determined the properties of UCN detectors that were

designed in Seattle in an experiment at ILL. Our detectors showed good efficiency for detecting UCN in the range down to velocities of approximately two meters per second. These detectors will be critical to assess potential spin-dependent flux asymmetries that could bias our experiment.

Our experiment at Jyväskylä, Finland, to determine the efficiency of a potential neutrino detector made of ^{100}Mo was successful and the data analysis is well under way. Preliminary numbers indicate the neutrino absorption cross section is significantly higher than previously thought.

We have determined the mass of the lowest T=2 state in ^{32}S with the unprecedented precision of $\sim$ 0.3 keV. This will allow for the most precise test of the Isobaric Multiplet Mass Equation.

In our ^{3}He$(\alpha,\gamma)^7$Be project, we have constructed most of the needed apparatus, reduced the backgrounds, made a preliminary measurement at $E_\alpha = 3$ MeV, and we are now preparing to begin accurate cross section measurements. We have also done some additional calculations that add confidence in our $\pm$ 3% extrapolation uncertainty estimate for the ^{7}Be(p,γ)^{8}B astrophysical S-factor.

We have made substantial progress in testing the gravitational inverse-square law using a new pendulum with 21-fold rotational symmetry. This has greater sensitivity to new short-range interactions and substantially reduced noise compared to our published work. We have taken data at separations as small as 65 μm with enough sensitivity to see gravitational-strength interactions with Yukawa ranges $\lambda > 80\mu$m. Unexplained signals for separations smaller than 100 μm are being investigated.

Our search for CPT-violating preferred-frame effects using a "spendulum" containing 10^{23} polarized electrons continues to improve. Our current sensitivity for the Lorentz-violating Kostelecky $\tilde{b}$ parameters has reached 4×10^{-31} GeV.

Our correlation analysis of p-p and Au-Au data from RHIC has produced the first two-particle parton fragment distributions on transverse rapidity and the first measurement of fragment angular correlations and corresponding fragment j_t and k_t distributions *vs* Q^2 for very low-Q^2 partons. We have studied low-Q^2 parton dissipation in the form of minijet angular deformation *vs* centrality in Au-Au collisions, and inversion of mean transverse momentum $\langle p_t \rangle$ fluctuation scale dependence to p_t autocorrelations. Those autocorrelations provide evidence for recoil of the bulk medium in the more central Au-Au collisions responding to semi-hard parton scattering. Measurement of the collision energy dependence of $\langle p_t \rangle$ fluctuations from 10-200 GeV per nucleon suggests the onset of detectable parton scattering and fragmentation at an N-N CM energy of about 10 GeV.

In RHIC collisions, formation of a quark-gluon plasma in the early stages is expected to result in a large fireball that emits pions over an extended time period, while HBT interferometry analysis has been interpreted as indicating a relatively small unexpanded source with a very short pion emission duration. Work in our laboratory published in PRL has solved this "RHIC HBT Puzzle" by including a deep attractive potential based on chiral symmetry restoration, which causes pions in the hot dense medium to lose most of their mass. This

distorts the HBT "view" of the fireball, making the source appear smaller and making the pion emission appear to be of shorter duration.

A proposal has been developed and submitted to the NSF for a conceptual study of developing the U.S. Deep Underground Science and Engineering Laboratory near Leavenworth, WA.

As always, we encourage outside applications for the use of our facilities. As a convenient reference for potential users, the table on the following page lists the capabilities of our accelerators. For further information, please contact Prof. Derek W. Storm, Executive Director, CENPA, Box 354290, University of Washington, Seattle, WA 98195; (206) 543-4080, or storm@npl.washington.edu. Further information is also available on our web page: http://www.npl.washington.edu.

We close this introduction with a reminder that the articles in this report describe work in progress and are not to be regarded as publications or to be quoted without permission of the authors. In each article the names of the investigators are listed alphabetically, with the primary author underlined, to whom inquiries should be addressed.

Derek Storm, Editor Barbara Fulton, Assistant Editor

TANDEM VAN DE GRAAFF ACCELERATOR

A High Voltage Engineering Corporation Model FN purchased in 1966 with NSF funds, operation funded primarily by the U.S. Department of Energy. See W. G. Weitkamp and F. H. Schmidt, "The University of Washington Three Stage Van de Graaff Accelerator," Nucl. Instrum. Meth. **122**, 65 (1974). Recently adapted to an (optional) terminal ion source and a non-inclined tube #3, which enables the accelerator to produce high intensity beams of helium and hydrogen isotopes at energies from 100 keV to 5.5 MeV.

Some Available Energy Analyzed Beams

Ion	Max. Current (particle μA)	Max. Energy (MeV)	Ion Source
^{1}H or ^{2}H	50	18	DEIS or 860
^{3}He or ^{4}He	2	27	Double Charge-Exchange Source
^{3}He or ^{4}He	30	7.5	Tandem Terminal Source
^{6}Li or ^{7}Li	1	36	860
^{11}B	5	54	860
^{12}C or ^{13}C	10	63	860
^{*14}N	1	63	DEIS or 860
^{16}O or ^{18}O	10	72	DEIS or 860
F	10	72	DEIS or 860
* Ca	0.5	99	860
Ni	0.2	99	860
I	0.001	108	860

*Negative ion is the hydride, dihydride, or trihydride.

Additional ion species available including the following: Mg, Al, Si, P, S, Cl, Fe, Cu, Ge, Se, Br and Ag. Less common isotopes are generated from enriched material.
In addition, we are now producing a separated beam of 15-MeV ^{8}B at 6 particles/second.

BOOSTER ACCELERATOR

See "Status of and Operating Experience with the University of Washington Superconducting Booster Linac," D. W. Storm *et al.*, Nucl. Instrum. Meth. A **287**, 247 (1990). The Booster is presently in a "mothballed" state.

Contents

1 Fundamental Symmetries and Weak Interactions

Weak Interactions

1.1 $\beta - \nu$ correlation in A=8 and neutrino spectrum from ^{8}B

J.M. Couture,* A. García and S. K. L. Sjue

Due to the presence of gluon exchanges between quarks the weak currents between nucleons are more complicated than the corresponding ones between leptons. The axial vector current between nucleons, for example, is:

$$\langle p|A_\mu|n\rangle = i\langle u_p| - f_a\gamma_\mu\gamma_5 - \frac{f_t}{2M}\sigma_{\mu\nu}q_\nu\gamma_5 + i\frac{f_p}{2M}q_\mu\gamma_5|u_n\rangle \quad (1)$$

The term with f_t is called Second Class Currents (SCCs) and should cancel if Time-Reversal Invariance and Charge Symmetry hold. Presently the limits on SCCs are not very good: the result of >20 years of work by a group at Osaka[1] yields an upper limit of $|f_t/f_a| < 0.15$. If enough accuracy could be reached to measure f_t/f_a at the 0.1% level, the experiments would be sensitive to the up-down quark mass difference. In the $A = 8$ system SCCs show through the angular correlations in the decay, in which the dominant terms are:

$$W(\hat{e},\hat{\nu},\hat{\alpha}) \approx 1 - \frac{v_e}{c}\hat{e}\cdot\hat{\alpha}\hat{\nu}\cdot\hat{\alpha} \mp \frac{2}{3}\frac{E_e - E_\nu}{M}b/Ac(\hat{e}\cdot\hat{\nu}) + \frac{2}{3}\frac{E_e + E_\nu}{M}(d^I/Ac \pm f_t/f_a)(\hat{e}\cdot\hat{\nu}) \quad (2)$$

where the upper (lower) sign corresponds to $\beta^{-(+)}$ decays and b, c, and d^I are the weak-magnetism, Gamow-Teller, and first-class induced pseudotensor form factors. Since last year[2]

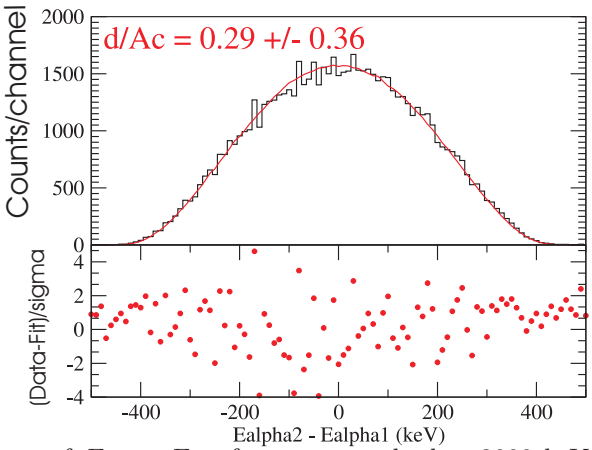

Figure 1.1-1. Histogram of $E\alpha_2 - E\alpha_1$ for events such that 3000 keV $\leq E\alpha_1 + E\alpha_2 \leq$ 3100 keV. The fit was done by minimizing the χ^2 with respect to variations in the value of $d^I/Ac \pm f_t/f_a$ in our calculations.

*Department of Physics, University of Notre Dame, Notre Dame, IN 46556.

[1] K. Minamisono *et al.*, Phys. Rev. C **65**, 015501 (2002).

[2] CENPA annual report,University of Washington (2004) p. 36.

we have generated the software we need for the analysis and can now produce plots of the difference between the energies of the two alpha particles, $E\alpha_2 - E\alpha_1$, and fit to extract the pseudo-induced tensor coupling constant $d^I/Ac \pm f_t/f_a$. With respect to extracting the shape of the ^{8}B neutrino spectrum from the alpha spectrum we have gathered the data and the analysis will soon come to conclusion.

1.2 Precise study of the final-state continuum in ^{8}Li and ^{8}B decays

E. G. Adelberger, M. Bhattacharya* and H. E. Swanson

The increasingly precise solar neutrino data, particularly from the SNO detector, place a premium on high-quality measurements of the unoscillated or intrinsic spectrum of ^{8}B neutrinos, as the oscillation parameters are sensitive to the energy-dependent distortion of the spectrum shape. This in turn requires accurate knowledge of the shape of the very broad ^{8}Be final-state continuum fed in the decays.

Two measurements of this continuum were recently reported, both with comparably high quoted precisions. Both measurements were sensitive to the summed energies of the two alphas, so the first-order effects of lepton recoil were absent. However, the two experiments involved very different systematic effects. The Ortiz *et al.* work[1] avoided positron summing by using a strong magnetic field to deflect the positrons from the alpha detectors. But this introduced energy-dependent distortions of the spectrum that had to taken into account. The experiment of Winter *et al.*[2] who implanted ^{8}B's into a Si counter, had to deal with positron summing in the implantation detector and questions about the absolute energy calibration.

Several years ago we made careful singles measurements of the delayed α spectra following ^{8}Li and ^{8}B β decays, with special emphasis on a careful calibration of the energy scale and the detector resolution.[3] Positron summing was negligible because of the small solid angle of our alpha counters. We have completed our R-matrix analysis of these data, accounting for detector energy resolution and lepton recoil effects. The resulting β-decay strength functions have very small errors, dominated by the systematic uncertainty in the energy calibration which was based on spectroscopic-grade alpha sources. The strength-function uncertainty was evaluated by doing complete analyses of the data using the best-fit energy calibration as well as with $\pm 1\sigma$ calibration relationships. Fig. 1.2-1 compares our ^{8}B strength function with recent high-precision work by Ortiz *et al.*[1] and by Winter *et al.*[2] using completely different experimental approaches that gave the summed the energies of the two αs. We are in excellent agreement with the Winter *et al.*[2] result, but the peak in our strength function is about 60 keV higher in excitation energy than that reported by Ortiz *et al.*[1]

*Mail Code XD42, Marshall Space Flight Center, Huntsville, AL 35812.

[1] C. E. Ortiz *et al.*, Phys. Rev. Lett. **85**, 2909 (2000); and C. E. Ortiz, Ph.D. Thesis, University of Notre Dame, unpublished (2000).

[2] W. T. Winter *et al.*, Phys. Rev. Lett. **91**, 252501 (2003); and W. T. Winter *et al.* nucl-ex/040619.

[3] CENPA Annual Report University of Washington, (2001) p. 48.

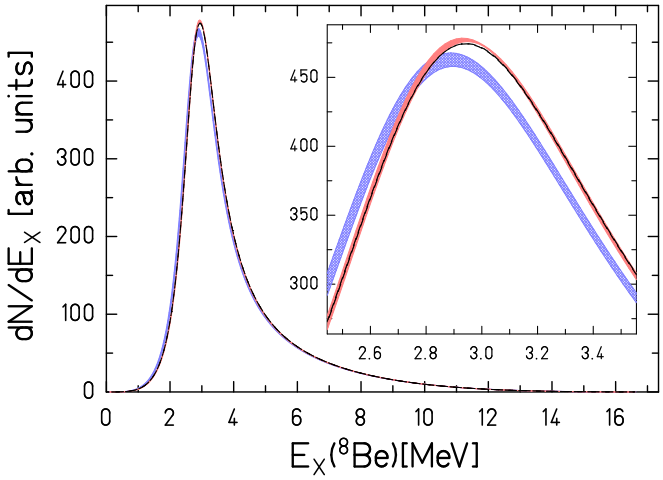

Figure 1.2-1. Comparison of ^{8}B final-state continuum shapes from our work (dark line) with recent results from Ortiz *et al.*[1] (hatched) and Winter *et al.*[2] (lighter line). The shaded bands show $\pm 1\sigma$ error bands of the R-matrix strength function. All shapes have been normalized to the same total area. Our results and those of Winter *et al.* overlap to such a degree that they are nearly indistinguishable in this plot. We generated the error band for the Ortiz et al. data from our R-matrix fits to their $\pm 1\sigma$ spectra. The Winter *et al.* error band data was generated by distorting the energy scale with a multiplicative factor of $1 \pm (0.275\%)$ added in quadrature with a constant offset of 3 keV as described in their paper.

1.3 Measuring the ^{100}Tc electron capture branching ratio

A. Algora,* A. García, S. A Hoedl, H. Penttilä,† S. K. L. Sjue, H. E. Swanson, S. Triambak and the IGISOL collaboration

We performed an experiment at the Ion Guide Isotope Separator On-Line (IGISOL) facility at the University of Jyväskylä, Jyväskylä, Finland in November 2004 to measure the electron capture branching ratio of ^{100}Tc. ^{100}Tc is an unstable isotope that beta decays to ^{100}Ru >99.9% of the time. Our experiment utilized the IGISOL facility and its ability to produce radioactive beams of short-lived isotopes in an attempt to measure the <0.1% of events in which ^{100}Tc captures an electron to become ^{100}Mo.

The analysis of this experiment presents several difficulties. The x-rays from the daughter ^{100}Mo nucleus of interest are low in energy at 17.4 keV. An accurate characterization of the overall detection efficiency as a function of energy, which varies dramatically at the relevant energies because of attenuation, is necessary to calibrate the branching ratio via the relative areas of gamma rays and x-rays in the observed spectra. The more prolific 19.2 keV ^{100}Ru x-rays are quite close in energy to the Mo x-rays, along with the 18.3 keV x-rays from the contaminative, long-lived isomer ($t_{\frac{1}{2}}$ ≈6 hr.) of ^{99}Tc, some of which the mass separation of the beamline magnet fails to eliminate (see Fig. 1.3-1). It is essential to understand the efficiency well and veto contaminants as much as possible to get a result with better than order-of-magnitude accuracy.

Data analysis is ongoing. We are currently performing PENELOPE Monte Carlo simulations in tandem with analysis of all our spectra to understand possible systematic errors. Below, Fig. 1.3-1 shows a vetoed x-ray spectrum along with its fit. Results should follow soon.

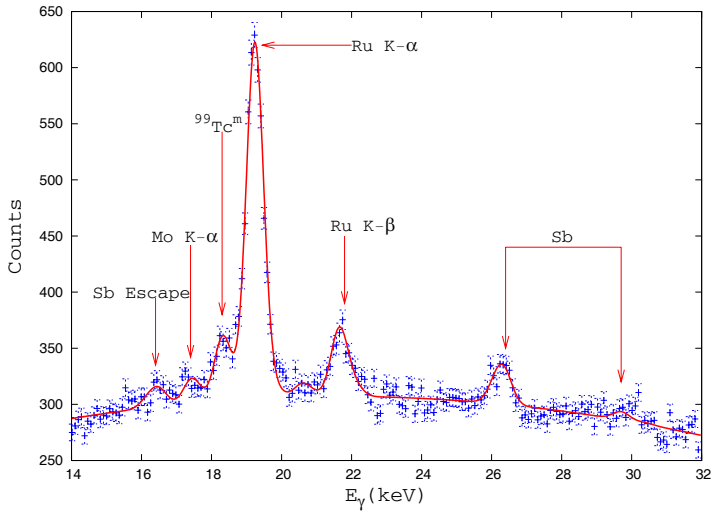

Figure 1.3-1. Vetoed x-ray spectrum with peaks labeled.

*Institute of Nuclear Research of the Hungarian Academy of Sciences Debrecen, Hungary.
†University of Jyväskylä, Jyväskylä, Finland.

1.4 Parity non-conserving neutron spin rotation experiment data acquisition progress

E. G. Adelberger, B. R. Heckel, A. Micherdzinska* and H. E. Swanson

Program development is now ongoing at both CENPA and Indiana University. We have added an additional hardware interface for controlling magnetic fields and other functions of the polarimeter and have begun tests for possible crosstalk with the ADCs. The system monitors temperatures and cryogen levels using multiple RS-232 ports accessed by USB to serial converters. The motor that pumps the liquid ^{4}He between target chambers is also controlled through one of these ports. An independent thread in the program sequences starting and stopping the pump, opening and closing valves and checking for the desired cryogen levels. For a description of the polarimeter see last years' Annual Report.[1]

Neutrons after passing through the polarimeter enter a 16-segment ^{3}He proportional counter. Individual segment currents are integrated for about one second in Burr Brown ACF 2101 gated integrators which are then read out by the ADCs. The integrator ICs used previously are no longer available and new preamps using currently available surface mount versions were constructed.

We have upgraded to National Instruments LabWindowsCVI version 7.

*Department of Physics, IUCF, Bloomington, IN 47405.

[1] CENPA Annual Report, University of Washington, (2004) p. 7.

1.5 A new source insert for the ultra-cold neutron project at Los Alamos

A. García, S. A. Hoedl, D. Melconian, A. L. Sallaska and S. K. L. Sjue

Ultra-high precision studies of neutron decay present a unique opportunity to improve the present uncertainty in V_{ud}, test the unitarity of the CKM matrix, and probe for physics beyond the standard model. We are members of the Ultra-Cold Neutron Asymmetry (UCNA) collaboration whose first goal is to measure the angular correlation between the electron momentum and the neutron spin (the β-asymmetry) five times better than the current uncertainty. Such a measurement, when combined with the presently known value of the neutron and muon lifetimes, will permit a determination of V_{ud} at the same level of precision as $0^+ \rightarrow 0^+$ decays without nuclear corrections. Additional articles in this report will discuss our efforts to construct and evaluate new ultra-cold neutron detectors. Here we discuss our efforts at improving the performance of the ultra-cold neutron source we helped construct at Los Alamos National Laboratory (LANL).

In order to use ultra-cold neutrons for the β-asymmetry a new solid deuterium source of UCN was constructed at LANL.[1] Tests in late spring 2004 indicated that the performance was an order of magnitude less than we anticipated. Four potential sources of loss were estimated with Monte Carlo studies: First, the neutron guide walls of the source may have been contaminated with neutron absorbing substances (such as water or hydro-carbons); second, the coatings applied to the guide walls may have deteriorated during instalation/operation; third, a shutter system built into the original source to prevent UCN from re-entering the solid deuterium volume may have not operated properly, and fourth, the coupling of the UCN guides between the experimental volume and the source volume may have been sub-optimal. To remedy these issues, we constructed at CENPA a source insert consisting of a new shutter, and a series of quartz neutron guides (see Fig. 1.5-1.5).

Our insert offers several advantages. First and foremost, by engineering the vacuum vessel as a separate unit from the neutron guides, we will be able to bake out the quartz to pump away potential contamination. In addition, our source insert is designed for easy removal so that the neutron guides can be easily replaced if need be. Second, our shutter operates with a rotary bearing so that the UCN guide cross section is either fully exposed or fully closed to the guide volume. In contrast the previous shutter system only exposed 40% of the guide area. Finally, the quartz guides incorporate two 45° bends to facilitate efficient coupling of the solid deuterium volume to the experimental volume. Complete tests of the CENPA source insert are expected by the end of April, 2005.

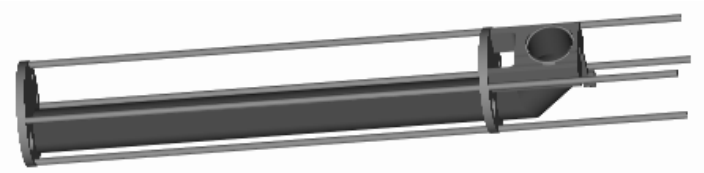

Figure 1.5-1. A schematic of the CENPA UCNA source insert.

[1] C. L. Morris *et al.*, Phys. Rev. Lett. **89**, 272501 (2002)

1.6 UCN monitors and absorbers: fabrication and testing

A. García, S. A. Hoedl, D. Melconian, A. L. Sallaska and S. K. L. Sjue

Over the past year, we have fabricated several types of ultracold neutron (UCN) monitors to probe the flux of neutrons in the UCNA experiment being conducted at Los Alamos National Labs. We have also produced absorbers to remove any UCN that do not decay in the specified decay volume. Because UCN are difficult to detect without allowing them to drop down a vertical pipe to a ^{3}He gas counter, it is necessary to convert the neutrons into charged particles by passage through thin foils. The charged particles are then detected by silicon surface barrier detectors located directly behind the foils. The main problem with this technique is implementing materials with low enough Fermi potentials to allow the UCN to penetrate. Two different materials were chosen: natural LiF and ion-implanted ^{10}B. Both have near zero potentials and also have high capture cross sections, on the order of megabarns, for UCN. For the LiF foils, the reaction is $n + ^6\mathrm{Li} \rightarrow ^4\mathrm{He} + ^3\mathrm{H}$ with both products having energies on the order of a few MeV and a cross section of 4.7×10^5 barns. The presence of the fluorine is for stability. The boron foils undergo the reaction $n + ^{10}\mathrm{B} \rightarrow ^7\mathrm{Li} + ^4\mathrm{He}$ with a cross section of 1.8×10^6 barns and MeV energies. Another benefit of these detectors is that the UCN do not need to penetrate an aluminum window, as they must do in the ^{3}He counters, so the energy range they are sensitive to has a possibility of being larger than with ^{3}He.

We have fabricated eight LiF foils and five boron foils. The LiF foils can be easily evaporated at CENPA with the resistive evaporator onto thin nickel foils ($< 1\mu$m thick). Nickel has a very high Fermi potential so if the UCN do not interact within the material, they will be reflected, which increases their interaction probability by a factor of two. The process of evaporating 300 μg/cm^2 of natural LiF takes about a day under pressures between high 10^{-7} Torr and low 10^{-6} Torr. The main concern is maintaining a low deposition rate, which should not exceed 10 Ångström/s. If the rate is higher than this, there is a high probability of breaking the foils.

The low deposition rate also applies to the boron foils. The current of negative boron ions onto the nickel target must be kept very low to avoid breaking the foils. Here, a 2000 Ångström thick layer of vanadium is applied to the nickel as well as a 200 Ångström layer of chromium for adhesion. The vanadium has a negative potential and needs to be evaporated by an e-beam. After one day of bombardment, roughly 1×10^{18} atoms can be produced.

Both types of foils were tested at the ILL in Grenoble, France at the end of March 2005 and will be used in monitoring the flux of UCN at LANL's upcoming spring 2005 run. Two of our foils have been tested previously at the ILL by colleagues from North Carolina State University; however, their results were inconclusive. At the ILL, we hope to produce time of flight spectra for several different foils: boron and LiF foils made in spring 2004, LiF foils made in spring 2005, and blank nickel foils. We will be comparing these data to a ^{3}He proportional counter, which has an efficiency of approximately 100 %. We also hope to be able to characterize the energy dependence of our foils' efficiency by using a gravitational spectrometer. This spectrometer will provide a gravitational barrier for our neutrons at a variety of heights, thereby setting different maximum energy limits on our spectrum.

We have also fabricated two different types of neutron absorbers. If the neutrons do not decay, we want to remove them to keep them from adversely affecting our other measurements. These materials also have to have a low Fermi potential and have a high neutron capture cross section. Naturally, we picked LiF and also a material called TPX, which is a 3-methylpentene-1 based polyolefin. TPX has a nearly zero potential because of the rich concentration of hydrogen, which has a slightly negative potential. The TPX has been formed into two different configurations, and the LiF has been evaporated on to sheets of stainless steel by wrapping the metal around rotating cylinders. During our experiment at the ILL, we plan to test a sample of TPX for its absorbing qualities. Both materials will also be employed in our spring 2005 run at LANL.

1.7 Calculations of polarized-neutron decay asymmetries to recoil order

A. García and S. K. L. Sjue

To ascertain the ultimate accuracy with which one can extract physics from our upcoming measurements of correlation parameters from polarized neutron decay, we have calculated the β-asymmetry A_β, the electron-neutrino correlation $a_{e\nu}$, and the proton asymmetry A_p including recoil-order effects. Treating the proton and neutron as elementary particles in an effective field theory, it is relatively simple to calculate all the recoil-order effects on the decay of the polarized neutron. We calculated the matrix element with recoil-order terms in the hadron current:

$$\begin{aligned} M &= G_F h^\mu \times l_\mu, \\ h^\mu &= \overline{p}(f_1\gamma^\mu - i f_2 \sigma^{\mu\nu}\tfrac{k_\nu}{m_n} + f_3\tfrac{k^\mu}{m_n} - g_1\gamma^\mu\gamma_5 + i g_2\sigma^{\mu\nu}\tfrac{k_\nu}{m_n}\gamma_5 - g_3\tfrac{k^\mu}{m_n}\gamma_5)n, \\ l_\mu &= \overline{e}\gamma_\mu(1-\gamma_5)\nu. \end{aligned}$$

Point-like particles only require the f_1 and g_1 terms, but for composite nucleons the current contains, in general, the recoil-order terms. Effects due to f_2,f_3,g_2, and g_3 are all suppressed by the small factor $\frac{k}{m_n}$ =0.8MeV/931MeV $\approx$ .001. To get an accurate estimate of the effects of the recoil-order terms in the matrix element, kinematic terms of the same order must be included.

We obtain analytical expressions for the β asymmetry $A_\beta(E_e)$, the $e-\nu$ correlation $a_{e\nu}(E_e)$, and the proton asymmetry $A_p(E_e)$. Our calculations agree with previous results for $A_\beta(E_e)$ and $a_{e\nu}(E_e)$.[1,2] None of the previous calculations have expressions for A_p. Below, Fig. 1.7-1 shows the difference in $A_p(E_e)$ when assuming the CVC value for f_2 versus assuming f_2 =0. This shows the precision necessary to extract f_2 via the proton asymmetry. These expressions will be essential to analyze our polarized neutron decay data, and to determine which observables to use for the best tests of various Standard Model parameters.

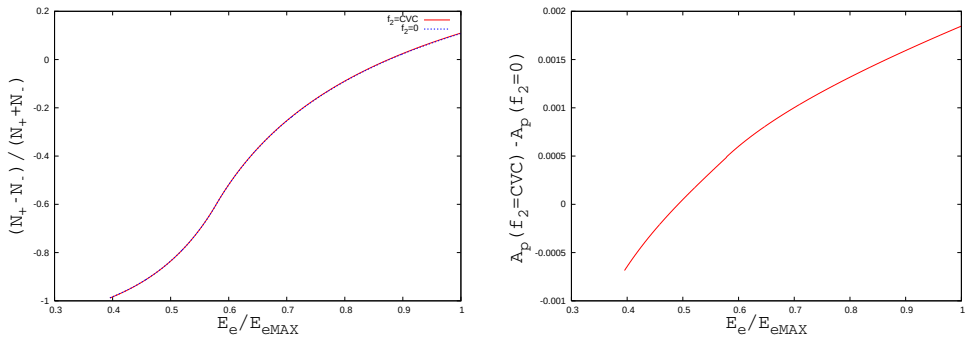

Figure 1.7-1. On the left is A_p, the proton asymmetry, and on the right is the difference between A_p for f_2 =CVC and f_2 =0.

[1] S. Gardner and C. Zhang, Phys. Rev. Lett. **86**, 5666 (2001).
[2] B. R. Holstein, Rev. Mod. Phys. **46**, 789 (1974).

1.8 emiT: Time reversal violation in neutron beta decay

A. García, H. P Mumm,* R. G. H. Robertson, M. F. Wehrenberg and J. F. Wilkerson

The emiT experiment, a search for time-reversal violation in neutron beta-decay completed a successful measurement on the NG-6 beamline at the NIST Center for Neutron Research (NCNR) in Gaithersburg, MD at the end of 2003. Currently we are working to complete the analysis of more than 250 million coincidence events which were collected during this run. These data should allow us obtain a statistical sensitivity to the T-violating coefficient "D" of 2×10^{-4}, which would exceed our original design goal by about a factor of 1.5. Not only were more data collected than in our first run, but the current data are of much higher quality. From our preliminary analysis the signal to noise was improved from about 2.5 to 1 to on the order of 100 to 1.

During the past year a comprehensive study of potential systematic uncertainties was completed by Mumm as part of his Ph.D. dissertation.[1] Two new systematic issues were identified that were not considered during our first run. The first, the sensitivity of the analysis to a spin dependent proton recoil spectrum, will require fitting the proton energy spectrum. We have now demonstrated that such an approach is feasible. Second, we recognized that electron backscattering plays an important role, and explains discrepancies observed between Monte Carlo and data seen in the analysis of our first run. After incorporated this backscattering into our Monte Carlo we were able to demonstrate that the improved simulation reproduces the observed coincidence rates. Based on this thorough characterization of all the systematic uncertainties we find that the largest of these will be less than 1×10^{-4}, which is below our expected statistical sensitivity of 2×10^{-4}.

Our present efforts are concentrated on data reduction and analysis. Data filtering routines have been developed which accept only data collected during periods where all environmental parameters, for example magnetic fields and high voltage, fell within acceptable ranges. In addition a detailed study of the beta detector timing and energy calibrations is nearing completion. Once these data reduction and cleaning tasks are complete we will proceed to carry out a full analysis of the D-coefficient, likely using both a super-ratio and PIN-pair based analyses.

*NIST, 100 Bureau Drive, MS8461, Gaithersburg, MD 20899.

[1] H. P Mumm, Ph.D. dissertation, University of Washington, 2004.

1.9 Search for a permanent electric dipole moment of ^{199}Hg

E. N. Fortson,* W. C. Griffith,* M. V. Romalis† and M. D. Swallows

An experimental effort is underway to improve the limit on, or possibly detect, a permanent electric dipole moment (EDM) of ^{199}Hg. The discovery of a non-zero EDM would reveal a new source of CP-violation, and would be experimental evidence for the existence of new physics such as supersymmetry. Our previous measurement[1] obtained a limit of $|d(^{199}\mathrm{Hg})| < 2.1 \times 10^{-28}\, e\,\mathrm{cm}$ by comparing the ^{199}Hg spin precession frequencies in a stack of two Hg vapor cells in a common magnetic field and oppositely directed electric fields. Our upgraded version of this experiment uses a stack of four vapor cells. The two additional cells have no electric field applied to them, and are used essentially as magnetometers to improve our statistical sensitivity and our understanding of systematic effects.

As of one year ago, we were attempting to understand a significant systematic effect that appeared frequently in the data taken with our upgraded apparatus. In our experiment, the signature of an EDM would be a shift in the ^{199}Hg spin precession frequency correlated with the electric field direction. Since ^{199}Hg has a magnetic moment, the most dangerous systematic effects are those that cause changes in the magnetic field at the vapor cells when we switch the polarity of the applied high voltage. The typical size of our false signals would correspond to a local magnetic field change of 20 pG, or an EDM of $2 \times 10^{-27}\, e\,\mathrm{cm}$, an order of magnitude larger than our previous limit. We do not believe these signals are evidence of an actual EDM, because the frequency shifts do not appear as symmetrically opposite shifts in the 2 cells with opposite electric fields, and they often occur in the magnetometer cells. Our investigations of this systematic effect are ongoing.

Over the past nine months, most of our effort has been devoted to the measurement of a linear Stark effect on the 254-nm resonance line in ^{199}Hg. In the presence of a static electric field, the 254-nm electric dipole transition can acquire magnetic dipole and electric quadrupole components which interfere with the electric dipole transition amplitude. This interference can lead to energy shifts that are linear in the applied electric field, and could mimic an EDM signal under certain conditions. The fractional change in the absorbtivity of the 254-nm line due to this interference has previously been calculated[2] to be $\delta\alpha/\alpha = -6.6 \times 10^{-8}(\mathrm{kV/cm})^{-1}$. Our measurement technique detects the Stark interference-induced phase shift of an optical signal due to the absorption of circularly polarized light by the spin-polarized Hg vapor. The experiment is ongoing, but our preliminary result ($\delta\alpha/\alpha = -6.2 \pm 0.6 \times 10^{-8}$ $(\mathrm{kV/cm})^{-1}$, quoted error statistical only) is in good agreement with the calculation. However, we have also encountered an unexplained systematic effect that clouds our interpretation of the data. Our immediate goal is to understand this systematic effect and complete our measurement of Stark interference in ^{199}Hg.

*Physics Department, University of Washington, Seattle, WA 98195.
†Department of Physics, Princeton University, Princeton, NJ 08544.

[1] M. V. Romalis, W. C. Griffith, J. P. Jacobs, and E. N. Fortson, Phys. Rev. Lett. **86**, 2505 (2001).
[2] S. K. Lamoreaux and E. N. Fortson, Phys. Rev. A. **46**, 11 (1992).

Torsion Balance Experiments

1.10 Sub-mm test of Newton's inverse-square law

E. G. Adelberger, T. S. Cook, J. H. Gundlach, B. R. Heckel, C. D. Hoyle, D. J. Kapner and H. E. Swanson

We completed a data-set with our 21-fold symmetric torsion pendulum to probe Newton's inverse-square law (ISL) at short distances. We achieved our smallest-yet minimum vertical separation between our attractor and detector rings of 65μm and we observe a discrepancy between our data and the ISL at distances smaller than 100μm. This discrepancy is an effect which changes with height and acts on our detector with a force whose sign is opposite that of Newtonian gravity. We can not reasonably account for this discrepancy and are currently repeating this measurement. Our increased sensitivity is shown in Fig. 1.10-1.

Between measurements, we have : (1) replaced our $\sim$ 20μm diameter torsion fiber with $\sim$ 18μm fiber to reduce our limiting thermal noise. (2) had our lower attractor ring lapped thinner by $\sim$ 125μm to change the expected shape of our Newtonian signal. (3) reduced a bend in our pendulum ring of $\pm$13μm to $\pm$4μm to achieve smaller vertical separations. (4) begun using a coordinate measuring machine for a more precise and comprehensive measurement of the attractor rings' thicknesses and the gap between them. (5) mounted our external calibration turntable solidly to the same cyclotron magnet yoke as our short-range apparatus. The turntable position is now motorized and electronically indicated. (6) implemented a new data-acquisition computer and an upgraded data-acquisition program.

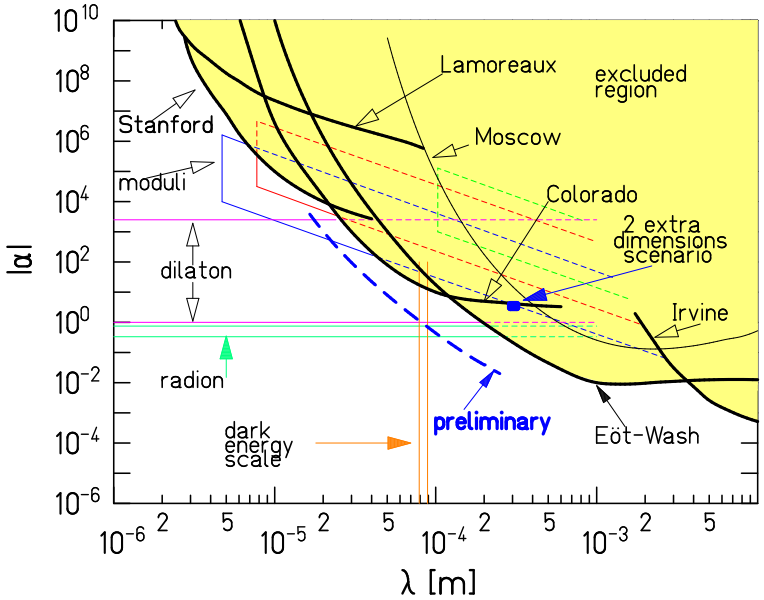

Figure 1.10-1. 95% *exclusion* limits on $|\alpha|$ and λ, the strength and range of a Yukawa potential. The line labeled "preliminary" indicates the sensitivity of our recent data set as compared to our previous limits labeled "Eöt-Wash".

1.11 Next generation short-range gravity pendulum

E. G. Adelberger, T. S. Cook and C. D. Hoyle

We are currently designing the next generation pendulum to test Newton's inverse square law at short distances. There will be two key changes to the geometry of the new pendulum in comparison to previous designs, chosen to maximize a Yukawa deviation while simultaneously minimizing the Newtonian background.

The torque from a short-range Yukawa interaction is proportional to the change in overlap area of the test masses per change in angle between pendulum and attractor. In order to maximize this, the azimuthal symmetry will be greatly increased. Past pendulums have employed anywhere from 10-22 fold symmetry in the azimuthal mass distribution. The new pendulum will be built with 120-240 fold symmetry, which decreases the angle between minimum and maximum overlap, increasing the Yukawa signal by a factor of about ten over previous designs. The higher symmetry also washes out the Newtonian torque and should remove the need for the Newton-canceling attractor used with previous designs.

The second key change in geometry is the shape of the test masses. All previous work has used cylindrical test masses (for engineering reasons), which is clearly not the ideal geometry to maximize the Yukawa torque. The new pendulum will maximize the overlap area by using pie shaped "wedges" as test masses. The wedges will likely be cut using hi-precision electrical discharge machining.

Additional improvements will come from using higher density test masses, a lighter overall design, a thinner torsion fiber, and other apparatus upgrades. Work to date has focused on researching numerous fabrication techniques and assessing design feasibility.

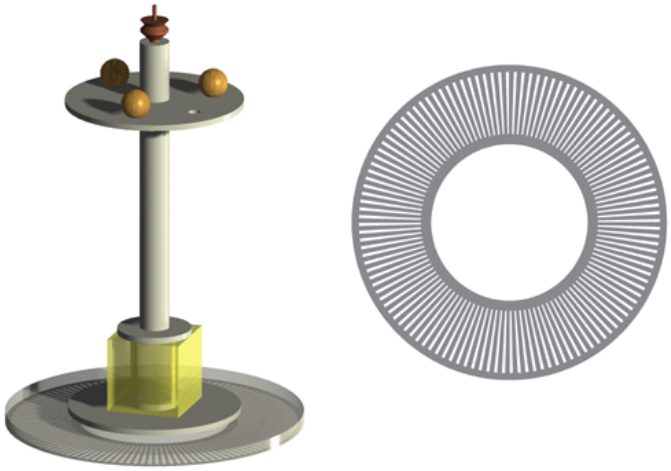

Figure 1.11-1. Possible pendulum design (left). 120-fold symmetric mass distribution (right).

1.12 A new test of the equivalence principle

E. G. Adelberger, K. Choi, J. H. Gundlach, B. R. Heckel, S. Schlamminger, C. D. Spitzer and H. E. Swanson

We are using a rotating torsion balance to test the equivalence principle for Yukawa range from 1 m to ∞. A sensitive torsion balance is mounted on an air bearing turntable rotating with constant angular velocity. On the torsion pendulum, four beryllium and four titanium test bodies are installed in a composition dipole configuration. A violation of the equivalence principle would yield a differential acceleration of the two materials towards a source mass. We can analyze this differential acceleration for a variety of sources, such as local topological features (hillside), the entire Earth, the Sun or the center of our galaxy. Since 25% of the differential acceleration towards the center of the galaxy is caused by galactic dark matter, it allows us to test the equivalence principle for ordinary matter falling towards galactic dark matter.

During the past year we have been taking data with the composition dipole pendulum. We have discovered a slow drift of the signal which we attribute to a subtle time dependent change in the turntable angle readout. In order to minimize this effect, we changed the orientation of the direction of the dipole once a day by rotating the pendulum with respect to the turntable without opening the apparatus. Fig. 1.12-1 shows the angular deflection amplitude of the pendulum due to a laboratory fixed torque, i.e our signal, in west-east and north-south direction. The statistical uncertainty of the signal measured over 56 days is 0.38 nrad, which corresponds to a differential acceleration sensitivity of 2.4 $\times 10^{-15}$ m/s^2.

We found a signal in the NS direction of -3.1 ± 0.4 nrad. The investigation of this resolved effect is in progress. In particular we have remeasured the gravity gradient fields with our gradiometer pendulum and found a residual Q_{31} field large enough to produce a signal in the order of 1 nrad. Subsequently, we reduced this gradient field by a factor of 40.

We have now reversed the orientation of the composition dipole relative to the pendulum frame by exchanging the test bodies. We have minimized and precisely measured the q_{21} and q_{31} moments of the eight test body pendulum. The expected residual gravitational coupling of the pendulum to the environment would result in a signal of at 0.06 nrad (Q_{21}) and 0.02 nrad (Q_{31}).

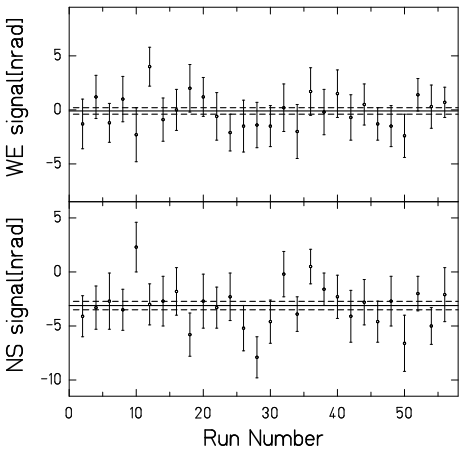

Figure 1.12-1. The results for 56 days of measurements. Each data point represents two runs with the opposite direction of the composition dipole with respect to the turntable. The dashed lines show the 1σ limits obtained from a statistical average of data sets.

1.13 Small force studies for LISA

J. H. Gundlach, C. A. Hagedorn, B. R. Heckel, M. J. Nickerson, S. Schlamminger and C. D. Spitzer

We are performing low noise force tests for the Laser Interferometer Space Antenna (LISA).[1] LISA consists of three spacecraft that form independent interferometers in a large triangle with sides of length $5,000,000$ km. The displacement of 2 kg test masses at the interferometer ends will be resolved with a 20 pm sensitivity. Spurious forces that may act between the test mass and the nearest housing surfaces have to be investigated at the frequency range of 10^{-4} to 10^{-1} Hz. In the past year we have improved our existing low noise torsion balance to measure these forces.

In order to get a higher torque sensitivity we changed the size of our pendulum to be a 101.6 mm by 38.1 mm gold coated glass plate with an aluminum q21 compensator bar at the top. Compared to the old pendulum this size gives us a factor of ~ 6 increase in force sensitivity. In addition we have changed our opposing plate to a gold coated glass plate with the same dimensions as the pendulum. The opposing plate simulates the housing of the test mass and can be moved to various distances from the pendulum in order to measure distance dependent forces between the surfaces.

Furthermore, we have installed two gold coated aluminum control electrodes behind the pendulum. These electrodes allow us to apply torques in both directions and can be used for feedback control of the pendulum.

The measures taken last year have increased the sensitivity of the torsion balance appreciably. As shown in Fig. 1.13-1, the measured force noise is only one order of magnitude above the LISA requirement at 0.1 mHz.

In order to reduce the force noise of the existing setup, a fiber with a higher mechanical quality factor, i.e., smaller loss factor, is required. We have focused our efforts on the production of quartz fibers. We have established a procedure to reproducibly draw fibers from 1 mm fused quartz rods. Our fibers are typically 0.6 m long and have a torsional constant of 0.23 nNm. We have started developing gold coating procedures for such fibers. For technical reasons the fiber could be gold-coated on only one side. Charge build up on the non-coated side may be the source of additional noise. We are now working on a procedure to completely coat the fiber.

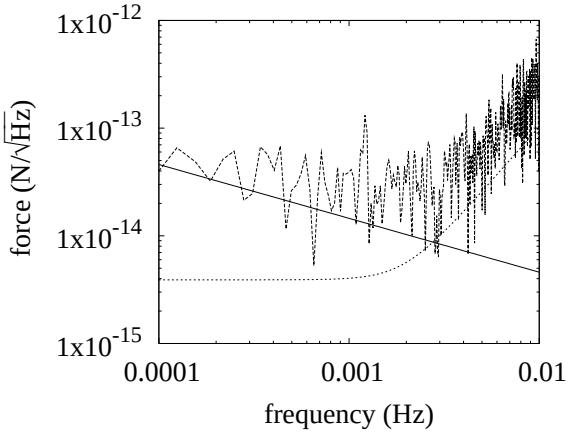

Figure 1.13-1. Measured force noise (dashed line) and thermal limit (solid line) of the torsion pendulum at 6 mm separation between the attractor plate and the pendulum. The dotted line indicates the force noise equivalent to the requirement for LISA.

[1] http://lisa.jpl.nasa.gov/

1.14 Progress on the torsion pendulum based axion search

E. G. Adelberger, B. R. Heckel, S. A. Hoedl and H. E. Swanson

Calculations indicate that a torsion pendulum search for the axion will offer an improvement of 10^{18} over the most recent measurement[1] for an axion mass of $\sim$ 200 μeV. The axion is the result of the hypothesized Peccei-Quinn symmetry and is a favored cold dark matter candidate.[2] The mass is constrained by the known flat geometry of the universe to be heavier than 1 μeV ($\lambda_a < 20$ cm), and is constrained by the neutrino flux from SN1987A to be lighter than 1000 μeV ($\lambda_a > 0.02$ cm). Note that microwave cavity searches probe for light axions (1.2 μeV $< m_a <$ 12.4 μeV). A torsion-pendulum based search is possible because the axion mediates a macroscopic pseudo-scalar potential between polarized and unpolarized fermions. By observing the motion of a germanium planar torsion pendulum (source of unpolarized fermions) position near the pole faces of an energized ferromagnet, we can observe such a force.

In the past year, we have designed and built the majority of the equipment necessary to begin our torsion pendulum based axion search. We have constructed a three dimensional translation stage capable of moving the torsion pendulum and a 10 kg load 10 cm in the vertical direction with a horizontal runout of less than $\pm 5 \times 10^{-4}$ cm. We have also fabricated the necessary vacuum chamber, three μ-metal magnetic shields, and mounted this equipment at an appropriate location in our laboratory. In addition, we are in the process of evaluating prospective magnet and pendulum geometries. We have identified a method for cutting a silicon or germanium wafer to shape without introducing ferromagnetic impurities. In the following year we anticipate a first measurement will be complete.

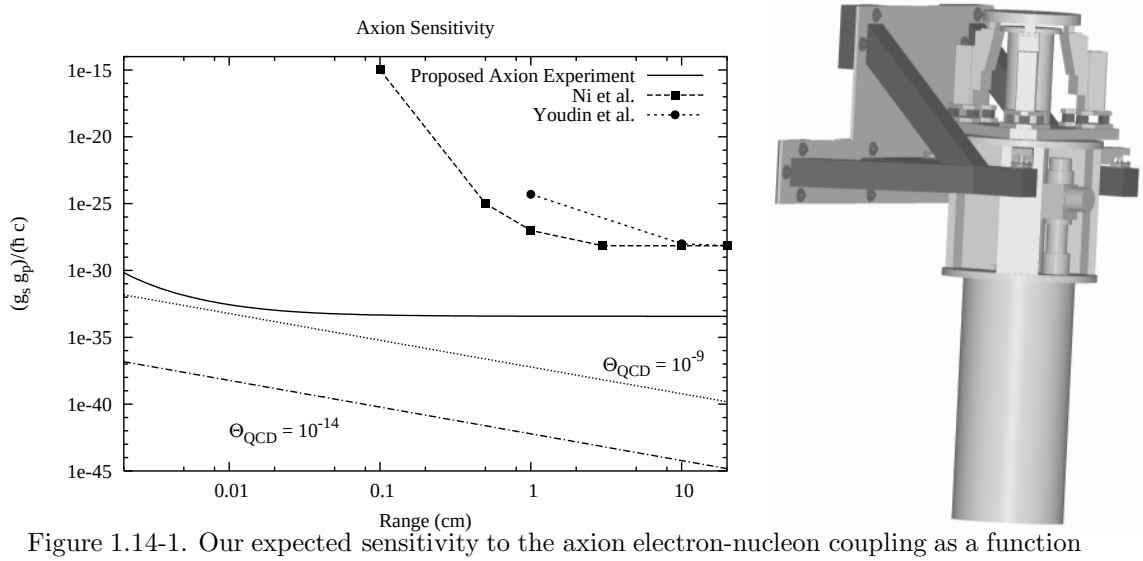

Figure 1.14-1. Our expected sensitivity to the axion electron-nucleon coupling as a function of the axion Compton wavelength compared with recent experimental searches and the expected coupling for different values of Θ_{QCD}; a picture of our axion-pendulum apparatus.

[1] W. T. Ni *et. al.* Phys. Rev. Lett. **82**, 2439 (1999).

[2] L. J. Rosenberg and K. A. van Bibber, Phys. Rep. **325**, 1 (2000).

1.15 Eötwash data-acquisition development

E. G. Adelberger, T. S. Cook, D. J. Kapner, M. J. Nickerson, S. Schlamminger and H. E. Swanson

EÖTWASH: Both the original and Eötwash-II data acquisition systems continue to run reliably and no upgrades are contemplated for these systems.

SRTWASH: We have upgraded the short range gravity data acquisition system to include a 3 GHz P-4 PC running Windows XP and a National Instruments PCI-6031 64 channel DAQ board. The software which incorporates much of our existing code was developed using Microsoft's Visual C++ and National Instrument's LabWindowsCVI version 7. The additional ADC channels permit us to continuously monitor individual temperature sensors without the need of an external multiplexer. On board counters keep track of the source and calibration turntable angles. There is less need for the custom electronics used in previous systems and it can be easily adapted to future experiments.

A Stanford DS 345 controls the sample rate of the DAQ board through an external input. The board handles all timings for reading the ADC channels and sends the values to the program. This significantly offloads the CPU when compared with the previous system and allows faster sample rates. The calibration turntable can now be positioned under computer control to avoid disturbing the thermal environment of the pendulum while taking data. Additional RS-232 ports were added to control and monitor the table's position using USB to Serial converters.

LISA DAQ: In the past year we have added a 16 channel 16 bit analog output card to the computer. Two channels were used to apply voltages on the control electrodes (see LISA article) behind the LISA pendulum. Utilizing these electrodes, we have programmed a PID-feedback algorithm to hold the pendulum at any given position or to follow a programmed periodic motion.

We enhanced the online data analysis capability of the LISA data taking software by a power spectrum estimator and a sine wave fitter. The former allows the user to see the noise power versus frequency and track the power content of a given frequency band over time. The later estimates the equilibrium position, amplitude and the frequency of the pendulum's motion. Both features provide their results as virtual sensors, which can be saved and visualized in the framework of the DAQ-software, including the data analysis software.

1.16 Status of the APOLLO lunar laser ranging project

E. G. Adelberger, C. D. Hoyle, H. E. Swanson, T. D. Van Wechel and the APOLLO Collaboration

A host of phenomena including extensions of the standard model and novel theories of gravity may be investigated by characterizing the shape of the lunar orbit. In particular, current measurements place the most stringent limits on the strength of a Yukawa-type deviation from Newton's gravitational inverse-square law, albeit only for distance scales comparable to the Earth-Moon separation ($\sim 400,000$ km). Such tests also probe effects such as Einstein's strong equivalence principle, extra-dimension and braneworld scenarios, gravitomagnetic effects, and the possible time variation of the gravitational constant, to name a few.

APOLLO (Apache POint Lunar Laser ranging Operation)[1] aims to measure the shape of the lunar orbit with unprecedented precision. A portion of a 532 nm laser beam, expanded to fill the primary mirror of the 3.5 m telescope at the Apache Point Observatory in New Mexico, will be returned by retroreflectors deposited on the lunar surface by various teams of astronauts. This large aperture will receive about 5 return photons per laser shot, or about 100 photons/s at 20 Hz, an improvement of roughly a factor of 100 in signal strength relative to previous experiments.[2] This improved signal coupled with precision timing of the round-trip photon travel time will allow characterization of the lunar orbit at the millimeter level, or about an order of magnitude better than it is known now.

We are currently gearing up to make the first range measurements this summer. Much progress has been made regarding the mechanical interface of the apparatus to the telescope and design and construction of the various necessary components in the optical path. In order to precisely measure the round-trip time, we need an accurate time-zero mark. We will use photons reflected from a corner cube mounted directly on the telescope to provide this basis for our differential measurement of the photon time-of-flight. Results showing a possible bias in this time-zero measurement due to localization of the photons within the Avalanche Photodiode (APD) detector array elements necessitated the development of a time-modulated diffusing optical element, to ensure that the spatial distribution of the time-zero photons closely resembles that of the lunar returns. This component has been successfully designed and tested.

In addition, the configuration of the APOLLO Command Module (ACM), a CAMAC hardware/software interface module, has been finalized and it now successfully performs its required tasks.

In preparation for operation, several tasks must be accomplished in the coming months including completion of the mechanical/thermal interfaces, installation of the receiver optical elements, further characterization of the APD array (particularly crosstalk and EMI issues), and finalization of acquisition and analysis software, including the development of a graphical user interface compatible with the existing Telescope User Interface (TUI) software.

[1] T. W. Murphy, J. D. Strasburg, E. G. Adelberger, C. W. Stubbs and K. Nordtvedt, Nucl. Phys. B **134**, 155 (2004).

[2] J. G. Williams, S. G. Turyshev, and D. H. Boggs, Phys. Rev. Lett. **93**, 261101 (2004).

2 Neutrino Research

SNO

2.1 Recent solar neutrino results from SNO

J. F. Amsbaugh, T. H. Burritt, G. A. Cox, P. J. Doe, C. A. Duba, J. A. Formaggio, G. C. Harper, M. A. Howe, S. McGee, K. K. S. Miknaitis, A. W. Myers, N. S. Oblath, J. L. Orrell,* K. Rielage, R. G. H. Robertson, M. W. E. Smith,† L. C. Stonehill, B. L. Wall, T. D. Van Wechel, J. F. Wilkerson and the SNO Collaboration

The Sudbury Neutrino Observatory (SNO) is a heavy-water Cherenkov detector located 6800 feet underground near Sudbury, Ontario. Using ultra-pure heavy water as a solar neutrino target, SNO is sensitive to three reactions of ^{8}B solar neutrinos on deuterium,

$$\begin{array}{lrcl} \text{ChargedCurrent(CC)Reaction}: & \nu_e + \mathrm{d} & \longrightarrow & \mathrm{p} + \mathrm{p} + e^- \\ \text{ElasticScattering(ES)Reaction}: & \nu_x + e^- & \longrightarrow & \nu_x + e^- \\ \text{NeutralCurrent(NC)Reaction}: & \nu_x + \mathrm{d} & \longrightarrow & \mathrm{p} + \mathrm{n} \end{array}$$

where ν_e indicates electron-flavor neutrinos, and ν_x indicates neutrinos of any flavor. The NC reaction in SNO allows a measurement of the total flux of ^{8}B solar neutrinos, while a comparison of the CC and NC reaction rates probes solar neutrino flavor change.

Cherenkov radiation from the electrons produced in the CC and ES reactions is detected using an array of approximately 9500 photomultiplier tubes. The neutrons liberated in the NC reaction must be detected through a secondary capture reaction. The SNO experiment has three phases, relying on three distinct neutron capture signatures. In the first phase, neutrons were detected using the 6.25 MeV gamma resulting from neutron capture on deuterium. Measurements during the first phase of SNO confirmed solar model predictions of the ^{8}B flux, demonstrated solar neutrino flavor change, and improved constraints on the underlying neutrino oscillation parameters.[1]

In the second phase of the experiment, ultra-pure salt (NaCl) was added to the D_2O. The higher cross section for neutron capture on ^{35}Cl and the higher energy (8.6 MeV) released in the reaction improve SNO's efficiency for detecting NC neutrons by nearly a factor of three relative to the first phase. In addition, the multiple gammas released in the ^{35}Cl capture reaction result in a more isotropic distribution of Cherenkov light relative to the distribution of light in single-electron events. Using the isotropy of light produced in a neutrino event, the CC, NC, and ES signals can be statistically separated without requiring constraints on the solar neutrino energy spectrum. This allows model-independent results from the salt phase. First results for 254 days of salt data were published in 2004.[2,3]

*Present address: Pacific Northwest National Laboratory, Richland, WA 99352.

†NASA JPL, MS 302-306, 4800 Oak Grove Dr. Pasadena CA 91109.

[1] Phys. Rev. Lett. **87**, 071301 (2001); Phys. Rev. Lett. **89**, 011301 (2002); Phys. Rev. Lett. **89**, 011302 (2002); all by the SNO Collaboration.

[2] S. N. Ahmed *et al.*, Phys. Rev. Lett. **92**, 181301 (2004).

[3] CENPA Annual Report, University of Washington (2004) p. 19.

Solar neutrino analysis has recently been completed on the full 391 days of salt data.[4] A model-independent determination of the reaction rates in SNO yields equivalent ^{8}B solar neutrino fluxes (in units of $10^6 \mathrm{cm}^{-2}\mathrm{s}^{-1}$):

$$\begin{aligned} \phi_{\mathrm{CC}} &= 1.68^{+0.06}_{-0.06}(\mathrm{stat.})^{+0.08}_{-0.09}(\mathrm{syst}) \\ \phi_{\mathrm{ES}} &= 2.35^{+0.22}_{-0.22}(\mathrm{stat.})^{+0.15}_{-0.15}(\mathrm{syst}) \\ \phi_{\mathrm{NC}} &= 4.94^{+0.21}_{-0.21}(\mathrm{stat.})^{+0.38}_{-0.34}(\mathrm{syst}). \end{aligned} \quad (1)$$

These results are depicted in Fig. 2.1-1. The NC measurement in the salt phase improves SNO's determination of the total ^{8}B flux from the sun, and agrees with standard solar model predictions, as shown in the figure. The best-fit point indicates the appearance of mu-tau neutrinos in the solar neutrino flux. Together with the results of other experiments, SNO's determination of solar neutrino flavor change provides strong evidence for neutrino oscillations and physics beyond the standard model. The electron energy spectrum from the CC reaction has also been measured, and is found to be consistent with solar model predictions as well as with the favored neutrino oscillation model.

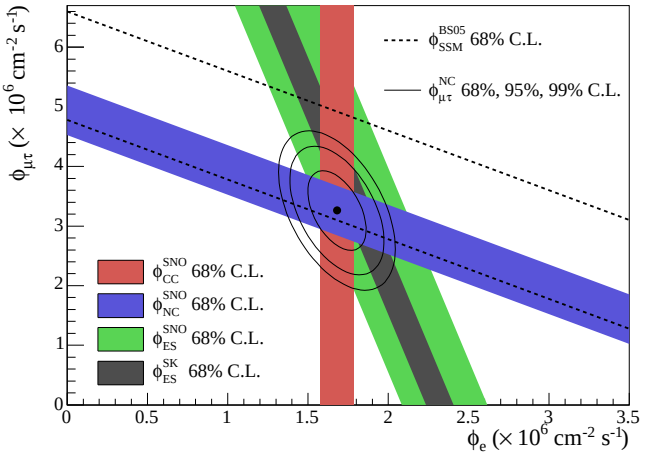

Figure 2.1-1. Flux of μ and τ neutrinos versus flux of electron neutrinos, for SNO's CC, NC, and ES reactions, Super-Kamiokande's ES result, and the solar model prediction.

Neutrino oscillations depend on the mass splitting of the underlying neutrino states, characterized by $\Delta m^2 = m_2^2 - m_1^2$, and the mixing angle θ that parameterizes the strength of the neutrino mixing. A global solar neutrino oscillation analysis has been performed, including the results of the first and second phases of SNO, along with the results of other solar neutrino experiments and the KamLAND reactor anti-neutrino experiment. The best-fit values for the neutrino oscillation parameters are

$$\Delta m^2 = (8.0^{+0.6}_{-0.4}) \times 10^{-5}\mathrm{eV}^2; \;\; \theta = 33.9^{+2.4}_{-2.2}\,\mathrm{degrees}. \quad (2)$$

The third phase of SNO is underway, in which the neutrons from the NC reaction are detected using an array of discrete ^{3}He proportional counters deployed in the detector volume. The third phase of the experiment will be described in Sections 2.4 through 2.12.

[4] LANL arXiv:nucl-ex/0502021

2.2 Day-night results from the salt phase of SNO

K. K. S. Miknaitis, and the SNO Collaboration

The favored model for solar neutrino oscillations invokes matter-enhanced oscillation in the solar interior, through the so-called MSW effect. Matter effects could also alter the flavor composition of neutrinos that pass through the earth before arriving at SNO. A day-night asymmetry in the CC reaction in SNO would therefore constitute direct evidence for the MSW effect. To search for day-night differences in solar neutrino flavor, we construct asymmetry parameters in terms of the measured day and night fluxes, $A_\alpha = 2(\Phi_{\alpha,N} - \Phi_{\alpha,D})/(\Phi_{\alpha,N} + \Phi_{\alpha,D})$, where α = CC, NC, ES.

The salt phase analysis allows a model independent determination of the day-night asymmetries,[1]

$$\begin{aligned} A_{CC} &= -0.050 \pm 0.074(\text{stat.}) \pm 0.053(\text{syst.}) \\ A_{NC} &= 0.042 \pm 0.086(\text{stat.}) \pm 0.072(\text{syst.}) \\ A_{ES} &= 0.146 \pm 0.198(\text{stat.}) \pm 0.033(\text{syst.}). \end{aligned} \quad (1)$$

Since an asymmetry in the NC rate is not expected for standard neutrino oscillations, we can constrain it to be zero. Under this additional constraint, the asymmetries become

$$\begin{aligned} A_{CC} &= -0.037 \pm 0.063(\text{stat.}) \pm 0.032(\text{syst.}) \\ A_{ES} &= 0.153 \pm 0.198(\text{stat.}) \pm 0.030(\text{syst.}). \end{aligned} \quad (2)$$

The day and night CC spectra assuming the constraint $A_{NC} \equiv 0$ are shown in Fig. 2.2-1.

The day-night asymmetry results from the salt phase are consistent with no asymmetry, and also with the predictions from the best-fit MSW model.

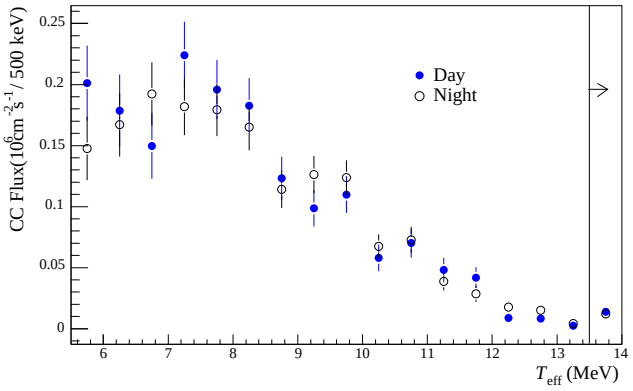

Figure 2.2-1. Day and night electron energy spectra from the CC reaction in the salt phase of SNO.

[1] LANL arXiv:nucl-ex/0502021

2.3 Cosmic ray studies at the Sudbury Neutrino Observatory

J. A. Formaggio

High energy muons and neutrinos are produced constantly by the interaction of primary cosmic rays with nuclei of the Earth's upper atmosphere. These primary interactions produce mesons (e.g. π, K and short-lived charmed D mesons) which decay into neutrinos and muons.

$$p + {}^{14}\mathrm{N} \rightarrow \pi^+(K^+) + X \quad (1)$$

$$\pi^+(K^+, D^+) \rightarrow \mu^+\nu_\mu \quad (2)$$

$$\mu^+ \rightarrow e^+\nu_e\bar{\nu}_\mu \quad (3)$$

At the depth of 2092 meters, where the Sudbury Neutrino Observatory is located, only muons and neutrinos are able to penetrate. SNO is currently in a unique position amongst world experiments located underground. At the depth of over 6 km water equivalent, it is the deepest underground laboratory currently in operation. The vertical flux intensity at this depth is $4.1 \times 10^{-10}\mu/\mathrm{cm}^2{\cdot}\mathrm{s}{\cdot}\mathrm{sr}$, which corresponds to a rate of about 3 muons/hour.

SNO can make two important measurements with respect to muons present in the detector. First, SNO is sensitive to the downward muon rate coming from primary cosmic ray interactions. The muon rate is expected to fall rapidly as a function of depth:

$$I_\mu(h) = A_\nu(\frac{h_0}{h})^\alpha \exp(-\frac{h}{h_0}) \quad (4)$$

where h is the depth of rock, and h_0 is the scale height, both measured in $\mathrm{hg/cm}^2$. By measuring the muon flux as a function of zenith angle, it is possible to test predictions regarding the energy dependence of the muon flux at the surface, as well as the transport mechanism of extremely high-energy muons.

Second, SNO's unprecedented depth allows for an unprecedented measurement of atmospheric neutrinos (via the detection of neutrino-induced muons)at inclinations as large as $\cos(\theta_{\mathrm{Zenith}}) \simeq 0.4$. These atmospheric muon neutrinos can interact with the rock around SNO. They produce penetrating muons that travel up to 10 km w.e. The predicted rate of neutrino-induced muons is about 120 muons/year and, as such, it is mainly a statistics limited measurement. This rate is small compared with the downward muon rate, but SNO's angular resolution is sufficient to make a clean separation at an angle of $\cos(\theta_{\mathrm{Zenith}}) \leq 0.4$. This feature is very important; all comparable experiments are at a much shallower depth than SNO and, thus, cannot distinguish neutrino-induced muons above the horizon. SNO's unique niche allows it to make important model-independent checks of atmospheric neutrino oscillations.

SNO is progressing forward in making a measurement of both the downward and upward cosmic ray muons. Since our last report, the analysis has made significant progress toward

completing this analysis. Some of the recent advances include establishing a blindness criterion for the data set, examining in detail the backgrounds and efficiencies of the muon track fitter, completing and verifying the Monte Carlo simulations of both downward and upward-going muons, and developing software to extract information on the atmospheric oscillation parameters. An expected sensitivity curve, based on the available 800-day dataset, is shown in Fig. 2.3-1 (statistical errors only).

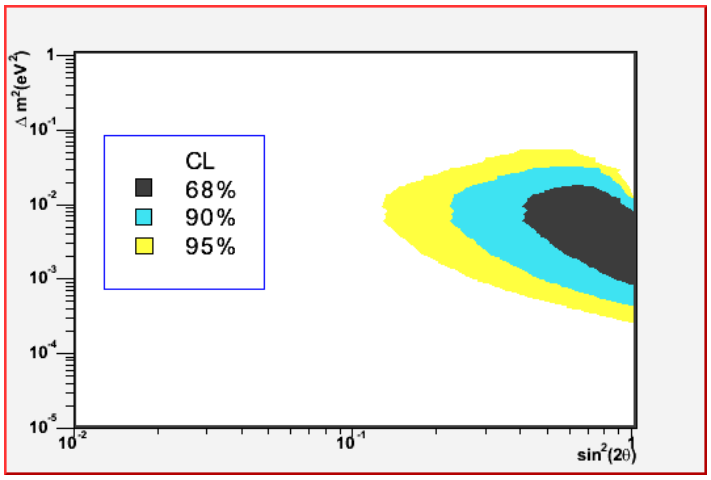

Figure 2.3-1. Projected atmospheric neutrino oscillation parameter sensitivity for SNO's accumulated 730 day data set. Colored bands show signal for different confidence levels. Fit is based on current best fit from the Super-Kamiokande experiment. Only statistical errors are included.

SNO Neutral Current Detectors (NCDs)

2.4 Commissioning of the NCD Array for SNO's Phase III

G. A. Cox, M. A. Howe, S. McGee, A. W. Myers, N. S. Oblath, R. G. H. Robertson, K. Rielage, L. C. Stonehill, B. L. Wall and J. F. Wilkerson

On April 21, 2004, removal of the Remotely Operated Vehicle (ROV)[1] signaled the completion of installation of 36 strings of ^{3}He and four strings of ^{4}He proportional counters to the Sudbury Neutrino Observatory (SNO). This array of Neutral Current Detectors (NCD's) was designed to capture neutrons generated in the neutral current interaction of solar neutrinos with SNO's 1000 metric tons of D_2O. The completion of installation marked the beginning of the commissioning phase of the NCD array.

There are two independent data acquisition paths in the NCD system: fast (shaper) and slow (multiplexing or MUX). Each path has a separate triggering system that was calibrated during the commissioning phase. The shaper system triggers were set with the use of a neutron source. Limits on the range of the neutron energy spectrum (191 keV to 764 keV) could be used to calibrate the distribution of shaper events. This allowed us to set the shaper thresholds on each channel well below the lower edge of neutron events but still above any low energy background events. Independently, the MUX thresholds were set to optimize the ratio of acceptance of pulser events set to mimic the lowest amplitude neutron pulses to electronic noise. This ratio was improved through increasing signal gain by raising the operating voltage of the NCDs from 1846 V to 1950 V. To monitor the stability of these thresholds, a set of electronic calibration (ECA) procedures were developed. These ECA runs are performed once a week by detector operators.

The current analysis plan requires that there is a shaper event (energy measure) associated with each MUX event (scope trace). The measure of this is known as the MUX/shaper correlation efficiency and is optimized by minimizing the MUX thresholds for each channel and maximizing the MUX livetime. The MUX/shaper correlation efficiency was measured to be 95% and 97% with ^{252}Cf and AmBe neutron sources, respectively.[2] The variation in this number is due to the nature of neutrons released in each of these sources.

In addition, source runs were used to determine the stability of the NCD array and the overall neutron capture efficiency. It was determined that the neutron capture efficiency for a source placed in the center of the array is 58.5%.[2] This efficiency is later corrected through MC simulations to represent the neutron capture of neutral current events distributed throughout the D_2O volume.

Before entering the production data taking phase, an analysis meeting was held at the University of Washington. This was to insure that before the data was subjected to the SNO blindness scheme, all necessary neutron and electronic calibration schemes had been developed and that there was an adequate understanding of physical and instrumental backgrounds. The blindness scheme was implemented on January 3rd, 2005.

[1] CENPA Annual Report, University of Washington (2003) p. 30.

[2] Internal SNO document: "Report from the NCD Commissioning Analysis Workshop."

2.5 Calibration of delay line lengths for use in determining event positions in NCDs

S. McGee, R. G. H. Robertson, L. C. Stonehill, T. D. Van Wechel and J. F. Wilkerson

A determination of the z-position of events in the Neutral Current Detector (NCD) array of the Sudbury Neutrino Observatory (SNO) will assist in the identification of backgrounds from neutrons generated on or near SNO's acrylic vessel (AV) and allow for a measurement of neutrons per fiducial volume of heavy water. To assist in the determination of z-position a long wire non-inductively wound on a Kapton medium is added to the base of all 40 deployed NCDs. This addition is referred to as the delay line. The delay line adds a fixed time delay to the z-dependent time delay between the initial pulse and its reflection from the bottom of the open-ended NCD configuration, making it easier to resolve the two pulses.

The goal is a 1 m resolution on the z-position of an event. This is equivalent to the x and y resolution since the NCDs were deployed in a 1 m grid centered on the central axis of the AV. Part of resolution along the z-axis will come from methods used to determine the pulse-reflection separation and part will come from the uncertainty with which the true length of the delay line is known.

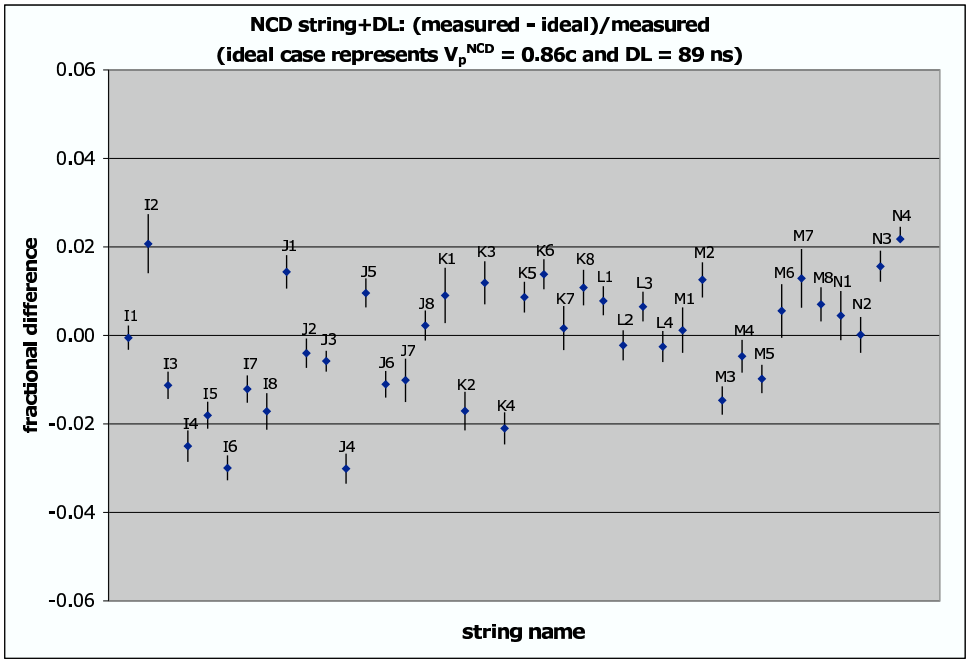

Figure 2.5-1. Comparison of measured NCD string plus delay line lengths to those expected with the V_p^{NCD} and length of delay line measured in the lab.

To check the delay line lengths, a narrow (20 ns) square pulse was injected at the preamp of each of the NCDs. This square wave then travels down the length of the NCD readout cable until reaching a large impedance mismatch at the top of the NCD. Part of the pulse reflects back up the cable while another part continues to travel down the length of the NCD

and delay line. The time difference between these two pulses can be used to check the lengths of the delay lines.

For comparison purposes, the velocity of propagation through the NCD counters (V_p^{NCD}) and a standard delay line length (DL) were measured at the UW test stand. The results were $V_p^{NCD} = 0.86c$ and DL = 89 ns. Since the length of the active sections of the NCDs is well known, a comparison of the expected NCD string plus DL using these values (the 'ideal case' in Fig. 2.5-1) to the measured pulse-reflection time difference will be a measure of the actual delay line length.

As seen in Fig. 2.5-1, the variation of the DL values is less than 3%. This equates to a potential uncertainty in z-position of 35 cm due to delay line variations. The largest variations (>2%) are seen in the I and J strings. This is believed to be due to a limitation of the narrow pulse method where a resonant combination of reflections is shifting the pulse-reflection peak to peak difference to larger values. As a double-check of this method, since α events are thought to be spread evenly along the z-direction of the NCD counters and a large fraction of α events has clearly distinguishable pulse-reflection peaks, it is believed that α pulses can be used to confirm the values of V_p^{NCD} and DL.

2.6 Alpha backgrounds in the NCDs

G. A. Cox, J. A. Detwiler, P. J. Doe, S. McGee, N. S. Oblath, K. Rielage,
R. G. H. Robertson, L. C. Stonehill and J. F. Wilkerson

The primary physics background to the NCD neutron signal is alpha events from ^{238}U and ^{232}Th decays in the nickel walls of the NCDs. In order to limit the photodisintegration neutron background from gammas in the ^{238}U and ^{232}Th decay chains to fewer than one per day, the NCD construction specifications called for fewer than 24 parts per trillion (ppt) of ^{238}U and fewer than 2 ppt of ^{232}Th in the NCD nickel. The ^{238}U and ^{232}Th are assumed to be uniformly distributed throughout the nickel walls of the NCDs and the decay chains are assumed to be in equilibrium. Alphas produced by ^{238}U and ^{232}Th decays have energies from about 4 MeV up to almost 9 MeV, well above the 764-keV Q-value of the ^{3}He(n,p)^{3}H reaction. However, the alphas lose energy escaping from the nickel walls and can strike another part of the wall before stopping in the gas, so about 10% of alpha events have energy below 1 MeV, where they are a potential background to the neutron signal. In addition to the ^{238}U and ^{232}Th bulk contamination of the nickel, there is ^{210}Po surface contamination that was introduced when the nickel tubes were inadvertantly stored in a high-radon environment during construction. The ^{210}Po decays produce a 5.3 MeV alpha line, which has a lower-energy tail due to alphas that strike the NCD wall before depositing all of their energy in the gas. The total rate of alpha events in the NCD array is on the order of 200 events per day.

In order to understand the levels of these alpha contaminants, the expected energy distributions of bulk ^{238}U chain alphas, bulk ^{232}Th chain alphas, and surface ^{210}Po decays were simulated. The ^{210}Po simulation included the effects of space charge, which occur when the electric field near the anode wire is modified by the presence of positive ions produced in the avalanche. Data taken from the NCD array in SNO were fit with these simulated spectra. An overall multiplicative shift in the energy scale was a free parameter in the fit, since the energy scale of the NCD Shaper/ADCs has not yet been fully characterized. The best-fit values from the fit shown in Fig. 2.6-1 indicate that the ^{238}U contamination of the nickel is 2.6 ± 0.2 ppt and the ^{232}Th contamination is 1.2 ± 0.5 ppt (uncertainties are statistical only). These values are below the construction specifications and are in good agreement with results of direct assay of the nickel during construction, which indicated that the ^{232}Th contamination is 1 ± 1 ppt. In addition, these results are in agreement with results of a previous analysis using time coincidences between short-lived alpha emitters in the ^{238}U and ^{232}Th decay chains, which indicated that the ^{238}U contamination is < 6 ppt and the ^{232}Th contamination is 0.4 ± 0.2 ppt.

The expected neutron signal in the NCDs is only a few events per day, compared to the alpha background of about 200 events per day, about 20 of which are in the energy region where neutron events are expected. Because of the small signal-to-background ratio, identification of neutron events through pulse shape analysis is very helpful for signal extraction. The width of the digitized current pulse from an NCD event is a good parameter to use in pulse shape discrimination. Because neutron captures on ^{3}He produce two back-to-back low-ionizing particles (a proton and a ^{3}H), neutron pulses can be wider than the widest possible alpha event of the same energy. In pulse width vs. energy space, up to about 50% of neutrons

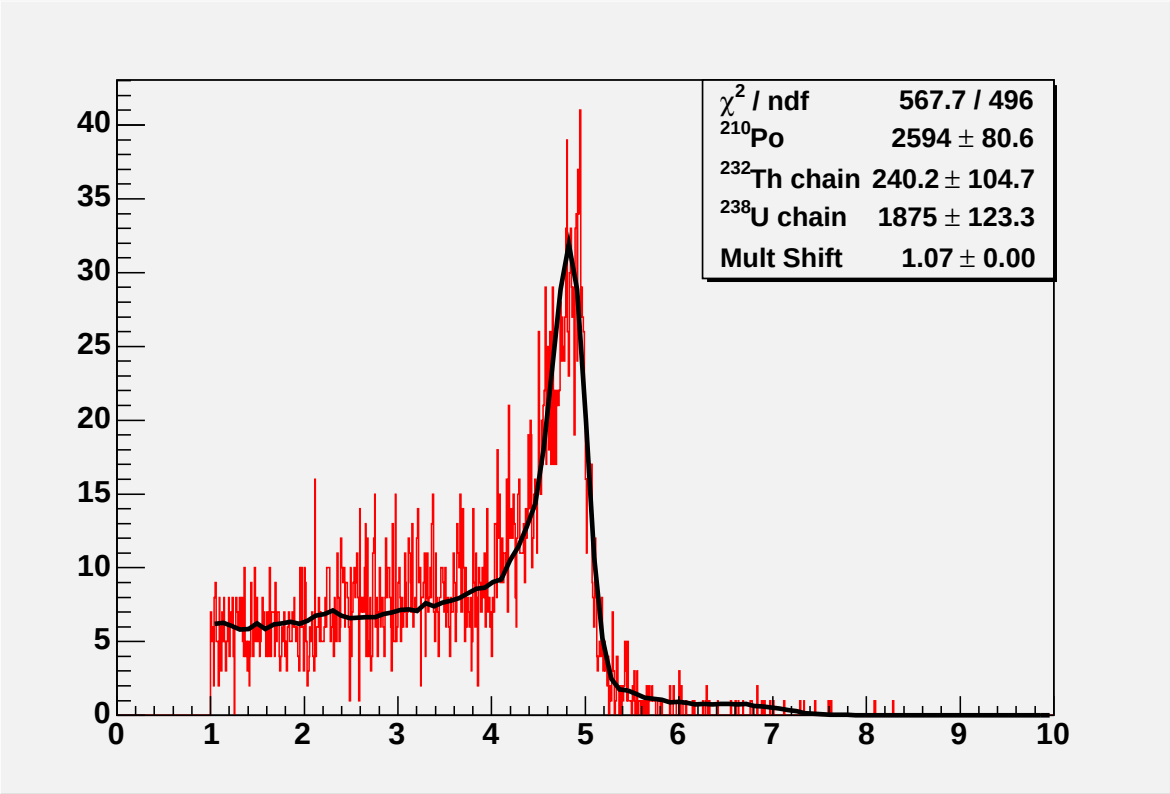

Figure 2.6-1. NCD alpha energy spectrum, fit with simulated spectra from the ^{238}U chain, the ^{232}Th chain, and surface ^{210}Po.

fall into a region free of alphas. Another technique under investigation to distinguish neutron events from alphas is the use of a pulse-shape fitting routine. It is based on semi-analytic functions that describe the expected signal from neutrons and alphas. A likelihood that an event is a neutron can be assigned based on the goodness-of-fit with the expected neutron and alpha signals. Both the pulse width vs. energy technique and the fitting technique require good understanding of the effects of the electronics on the NCD pulse shapes, which is where much of the current analysis effort is focused.

2.7 Estimation of deployed NCD tilts in SNO

J. F. Amsbaugh and J. Heise*

Each neutral current detector (NCD) position in the heavy water of SNO is determined by its anchor point (AP) which was bonded to the acrylic vessel (AV) during construction. The buoyant NCDs should be aligned vertically above its AP, but an NCD readout cable can pull it toward the center at the top if the cable's run constraints are not placed correctly. The global view camera (GVC), being near the central axis, can only resolve an extreme tilt. It was decided a limit on this possible misalignment was very desirable before finishing the NCD deployment.

A laser range finder (LRF) was designed and built to SNO cleanliness standards. It attaches to the deployment boathook and extends beyond the bottom of the AV chimney. The LRF made the boathook assembly negatively buoyant providing the vertical axis and the swivel were replaced with a fixed bearing and angle readout vernier. The laser[1] beam points down to a splitting prism and one arm then turns off a first surface mirror to provide two beams crossing about 113 inches from the vertical axis in the vertical plane with a known baseline for triangulation. Normal acrylic exit windows prevent beam deflection from acrylic–heavy water interface refraction. A battery pack provided more than ten days continuous operation. The layout is illustrated in Fig. 2.7-1.

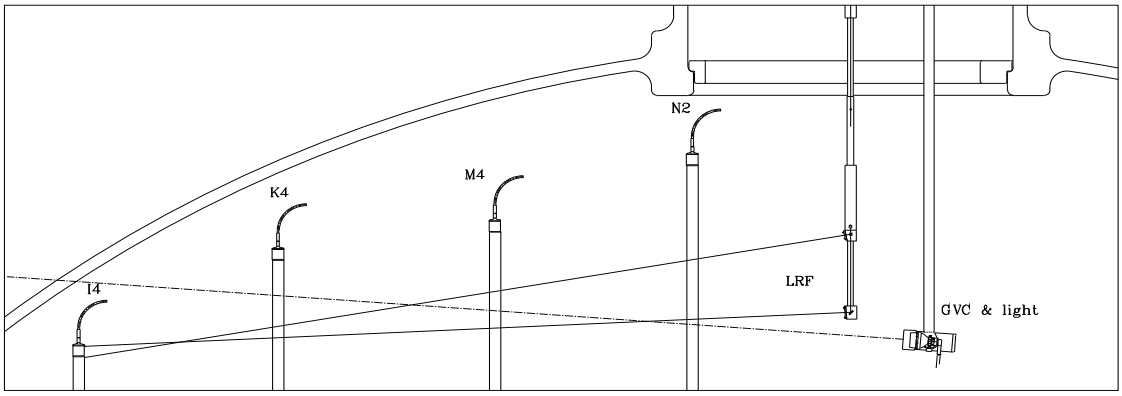

Figure 2.7-1. The laser range finder pointed at NCD string I4 and the GVC pointed at M4. Readout cables truncated.

To measure a tilt, one turns the LRF until the spots are centered upon the target NCD, with the NCD also centered in the GVC image. Capture the video image and record the LRF angle and GVC angles. Later the images are converted to 8 bit gray scale, analyzed with imaging software[2] to measure the spot separation and NCD tube width in pixels. Since the NCD width is known, the range can be estimated. Due to automatic exposure controls many images have low contrast near the NCD edges. Several contrast enhancements are

*Los Alamos National Laboratory, Los Alamos, NM 87545.

[1]Diode module from Infiniter pointer, QPON-650-100 CLIIIa, 650 nm, $\leq$4mW.

[2]Sherlock Professional, available from Coreco Imaging, Inc.(978)670-2000.

applied and the best one is chosen by checking the edge detection algorithm output for bias and bright spot rejection. With the GVC and light offset from each other and from the LRF axis, some NCDs are shadowed or behind another NCD. For these cases, the LRF was raised 3-inches and a second image captured to provide image pixel scaling.

The LRF was commissioned on 25-March-2004, and it found NCD string I4 looked like a J string, clearly tilted. The cable constraints were found to be 13-inches off and this was fixed. A complete set of LRF measurements were taken on 5-April-2004. A careful GVC survey (pan and tilt angles) of the NCD tops and bottoms was done along with LRF measures of the visible 14 out of 20 AV suspension ropes. Analysis and cross checking is nearly done and a report will be available. Fig. 2.7-2 is a typical analysis with $\rho = 61.5$-inches equal to AP $\rho = 62.5$-inches less 1.0-inch NCD radius.

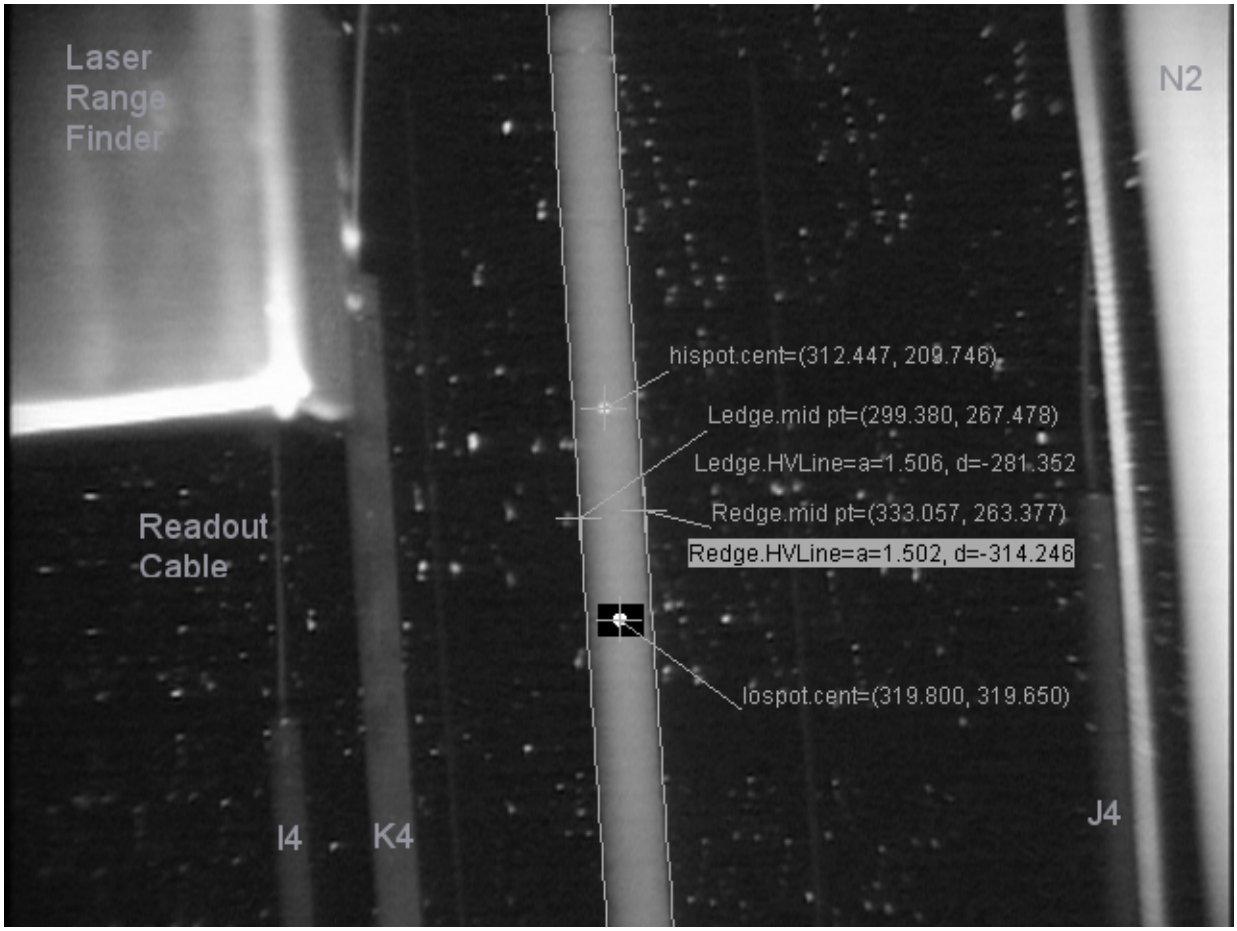

Figure 2.7-2. The captured image for measuring M4 NCD string tilt with image analysis edges and spot centroids overlayed. The lower spot shows the threshold result used. Note the LRF in upper right, and other NCDs with readout cables are visible. The white streak near N4 is a rope used to haul the NCDs down during deployment. The background spots are reflections from PMT collectors.

2.8 PMT calibrations for the NCD phase of SNO

C. Kraus,* I. Lawson,† N. S. Oblath and A. W. P. Poon‡

The timing and gain calibrations of the SNO PMT array are performed using a nearly-isotropic light source that can be moved to different locations within the detector. The light source is a pulsed nitrogen/dye laser system which can operate at six different wavelengths. An acrylic diffuser ball, called the laserball, is used to isotropically (to $\approx 10\%$) distribute the light.

During the previous two phases of SNO the laserball was placed at the center of the detector. During the NCD phase, however, since the NCDs cast shadows on the PMTs, the laserball must be placed in multiple locations to illuminate all PMTs. Over the past year the simulations[1] used to determine the ideal laserball locations were refined and it was found that by placing the laserball in the center of the detector and 24 cm offset along the x or y axis 99% of the PMTs receive sufficient light to be calibrated successfully. An example of simulated shadows is shown in Fig. 2.8-1. If only one of those two positions is used, approximately 80% of the PMTs are correctly calibrated.

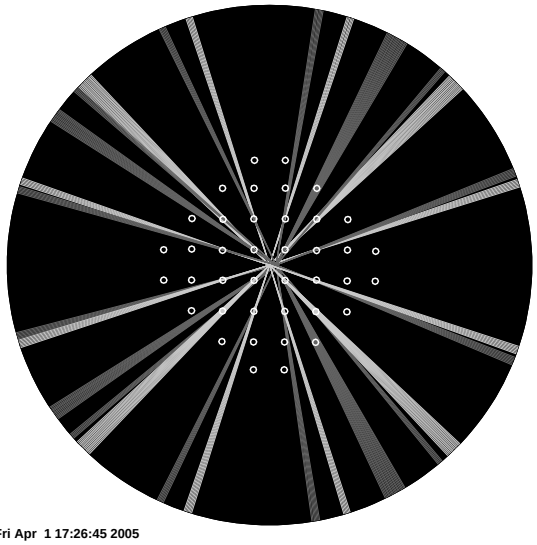

Figure 2.8-1. Simulation of shadows from the ideal laserball positions, (0,0,0) cm and (24,0,0) cm. All NCD positions are indicated, but only shadows from the central 16 NCDs are shown.

We have been working on verifying the accuracy of this 2-point PMT calibration. This has involved reconstructing the position of the laserball based on the timing of the PMT signals, as well as reconstructing events from the ^{16}N calibration source. Preliminary results from these verification procedures have shown that the 2-point PMT calibration works well and that, with a few minor refinements, it will be ready for use during the NCD phase.

*Queens University, Kingston, Ontario, Canada K71 3N6.
†University of Guelph, Guelph, Ontario, Canada N1G 2W1.
‡Lawrence Berkekely National Laboratory, Berkeley, CA 94720.
[1]CENPA Annual Report, University of Washington (2004) p. 24.

2.9 Development of NCD burst cuts

G. A. Cox, P. J. Doe, S. McGee, N. S. Oblath, K. Rielage, R. G. H. Robertson, L. C. Stonehill and J. F. Wilkerson

The first major step in the analysis of data from the SNO NCDs is the development of data-cleaning cuts to remove instrumental backgrounds from the data. There are two primary types of data-cleaning cuts: cuts that remove specific types of events based on pulse shape (these cuts are primarily being developed at other institutions in the SNO collaboration) and cuts that remove high-rate bursts of data. High data rates can be caused by high-voltage breakdown in the SNO photomultiplier tubes (PMT), blasting and rockbursts in the mine environment, or high-voltage discharging events in the NCD string itself. The only known physics events in the NCDs that occur in bursts are neutrons following cosmic-ray muons, which are identified by the muon signal in the PMT array and removed from the data, and galactic supernovae, which would be identified by the supernova trigger system. Other periods of high data rates are caused by undesirable instrumental backgrounds and should be removed. Since the PMT system also experiences instrumental background bursts, code that can identify and flag bursts already exists in the SNO analysis software. Thus, development of burst cuts for the NCDs simply requires the determination of the appropriate type, size, and duration of a burst to be cut.

Two different types of NCD burst cuts have been developed, a general cut that removes bursts of four or more events in 0.1 s, and another cut that removes discharge events that occur after a very large high-voltage discharge on an NCD string. The 0.1 s burst cut is implemented as two separate cuts, one for Shaper/ADC events and one for digitized events. The bursts cut by the 0.1 s cut range in size up to about 50 events and occur once or twice a day. The other cut is implemented by removing a fixed amount of time before and after any event that falls into the overflow bin in the Shaper/ADCs. Before the event, 15 μs are cut, in order to remove the digitized event associated with that Shaper/ADC event, which typically falls 8 μs prior to the Shaper/ADC event. After the event, 5 ms are cut, to remove smaller discharge events that follow the large primary discharge on the same string. The number of follower discharge events ranges from zero up to about ten. Large discharges in the Shaper/ADC overflow bin occur about four times a day, primarily on the J1 (about three per day) and M7 (about one per day) strings. Overall, the amount of livetime removed by these two burst cuts is very small, typically less than one second per day.

2.10 SNO NCD DAQ and electronics improvements

G. A. Cox, M. A. Howe, S. McGee, A. W. Myers, K. Rielage, R. G. H. Robertson, L. C. Stonehill, T. D. Van Wechel, B. L. Wall and J. F. Wilkerson

A number of improvements have been made to the SNO NCD electronics since the completion of the NCD installation phase.[1] The electronics for the NCDs are composed of two main systems: a digitized data path utilizing 40 multiplexer channels that can be sent to two different oscilloscopes and 40 shaper channels that return a total integrated charge for the event.

The most significant hardware change to the SNO NCD system was the development of a 32-bit NCD trigger card with several features that were not in the original trigger card. This new trigger card includes a 10-MHz clock that can be used in place of the SNO MTC clock in the event of the PMT system being unavailable due to maintenance or power conservation during power outages. The trigger card also utilizes this clock to evaluate the livetimes of the three NCD system components: the multiplexer, the shapers, and scopes. This allows for an accurate accounting of the system deadtimes.

Two additional methods of determining the system deadtime have also been implemented. The shaper system includes a scaler counter for each channel. This counter has a very small deadtime (<6 μs) so it can provide the total number of shaper events that the system received even while the shaper channel is waiting to be read out. The optimization of the scaler counter threshold circuit was completed this past year and implemented in the SNO NCD system. A second method to determine deadtime is to utilize a random pulser. Ideally one should use a random pulser with a rate similar to the total data rate. For the SNO NCD system this requires a pulser capable of producing a rate of 0.01 Hz as well as a faster rate (for independent measurements) up to 10 kHz. Such a pulser was designed and built by the electronics shop at CENPA. Several design iterations resulted in a pulser capable of producing a variable-amplitude negative pulse as well as a TTL pulse for triggering an external pulser.

A large amount of work was also spent in the NCD commissioning phase on electronic noise mitigation. The SNO NCD system was found to be susceptible to noise generated by the SNO PMT system during high digital traffic rates and from other external electronic devices. Improved grounding and shielding helped reduce the noise susceptibility to acceptable levels.

The SNO NCD system utilizes the ORCA software as the data acquisition system. Several improvements were made to the software including the addition of a number of alarms to alert detector operators of various conditions, the addition of software for the new trigger card and to control the random pulser settings, and improvements to the readout speed of the system. One major area of improvement came with solving a low-level driver register instability problem during accesses to the VME electronic crates. By changing the timing in the driver to wait for stability ORCA is now able to utilize the capability of dual processor machines and thus achieve a significant improvement in readout speed.

[1] CENPA Annual Report, University of Washington (2004) p. 25.

2.11 NCD electronics calibration

G. A. Cox, M. A. Howe, S. McGee, A. W. Myers, K. Rielage, R. G. H. Robertson, T. D. Van Wechel and J. F. Wilkerson

The NCD electronics calibration plan is now a fully automated routine that is processed weekly at SNO. There are now three types of electronics calibrations routines that are performed regularly - calibration of the logarithmic amplifier, and measurements of the linearity and thresholds of the VME-based shaper/ADC cards and the multiplexers. Each of these routines generally consist of injecting each NCD electronics channel with a sufficient number of known pulses and then analyzing the measurements made by the shaper/ADC and multiplexers. Extended calibrations are performed monthly where a larger than normal number of pulses are injected into the system in order to make a more precise characterization of the system. The monthly occurrence of these calibrations is due to the significant amount of time they require to perform, which cuts into our live-time. Square waves of various amplitudes are injected into the system in order to perform the linearity and threshold measurements. The total charge of the waveforms injected for the linearity calibration cover the energy range of the physics event energies in the NCDs. For threshold calibration, a series of low amplitude offset sine waves (such that the entire pulse is at or below baseline) are injected in order to measure at what amplitude they cease to be recorded by the electronics. The logarithmic amplifier characterization is done by injecting an offset sine wave and then performing a χ^2 minimization to fit to the shape of the measured signal Lto extract the parameters which characterize the amplification.[1]

Over the past year, significant improvements in our understanding of the overall effect of the NCD electronics chain on our event waveforms have been made. This includes a more detailed model of the equivalent electronics circuitry, more accurate measurements of our allowed bandwidth and its effects on signal transformation, and improved understanding of small impedance mismatches in our system that produce reflections of the injected signals.

The parameters which characterize the signal transformation have been shown to be stable since major configuration changes to the NCD electronics setup were completed. The parameters have been shown to be stable over the time range of an hour, a week and a month and do not fluctuate significantly within the typical temperature range of the SNO underground laboratory.

Due to the complexity of modeling the system, we were motivated to calibrate the logarithmic amplifiers with an alternative method which uses the waveforms injected for the linearity calibration. This method has been successful (though still very much under development) and agrees well with the χ^2 minimization method that requires a more detailed model of the signal transformation.

[1] CENPA Annual Report, University of Washington (2004) p. 23.

2.12 ^{3}He assay system for SNO

R. Ford,* N. S. Oblath and R. G. H. Robertson

The Neutral Current Detector (NCD) array is a set of 36 'strings' of ^{3}He proportional counters that has been installed in the heavy-water volume of SNO. ^{3}He was used because it has a high cross section for thermal neutron capture (5330 barns) relative to that of deuterium (5.21×10^{-4} barns). While the ratio of neutron capture cross sections is favorable for detecting neutrons with the NCDs, it also means that even a tiny amount of ^{3}He dissolved in the heavy water (from a leaking NCD, for example) could significantly affect the Neutral Current cross section of the detector.

We have designed and built the ^{3}He assay system to measure the amount of ^{3}He in the heavy water. The assay system will be integrated into the SNO heavy water degassing system. The gas flow from the degassing system, containing any ^{3}He that was in the water, is passed over the outsides of heated quartz tubes, which are permeable to helium and have a high vacuum inside. Any ^{3}He in the high-vacuum region is detected with a residual gas analyzer (RGA). A schematic of the system is shown in Fig. 2.12-1.

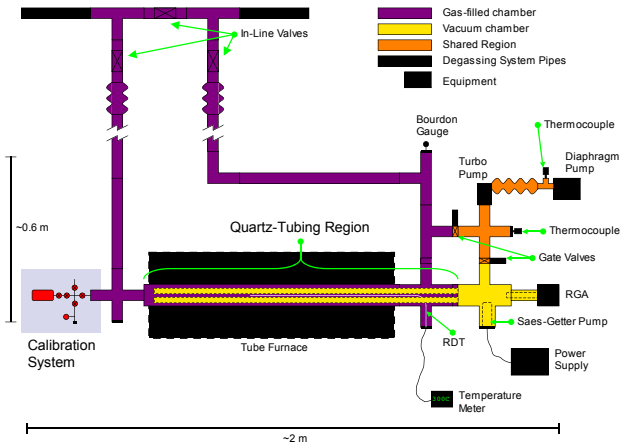

Figure 2.12-1. Schematic diagram of the ^{3}He assay system.

A turbomolecular drag pump is used to achieve the high vacuum. Since quartz is also permeable to hydrogen and deuterium, HD molecules, which are also mass-3, could interfere with our measurement of ^{3}He. We use a getter pump to remove any HD in the high-vacuum region, before it reaches the RGA.

Work on designing the assay system began during the Summer of 2004, and construction was completed in February, 2005. Preliminary tests were done to verify that the components worked correctly, and the entire system was shipped to Sudbury for installation in March. Further tests and calibrations are planned once the assay system is installed.

*Sudbury Neutrino Observatory, Lively, Ontario, Canada P3Y 1M3.

KATRIN

2.13 The CENPA contribution to the KATRIN neutrino mass experiment

T. H. Burritt P. J. Doe, J. A. Formaggio, G. C. Harper, M. A. Howe, M. L. Leber, A. W. Myers, K. Rielage, R. G. H. Robertson, T. D. Van Wechel and J. F. Wilkerson

The Karlsruhe Tritium Neutrino (KATRIN) experiment[1] is the next generation tritium beta decay experiment which is designed to make a direct measurement of the neutrino mass. The experiment is expected to achieve a sensitivity of m(ν_e)= 0.2 eV (90 % C.L.) on the mass of the neutrino, corresponding to a 5σ discovery potential for m(ν_e)= 0.35 eV. This represents an order of magnitude improvement over current limits on the neutrino mass and a significant improvement over the original Letter of Intent. This level of sensitivity will allow KATRIN to probe the quasi-degenerate neutrino mass scenario and the full cosmologically relevant neutrino mass range. The experiment is expected to begin taking data in Fall 2008 and run through 2115. A schematic of the layout of the KATRIN experimental facility is shown in Fig. 2.13-1

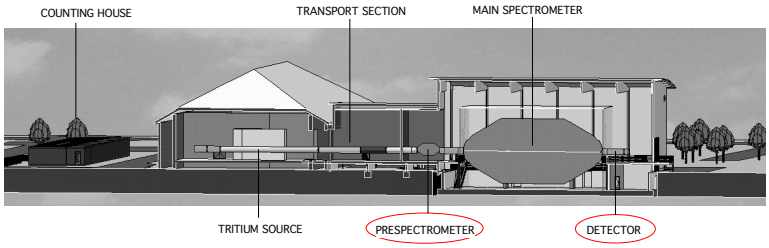

Figure 2.13-1. Layout of the KATRIN experimental facility. In addition to the data acquisition system, CENPA is responsible for providing components of the pre-spectrometer and the entire detector system

The KATRIN experiment, shown above, is located adjacent to the Karlsruhe Tritium laboratory which has the license and expertise to handle the large quantities of tritium required by the experiment. CENPA is responsible for providing the following components of the experiment:

- The real-time data acquisition system. This is based on the object-orientated ORCA system that CENPA developed for the SNO NCD data acquisition system. To date we have provided a 64-channel system used to evaluate the prototype detector for the pre-spectrometer.
- An electron gun used to evaluate the possible solid state detector arrays for use as the focal plane detector for the main spectrometer.

[1]The present collaboration: Univ. of Bonn; CCLRC Daresbury Laboratory; Joint Institute for Nuclear Research Dubna; Univ. of Applied Science (FH) Fulda; Forchungszentrum Karlsruhe; Univ. of Karlsruhe; Johannes Gutenberg Univ, Mainz; Univ. of Muenster; Institute for Nuclear Research, Moscow; Nuclear Physics Institute, Prague; Rutherford Appleton Laboratory; University of Wales, Swansea; Center for Experimental Nuclear Physics and Astrophysics, Univ. of Washington.

- A low mass electrode system for the pre-spectrometer that is used to reduce backgrounds and will serve as a prototype for the main spectrometer electrode. This has been manufactured at CENPA and delivered to Karlsruhe.

- The focal plane detector for the main spectrometer. This is the major contribution of CENPA to the KATRIN experiment. It consists of a 700 pixel, 10 cm diameter solid state detector located inside a 6T superconducting magnet. Electrons falling on this detector will be accelerated by $\approx$ 30kV to raise them about background. The entire system is located in a 10^{-11} mbar vacuum. The detector system will be delivered to Karlsruhe during spring/summer of 2008.

2.14 Optimization of the KATRIN detector shielding using Geant4

J. A. Formaggio, M. L. Leber, R. G. H. Robertson and J. F. Wilkerson

The KATRIN (KArlsruhe TRItium Neutrino) Experiment will fix or limit the neutrino absolute mass scale with an order-of-magnitude-greater sensitivity than previous beta decay experiments. To achieve such high precision, an overall background count rate of less than one milliHertz is required in the region of interest. For an above-ground experiment, a large contribution to the background comes from cosmic rays, and shielding becomes increasingly important. At the University of Washington, we are investigating active and passive shielding to reduce the background contribution from cosmic rays and environmental radioactivity in the detector area. By simulating these sources, the material's shielding effectiveness can be balanced against the possibility of increasing backgrounds by introducing natural radioactivity or by muon activation.

Geant4 Monte Carlo simulates a flux of cosmic rays or other radiation incident on a simplified KATRIN shielding and detector geometry. Relevant physics processes are used to calculate the energy deposition in the detector array. Acceleration of the tritium beta-decay electrons past the endpoint energy is assumed, but electric and magnetic fields are not included. Concentric layers of shielding surround the silicon detector array. Closest to the detector is the gamma shield for which lead, copper or tungsten are being considered. Scintillators, along with potential neutron shields of cadmium foil and either lithium- or boron-doped polyethylene follow. The neutron flux is representative of the total neutron production at the air-ground boundary[1] and is assumed to be isotropic. Cosmic-ray muons[2] are considered primary background events, but muon activation in the shielding material is not yet included. Existing code is used to generate the decay products from the ^{238}U and ^{232}Th chains. Design goal limits on the ^{238}U and ^{232}Th content of the detector magnet, vacuum tube, and shielding materials can be calculated from the count rates in the region of interest. Preliminary results are given in the table. The assumed impurity of the copper shield is one part-per-trillion, and one part-per-billion for the stainless-steel[3] vacuum tube. This work can be extended to validate the Monte Carlo estimations of the energy deposition from ^{238}U and ^{232}Th decay products in silicon detectors with the KATRIN electron gun.[4]

Source	Shielded	Unshielded	Material
Neutrons	1.3 mHz	2.1 mHz	Polyethylene-Boron
Muons	6.6 mHz	2.7 mHz	Tungsten
Magnet ^{232}Th ^{238}U	0.00035%	0.0047%	copper
Shield ^{232}Th ^{238}U	1.0 μHz	0	copper
Vacuum Tube ^{232}Th ^{238}U	0.57 mHz	0.57 mHz	steel

Table 2.14-1. Effect of shielding on the background count rates in the region of interest 25-50 keV.

[1] M. Yamashita, L. D. Stephens, and H. W. Patterson, J. Geophys. Res. **71**, 3817 (1966).
[2] S. Miyake, PICRC, **5**, 3638 (1973).
[3] J. Busenitz, KamLAND US Proposal, (1999) p. 45.
[4] CENPA Annual Report, University of Washington (2003) p. 34 and p. 65.

2.15 Improvements to the KATRIN electron gun

P. J. Doe, J. A. Formaggio, G. C. Harper, M. A. Howe, M. L. Leber, K. Rielage, R. G. H. Robertson, J. F. Wilkerson and the KATRIN Collaboration

To aid in the characterization of the detector component of the KATRIN experiment a monoenergetic electron gun has been built at UW[1] capable of producing electrons with energies up to 30 keV. These electrons are used to examine the deadlayer thickness, the energy resolution and the backscatter properties of several test detectors.

A new detector test chamber (see Fig. 2.15-1) is being built to accommodate detectors up to 10 cm x 10 cm in active area. An X-Y translation stage is being mounted inside the chamber to allow for precision movement of the detector along with the capability of rotating the stage for deadlayer measurements. A 64-pixel silicon detector made by Canberra has been acquired by the KATRIN collaboration and will be sent to UW for testing shortly. Final designs are being completed to handle the flexible cabling for the detector and the cooling to -100^0 C and modifications to the gun will be made to produce electrons with energies up to 50 keV.

The previous detector chamber was used this past summer by an REU student to make detailed measurements of the backscattered electrons as a function of angle from a silicon PIN diode detector. These data are being compared to simulations in an effort to validate the simulation code before being used on the final detector design.

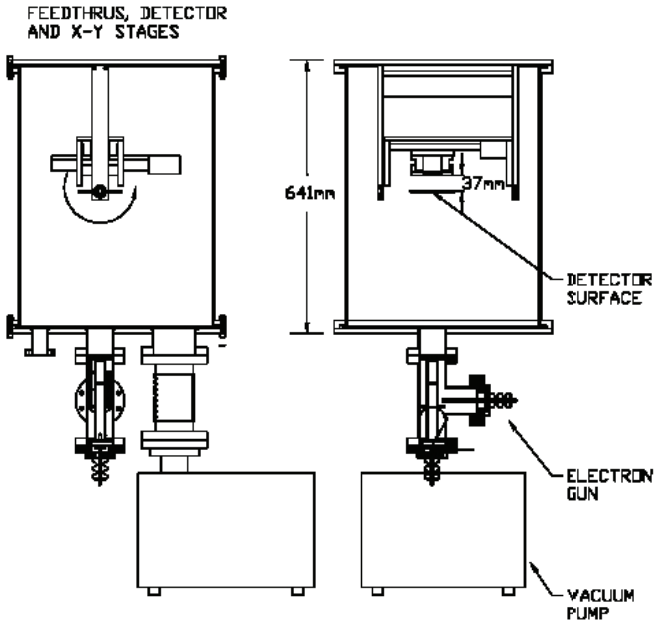

Figure 2.15-1. Design of the new electron gun detector chamber.

[1]CENPA Annual Report, University of Washington (2004) p. 27; (2003) p. 65.

2.16 KATRIN pre-spectrometer electrode

T. Burritt, P. J. Doe, J. A. Formaggio, M. L. Leber, K. Rielage, R. G. H. Robertson and J. F. Wilkerson

Both the pre-spectrometer and the main spectrometer contain low mass electrodes. The purpose of these electrodes is to reduce backgrounds coming from natural radioactivity in the walls of the vacuum vessel and electrons trapped in regions of the electric field which later enter the detector. In addition, the electrode further optimizes the shape of the electric field. The electrode installed in the pre-spectrometer will serve as a prototype for the main spectrometer electrode. CENPA delivered the pre-spectrometer electrodeto Karlsruhe in March and it is now in the process of being installed into the pre-spectrometer vacuum vessel. The electrode is shown installed in the vacuum vessel in Fig. 2.16-1.

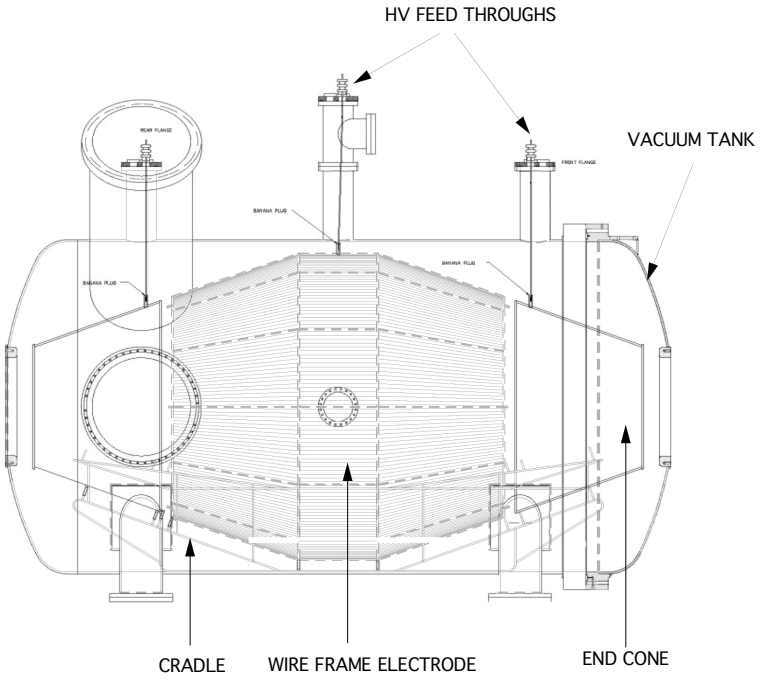

Figure 2.16-1. The pre-spectrometer electrode shown installed in the vacuum vessel.

The electrode must be low mass in order to reduce secondary-emission backgrounds from cosmic and radioactive backgrounds. It is held at a negative potential with respect to the vacuum vessel. Thus any electrons originating from the vessel are repelled back to the vessel and do not enter the spectrometer. Since the electric field profile is not perfect, there exist Penning traps in which electrons may accumulate. These electrons may eventually spill out into the detector, representing a background. Therefore the electrode is divided into two electrically independent halves, allowing a transverse electric field to be applied which sweeps out the trapped electrons. These design features will be tested in the pre-spectrometer and the lessons learned will be applied to the design of the main spectrometer electrode. These tests will be carried out in the summer of 2005 and CENPA personnel will participate.

Majorana

2.17 Majorana double beta decay experiment

J. F. Amsbaugh, P. J. Doe, J. A. Formaggio, R. A. Johnson, K. Kazkaz, M. A. Howe, M. G. Marino, A. W. Myers, R. G. H. Robertson, T. D. Van Wechel and J. F. Wilkerson

The Majorana experiment is a proposed next generation ^{76}Ge 0ν $\beta\beta$-decay experiment. For the first phase of Majorana, we envision an array of 180 kg of 86% enriched ^{76}Ge which provides a sensitivity to neutrino mass in the quasi-degenerate range $\sim$100 meV, while also enabling a stringent test at the 95% CL on the recent controversial claim of Klapdor-Kleingrothaus *et al.*[1] The experiment is envisioned to consist of 170 crystals grouped into a collection of three independent modules. This modular design allows for an optimized measurement plan as the crystals are fabricated and also is scalable to larger masses in the future. Careful attention has been given to controlling intrinsic and external backgrounds and in developing capabilities for measuring the activities of the materials that will be used in the apparatus.[2]

During the past year our efforts at UW have concentrated in the following areas.

- The development of a full "Phase 1" proposal to be submitted by the collaboration to the DOE Office of Nuclear Physics.
- Exploring potential private foundation funding sources that might allow us acquire to a quantity of enriched isotope within a short time frame.
- Studies of alternative cooling and shielding using liquid Ar as an active shield.[3]
- In collaboration with PNNL, we are developing a new sensitive low-background counting system to be installed at the Lower Monumental Dam near Richland, WA.
- Studies of the potential sensitivity of Majorana to 2ν $\beta\beta$-decays of ^{76}Ge to excited states.[4]
- Contributing to the development of the GEANT4 based "MaGe" joint Majorana and GERDA collaborations' simulation framework.

We have recently taken on the responsibility of coordinating the completion of the "Phase 1" proposal that will be submitted to the DOE Office of Nuclear Physics. The proposal is an evolution of the collaboration's "White Paper" written in 2003. As part of these efforts we have been reviewing all aspects of the current reference design. In January, after developing an

[1] H. V Klapdor-Kleingrothaus, I. V. Krivosheina, A. Dietz and O. Chkvorets, Phys. Lett. B **586**, 198 (2004).

[2] These techniques are also directly relevant to future ultra low background counting efforts at a Deep Underground Science and Engineering Laboratory.

[3] These studies have been carried out with our collaborators at Pacific Northwest National Laboratory (PNNL).

[4] These studies have been carried with our collaborators at Los Alamos National Laboratory.

internal UW pre-proposal, we have been selected by the University of Washington to submit a preliminary proposal on behalf of the university to the W.W. Keck Foundation. Our proposal to the Keck Foundation is to provide funds allowing the collaboration to immediately initiate the purchase of 15-20 kg of enriched ^{76}Ge. The goal is to accelerate the experimental schedule, facilitate R&D and demonstrate the ability to obtain the enriched isotope at the requisite purity, thus reducing potential risks for the DOE proposal. More details can be found in subsequent sections on progress with the technical activities.

2.18 Using activated germanium to mimic ^{76}Ge double-beta decays to excited states

S. R. Elliott,* V. M. Gehman,* K. Kazkaz, D. M. Mei* and J. F. Wilkerson

The Majorana experiment[1] is a ^{76}Ge-based search for neutrinoless double-beta ($0\nu\beta\beta$) decay. The nuclear matrix elements governing the rate of double-beta decay are model-dependent. These matrix elements relate the halflife of $0\nu\beta\beta$ decays to the effective Majorana mass of the neutrino, and they currently have a spread of roughly two orders of magnitude.[2] By measuring the ratio of the halflives of $\beta\beta$ decays to excited and ground states, more direction can be provided to improve the nuclear models, reducing the uncertainty in the effective neutrino mass calculation. Two experiments closely related to Majorana are the Multi-Element Germanium Array[3] (MEGA), and the Segmented Enriched Germanium Assembly[4] (SEGA), experiments. The SEGA detector is made of germanium enriched to 86% ^{76}Ge, increasing its rate of double-beta decay events over similarly-sized unenriched detectors. SEGA will be run inside the MEGA annulus, which will in part increase the efficiency for observing cascade gammas derived from $\beta\beta$ decays to excited states.

To determine the sensitivity of the MEGA/SEGA detectors to these decays to excited states, we will use MaGe, the GEANT4-based simulation package developed by both the Majorana and GERDA collaborations. To test the simulation, we have mimicked $\beta\beta$ decays to excited states using an unenriched, segmented, four-crystal Clover[5] detector located at Los Alamos National Laboratory. The MaGe simulation will be validated against the Clover experimental results, and then applied to the other experimental configurations.

The ^{76}Ge $\beta\beta$ decay to the first 0+ excited state of ^{76}Se has a specific signature. It is a triple coincidence comprised of a single-site $\beta\beta$ energy deposition with an energy endpoint of 917 keV, followed by two cascade gammas at 563 keV and 559 keV. A mimicked signal needs to have a similar triple coincidence: a single-site β and two cascade gammas. Because of the beta energy deposition, any mimicked signal must come from within the germanium detector itself, as the beta particles from an external decay will not be able to penetrate the aluminum cryostat around the Clover crystals. This requirement for internal activity limits the available parent radioisotopes to those that are formed in natural germanium from either cosmogenic or neutron activation.

^{77}Ge is an available radioisotope that provides a decay with the required particle coincidences, and is created via neutron activation. We used a 30 mCi AmBe neutron source with four inches of polyethylene to thermalize the neutrons.

The Clover detector utilizes indium patches for electrical connections. Natural indium contains 96% ^{115}In, which has a thermal neutron capture cross-section of 283 barns. Neutron

*P-23, MS H-803, Los Alamos National Laboratory, Los Alamos, NM 87545.

[1] http://majorana.pnl.gov

[2] S. R. Elliott and J. Engel, J. Phys. G: Nucl. Part. Phys. **30**, R183 (2004).

[3] K. Kazkaz *et al.*, IEEE Trans. Nucl. Sci. **51**, 1029 (2004).

[4] A. Carpenter *et al.*, The SEGA Detector, TUNL Progress Report XLII, 77 (2003).

[5] Manufactured by Canberra Eurysis, 800 Research Parkway, Meriden, CT 06450.

activation therefore creates an ^{116}In signal with a high rate compared to ^{77}Ge. Unfortunately, ^{116}In includes a gamma decay at 417 keV, and is therefore a background in the ^{77}Ge signal. This background can be reduced, however, by taking advantage of the triple coincidence of the desired signal. Requiring hits in three of the four crystals reduces the ^{116}In contribution to the signal peak. The reduced accidental rate is measured in a noncoincidence region at 225 keV. The final count is 73.3 events under the 215 keV and 416 keV coincidence, 26.2 of which are expected to be ^{116}In accidentals or other coincidences. Fig. 2.18-1 shows the spectra of events in the 416 keV region coincident with either 215 keV or 225 keV events.

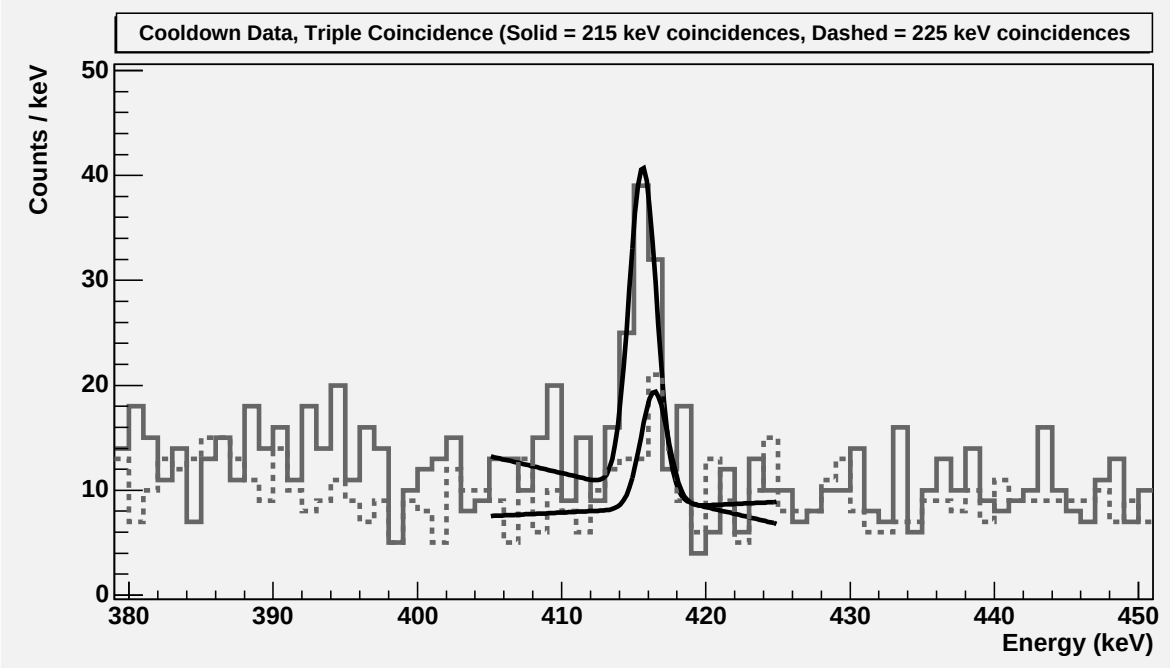

Figure 2.18-1. Spectra coincident with 215 keV events (solid curve) and 225 keV events (dashed curve). Utilizing a measured FWHM at 416 keV of 2.22 keV, a Gaussian fit on the solid curve has an integrated area of 73.3 counts, and the Gaussian fit on the dashed curve has an integrated area of 26.2 counts.

2.19 LArGe — extending the germanium detector technique

C. E. Aalseth,* J. F. Amsbaugh, P. J. Doe, T. Hossbach,* J. L. Orrell,*
R. G. H. Robertson and J. F. Wilkerson

For the last 30 years, large germanium diodes have been an indispensable tool for precision studies of gamma rays. To operate, these detectors must be cooled to liquid nitrogen temperatures. Typically, a detector is housed in a vacuum insulated cryostat and cooled via a copper cold finger. To suppress backgrounds, the detector is frequently surrounded by low background shielding. In 1987, G. Heusser of the MPI, Heidelberg, proposed immersing the crystal in liquid nitrogen (LN_2). This cools the crystal and, since liquid cryogens are inherently clean, the LN_2 also provides shielding against external radiation. This idea has since been adopted by the GENIUS and GERDA collaborations who are searching for evidence of neutrino-less double beta decay in ^{76}Ge. The sensitivity of these germanium diode detectors may be enhanced by surrounding the detector with sodium iodide, which serves as a Compton veto. In 2002, S. Shoenert, also of MPI, Heidelberg, proposed using liquid argon (LAr), rather than LN_2 to cool the crystal. Since LAr is only 10 K warmer than LN2, it is an acceptable alternative. In addition, LAr is a superior shielding material due to its higher density and most importantly, it is a very efficient scintillator, enabling it to act as a Compton veto to identify and suppress backgrounds. The GERDA collaboration is actively investigating this technique with a view to replacing the LN_2 of their current proposal. Initial results are very promising and, as a result, the Majorana collaboration has instigated its own program of investigation, in close coordination with the GERDA collaboration. The promising background suppression potential of this technique could prove of great importance in low background counting. This is of interest not only in screening materials for double beta decay and dark matter experiments, but also for national security. To this end, we are joined by our Majorana colleagues from Pacific Northwest National Laboratory (PNNL). The goal of our program is to demonstrate, on an appropriate timescale, the efficacy of this technique to both the Majorana experiment and to low background counting. To this end we must address the following questions:

- What is the most effective way of collecting the scintillation light from the LAr?
- Can naked germanium diode detectors be operated for extended period (years) in LAr without loss of performance?
- Can the front-end electronic components operate effectively in LAr?

To study the production of scintillation light in association with the operation of a naked Ge detector, we constructed an apparatus containing a P-type Ge detector surrounded by ≈ 0.5 radiation length (7 cm) of LAr. A 20 cm hemispherical PMT with its photocathode immersed in the LAr was used to detect the scintillation light. Preliminary data obtained from the Ge crystal when irradiated with a ^{207}Bi source is shown in Fig. 2.19-1. The upper spectrum is with no veto applied while the lower spectrum shows the effect vetoing signals

*Pacific Northwest National Laboratory, Richland, WA 98352.

from the crystal which are in coincidence with scintillation light from the liquid argon. The factor of 2 suppression of the Compton continuum is expected to improve with more LAr surrounding the crystal.

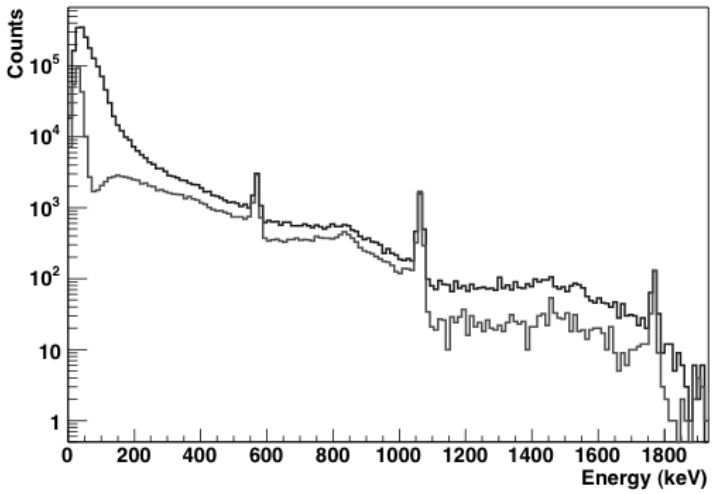

Figure 2.19-1. ^{207}Bi spectra obtained from a naked Ge crystal immersed in LAr with and without the veto.

Using this apparatus we will continue to study ways of optimizing the collection of the scintillation light. A separate apparatus has been designed to investigate both the long term stability of Ge crystals immersed in LAr and the low background counting capabilities.

Underground Science

2.20 A Deep Underground Science and Engineering Laboratory - DUSEL Cascades

W. C. Haxton* and J. F. Wilkerson

For the past four years our group has worked with other physicists, earth scientists, engineers, and educators to formulate science arguments and identify sites for a deep, multipurpose U.S. underground laboratory. As part of the effort to establish a Deep Underground Science and Engineering Laboratory (DUSEL) we have now developed and submitted to NSF a proposal for DUSEL-Cascades, a laboratory that would be located near Leavenworth, WA. Our proposal was a response to the NSF call for conceptual site specific designs for the DUSEL.

At DUSEL-Cascades, we propose to develop a horizontal access facility in the Mt. Stuart batholith, a 20 km by 30 km granite mass on the eastern slopes of the Cascades, famous for its record-setting tunnels. The site properties include: 1) a tunnel path that can be fully cored; 2) a location in an area of low to moderate seismicity, well separated ($\sim$76 km) from the nearest identified active crustal fault; 3) a tunnel alignment that appears to be free of intersections with the older host rock; and 4) an outstanding data base on rock properties and tunnel aging due to seven previous tunnel excavations in the batholith, including the 12.5-km, 1000-m deep Great Cascade Tunnel. The parallel Pioneer Tunnel is largely unlined, providing access to over eight kilometers of deep rock. The portal site is on United States Forest Service ('USFS') land, designated as suitable for such development. There are no mining, environmental contamination, or legacy issues and no requirements for indemnifying previous owners. The permitting process through Chelan County and state and federal agencies is clearly established. Initial steps in this process are already underway.

The envisioned laboratory consists of three components:

- A deep underground horizontal-access site consisting of a portal, two parallel 4.9 km tunnels, a 0.9 km ring tunnel encircling the laboratory area, and laboratory rooms located on USFS land in Chelan County, WA.
- A Science Campus located outside the forest, on a nearby site that is available, properly zoned, and served by utilities.
- A Visitor Center focused on public outreach, K-12 teacher and student development, and undergraduate and graduate education.

In addition, we have defined a second horizontal-access site of intermediate depth, convenient to the Science Campus and already developed, ideally suited for a future neutrino superbeam/nucleon decay detector, should the U.S. elect to pursue such a project in the next decade.

*Department of Physics, University of Washington, Seattle, WA 98195.

We received substantial support from the University of Washington to develop this proposal. As part of the process, we solicited and received significant local community input. Support from the county, local cities, and the state of Washington is strong to proceed with the conceptual study. The proposal and considerably more information on the DUSEL- Cascades can be found at our web page: // http://www.int.washington.edu/DUSEL/cascades.html

2.21 The Lower Monumental Dam Test Counting Facility

C. E. Aalseth,* J. A. Detwiler, J. A. Formaggio, T. Hossbach,* S. McGee, H. S. Miley,* J. L. Orrell* and J. F. Wilkerson

As part of the joint collaboration between the University of Washington and Pacific Northwest National Laboratory (PNNL), we are pursuing the design and construction of a novel low background counting facility, the Advanced Sample Detector (ASD). ASD will build on the knowledge gained from both the 17A low-background counting facility at PNNL, currently one of the most sensitive low-level gamma detectors built above ground, and the Multiple Element Germanium Array (MEGA) that is currently being constructed by PNNL and the Majorana Collaboration at the Waste Isolation Pilot Plant (WIPP) underground facility in New Mexico. The ASD counting system is envisioned to consist of two sets of three high purity germanium detectors that will measure the radioactivity of various samples inserted within the active volume. Surrounding the crystals will be a passive lead shield to attenuate natural radioactivity occurring within the experimental hall. Finally, a 4-π active anti coincidence shield will provide additional background reduction and increased sensitivity to radioactivity.

At least initially, ASD will be situated within Lower Monumental Dam (LoMo), located on the Snake River within an hour's drive from PNNL. The site, which has been used previously by PNNL as a facility for low background counting, provides approximately 75 meters water equivalent of overburden against cosmic rays.

In addition to providing a low-level counting facility for materials and components associated with the Majorana experiment, ASD will also furnish important research and development with regards to the Majorana experiment. ASD will provide a test bed for various mounting techniques of germanium crystals and test cryostat designs that can eventually be employed for the Majorana detector. Finally, the passive and active veto shield used in ASD can serve as a guide for shielding considerations for the main Majorana experiment.

CENPA is contributing a detailed simulation of ASD and the LoMo experimental facility. The simulation uses the framework of the Geant4-based MaGe Monte Carlo software toolkit used by the Majorana and Gerda collaborations. Following detailed simulations, CENPA will actively participate with PNNL personnel in the design and assembly of the new low level counting facility. The facility is projected to be operational with one or more germanium crystals sometime in 2006.

*Pacific Nothwest National Laboratory, Richland, WA 98352.

3 Nuclear Astrophysics

3.1 Extrapolation of the ^{7}Be(p,γ)^{8}B S-factor to low energies, and refined interpretation of ^{8}B Coulomb dissociation experiments

G. F. Bertsch,* H. Esbensen,† A. R. Junghans‡ and K. A. Snover

Recently $S_{17}(0)$ values and $S_{17}(E)$ slopes determined from published Coulomb dissociation (CD) experiments were compared to values obtained from direct ^{7}Be(p,γ)^{8}B measurements and found to differ systematically - on average the CD $S_{17}(0)$ values are lower and the slopes are steeper than direct results.[1] We (H.E., G.F.B. and K.A.S.) have addressed these differences in a recent publication[2] in which we estimate the effects of several refinements in CD theory on the inferred values of $S_{17}(E)$. The refinements - dynamic ^{8}B polarizability and avoiding the far-field approximation - were not included in previous CD experimental analyses. We showed that including these effects tends to raise the low-energy CD $S_{17}(E)$ values, reducing the (apparent) systematic differences between the 2 types of experiments.

Two of us (K.A.S. and A.R.J.) have made some further investigations[3] into the extrapolation uncertainty in $S_{17}(0)$, estimated previously[1] as $\pm$ 6 eV b from the rms deviation of 12 different theories fitted to the low energy data of ref. 1. Our philosophy here is to empirically constrain ^{7}Be(p,γ)^{8}B theories as much as possible using ^{7}Be(p,γ)^{8}B data. We obtained separate s- and d-wave cross sections for 5 of the 12 theories, and we introduced, in addition to the overall normalization, an additional s/d scaling parameter k, where k=1 corresponds to the theoretical s/d ratio. We determined k for each theory from a fit to the data of ref. 1 below 1200 keV,and then we determined the normalization by fitting the data below 425 keV with k fixed to the value determined from the wide-energy-range fit. For the Descouvemont and Baye (DB) cluster-model theory, used in ref. 1 to determine the central value for $S_{17}(0)$, the new fit differs by $< 1\%$. For all 5 theories, these fits yield a mean and rms deviation of $S_{17}(0) = 22.5 \pm 0.4$ eV b. The smallness of this uncertainty and the similarity of the mean value to the DB fit result $S_{17}(0) = 22.1 \pm 0.6$ eV b given in ref. 1, add confidence in the published result. In addition we investigated the sensitivity of the DB theory fit to variations in the channel spin S=1/S=2 ratio, and found that changing this ratio by a factor of 3 from the value given by DB changes $S_{17}(0)$ by $< 1\%$. Finally Descouvemont[4] has made a new, improved cluster-model ^{7}Be(p,γ)^{8}B calculation that includes dynamic ^{8}B polarizability and yields a theoretical value for $S_{17}(0)$ that is much closer to the experimental value. This new calculation is very similar to the DB calculation at low energies and hence will not change our $S_{17}(0)$ significantly. All of these results add significantly to our confidence in the extrapolation procedure (central value and uncertainty) used in ref. 1.

*Institute for Nuclear Theory, University of Washington, Seattle WA 98195.
†Argonne National Laboratory, 9700 Cass Avenue, Argonne IL 60439.
‡Forschungszentrum Rossendorf, Dresden, Germany.

[1] A. R. Junghans *et al.*, Phys. Rev. C **68**, 065803 (2003).
[2] H. Esbensen, G. F. Bertsch and K. A. Snover, Phys. Rev. Lett. **94**, 042502 (2005).
[3] K. A. Snover *et al.*, Proc. of the Eighth Nuclei in the Cosmos Conference, Vancouver Canada, July 2004, to be published.
[4] P. Descouvemont, Phys. Rev. C, to be published.

3.2 Progress in ^{3}He$(\alpha,\gamma)^7$Be

R. W. Abel,* C. Bordeanu, R. M. Donovan,† J. D. Lowrey,‡ K. P. Michnicki, K. A. Snover and D. W. Storm

The S-factor for ^{3}He+^{4}He fusion, $S_{34}(0)$, is at present the largest nuclear physics uncertainty in solar model calculations of the neutrino flux from the sun. We have begun an experiment to measure S_{34} both by detecting the direct capture γ-rays and by measuring the ^{7}Be radioactivity. During the last year we built a gas cell (see section 1), did a variety of background studies, and made some preliminary measurements of the ^{3}He+^{4}He reaction using an Ortec Ge detector with 50% efficiency.

In measurements at $E_\alpha = 3.5$ MeV we observed a significant beam-induced γ-ray background that increased by about 20% over a 24 hour running period. Measurements with and without foil windows and gas, and measurements in which the gas cell beam stops were changed indicated that carbon was building up on the foil, on the beam stop when the cell was open to vacuum, and perhaps on the collimators. Measurements with the foil and gas in place suggest carbon buildup on the beam stop, consistent with discoloration on the beam stop where the beam hit. Excitation functions measured on the beam stops in the range E_α= 2.9 - 3.5 MeV exhibited the known resonance structure of the ^{13}C(α, n) reaction. Further measurements using Energy Dispersive Spectroscopy[1] (EDS) showed carbon on both the beam stops and the foil, with increasing amounts found after irradiation with the beam. Chemical and ultrasound cleaning of the beam stops followed by glow discharge cleaning reduced the amount of carbon initially on the beam stop. In order to reduce the amount of volatiles present in the vacuum, we dissassembled the beam line and target chamber and cleaned them with detergent and solvents, and we installed oil-free roughing pumps in addition to the high-vacuum cryopumps.

We made preliminary ^{3}He$(\alpha,\gamma)^7$Be measurements at $E_\alpha = 3.5$ MeV using a 1μm Ni entrance foil and 200 torr of ^{3}He. We monitored the direct capture γ_0 and γ_1 peaks, and the 429-keV γ-ray from decay of the ^{7}Be first excited state. The γ_0 lineshape, which is dominated by energy loss of the beam in the gas cell, was obtained by subtracting room background and beam-induced background measured with the gas cell filled with ^{4}He. Reasonable agreement was obtained between the measured lineshape and a lineshape estimated by including the known energy dependence of the cross section, the mean Doppler shift of the γ-rays, and using TRIM to estimate the energy loss of the beam in the foil and the gas. The Ge detector efficiency was estimated using calibrated ^{137}Cs and ^{60}Co sources located at the center of the cell, and the Monte Carlo code Pendoses to estimate the efficiency ratio for γ-rays of higher energy, and corrections for finite source size. Our resulting cross section estimate is within 10% of the accepted value. We also measured the number of ^{7}Be atoms produced in combined runs at $E_\alpha = 2.8$ and 3.5 MeV by counting the 478-keV γ-rays from ^{7}Be decay offline in a 4" Pb brick house, and we found rough agreement with the expected value.

*Olympic College, 1600 Chester Ave. Bremerton, WA 98337.
†Department of Physics, University of Washington, Seattle, WA 98195
‡Department of Physics, University of Texas, Austin, TX 78712.

[1] A process in which the sample is irradiated with electrons and the resulting x-ray energy spectrum is obtained.

3.3 Gas cell design for ^{3}He(α,γ)^{7}Be

M. Bacrania, C. Bordeanu, G. C. Harper, K. A. Snover and D. W. Storm

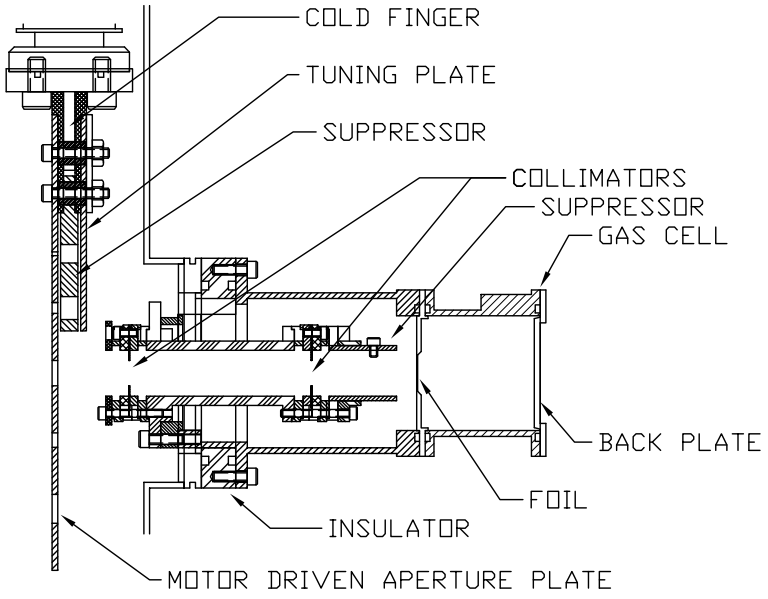

Figure 3.3-1. Gas cell and collimator apparatus for the ^{3}He+^{4}He experiment.

The ^{3}He+^{4}He fusion experiment described in Sec. 3.2 is being performed on the L45 beamline used previously for the ^{7}Be(p,γ)^{8}B experiment. The accelerator beam passes through two magnetic quadrupoles, two steering magnets, a rastering magnet and into a target box on the downstream side of which is mounted the gas cell and collimator apparatus shown in Fig. 3.3-1. The ^{4}He$^+$ beam enters horizontally from the left, passing through the aperture plate. Initially the beam is tuned through a 1 mm diameter aperture near the top of the plate, and the transmitted beam is collected on the electron-suppressed tuning plate. Then the beam rastering is turned on and the plate is positioned to allow the beam to pass through a 7 mm clearance aperture. The rastered beam then passes through 2 copper collimators and a copper electron suppressor and enters the 3 cm long gas cell through a thin nickel entrance foil. The beam stops in a 10 mil OFHC copper stopper soldered onto a copper backplate. The backplate is air cooled, and the whole gas cell assembly is electrically isolated and used as a Faraday cup. The two collimators and the electron suppressor are assembled using anodized aluminum insulating spacers. A cold trap will be used to shield the upstream side of the aperture plate to suppress carbon deposition. The cylindrical gas cell wall is thin aluminum, covered on the inside by a thin tantalum liner. The removable foil holder is made of nickel, with a 10 mm diameter aperture. A second movable aperture plate mounted on a rotating arm is located upstream of the apparatus shown in Fig. 3.3-1, and may be used also.

3.4 Using ^{24}Mg(α,γ)resonances to determine energy losses in a gas cell

C. Bordeanu, J. D. Lowrey,* K. P. Michnicki, K. A. Snover and D. W. Storm

For the ^{3}He + ^{4}He capture experiment (see Section 3.2) it is essential to know the energy of the ^{4}He beam throughout the gas in the gas cell. We have measured the energy loss of the beam in the 1-μm nickel window and the 3-cm long gas volume using the resonance in ^{24}Mg(α,γ) at E$_\alpha$ = 3.199. By making this measurement at various gas pressures we can separate the energy losses in the window and in the gas. (Measurements with no gas are not feasible, since the gas must cool the nickel window.)

We evaporated 70 μg/cm^2 of natural Mg on the beam stop of the gas cell. A 5 x 6 inch NaI crystal detected the 12.7- and 11.0-MeV gamma rays from the resonance decay to the ^{28}Si ground and first excited states. Fitting the excitation functions (see Fig. 3.4-1) we obtain the central beam energy at resonance and the energy spread produced by straggling and foil nonuniformity. If energy loss were independent of beam energy, we could use the results of two measurements, one at 100 and one at 200 Torr, to solve directly for the foil energy loss and gas energy loss. Using TRIM[1] to correct for the energy dependence of the energy loss results in less than a 1% adjustment over the present energy range.

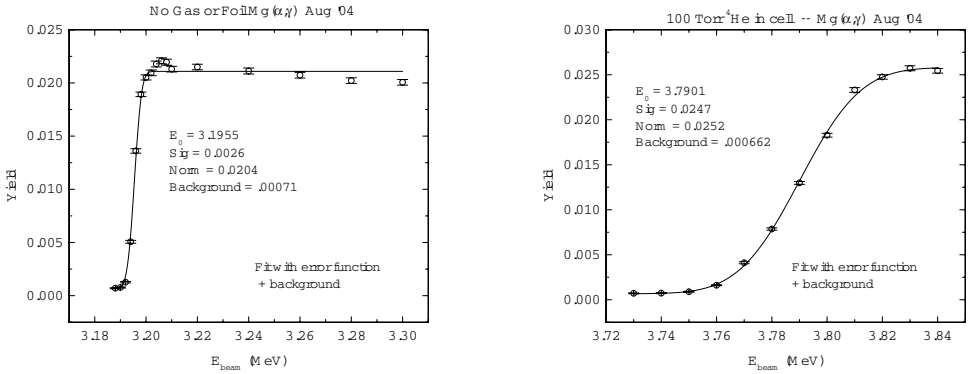

Figure 3.4-1. Excitation functions for ^{24}Mg$(\alpha,\gamma_0)^{28}$Si with an open gas cell and with the nickel window and gas in the cell.

We find that the energy losses for 200-Torr gas pressure are 511 ± 4 keV in the foil and 155 ± 4 in the gas, for an incident beam energy of 3861 keV. The primary source of uncertainty is the uncertainty in the gas pressure, which we expect to improve. Accurate gas pressure is required to separate the total energy loss, measured with better than 2 keV uncertainty, into the loss in the gas and that in the foil. Furthermore, the measured energy spread is consistent with straggling in the foil and gas, as predicted by SRIM,[1] with an additional 2% foil nonuniformity. Finally, we studied energy loss as a function of beam intensity to determine heating of the gas. We find a 4% change in gas density between beam currents of 0.20 and 0.60 μA. This heating effect needs further study to determine its dependence on beam current.

*Department of Physics, University of Texas, Austin, TX 78712.

[1] J. F. Ziegler and J. P. Biersack, www.SRIM.org.

3.5 Status of the search for the ^{8}B(2^+) $\rightarrow$ ^{8}Be(0^+) beta decay transition

M. K. Bacrania, W. C. Haxton,* R. G. H. Robertson and D. W. Storm

In 2004, we reanalysed our most recent set of ^{8}B decay data[1] using improved cuts on coincidence timing and scintillator energy information. The resulting upper limit for the branching ratio of ^{8}B second-forbidden beta decay is 5.6×10^{-5}. This is well below the 10^{-3} branching ratio that would affect the analysis of precision measurements of ^{8}B and *hep* solar neutrinos.

Theoretical estimates[2,3] have indicated that the ^{8}B second-forbidden branching ratio should be on the order of $10^{-6} - 10^{-9}$. Unfortunately, these estimates do not give much information about the details of the calculations, and Ortiz[3] only considers the vector contribution. In light of this, we are working to calculate the transition rate of the second-forbidden decay using the formalism developed by Walecka[4] and Donnelly and Haxton.[5] This involves approximating the initial ^{8}B and ^{8}Be states with Cohen-Kurath p-shell wave functions,[6] and using a multipole representation of the beta-decay nuclear matrix elements to calculate the transition rate of both the allowed and second-forbidden decay transitions.

We are currently trying to improve our understanding of the response of silicon detectors to low-energy alpha particles (see Section 3.6). We are also developing a technique for low-energy alpha particle calibration using the delayed-alpha breakup of excited ^{12}C, which will be produced in our silicon detector by the decay of implanted ^{12}N. This calibration, combined with our understanding of pulse-height defect for low-energy alpha particles in silicon, will help in the development of a robust signal-extraction technique to identify low-energy delayed-alpha particles arising from ^{8}B second-forbidden decay.

*Department of Physics, University of Washington, Seattle, WA 98195.

[1] CENPA Annual Report, University of Washington (2003) p. 37.

[2] R. E. Tribble and G. T. Garvey, Phys. Rev. C **12**, 967 (1975)

[3] C. E. Ortiz, Ph. D Dissertation, (2000), Department of Physics, University of Notre Dame, Notre Dame, IN 46556.

[4] J. D. Walecka, in Muon Physics, eds. V. W. Hughes and C. S. Wu, Academic Press, New York, NY, **2**, 113 (1975).

[5] T. W. Donnelly and W. C. Haxton, Atomic Data and Nuclear Tables, **23**, 103 (1979).

[6] S. Cohen and D. Kurath, Nucl. Phys. **73**, 1 (1965).

3.6 Silicon detector response to low-energy alpha particles

M. K. Bacrania, G. C. Harper and D. W. Storm

As described in previous annual reports,[1] we are working to place a limit on the branching ratio of the $^8\mathrm{B}(2^+) \rightarrow {}^8\mathrm{Be}(0^+, \mathrm{g.s.})$ second-forbidden beta decay transition by observing the decay of ^{8}B implanted into a silicon PIN photodiode detector. The signature for this transition is the decay of the ground state of ^{8}Be, which results in two 46-keV alpha particles (excluding nuclear recoil corrections).

At low energies, energy lost by the alpha particle to undetectable nonionizing interactions accounts for a significant fraction of the energy loss. For example, in a TRIM simulation of 45 keV-alpha particles in silicon, the amount of energy lost to ionization is estimated to be only $\sim 90\%$ of the total energy loss. In order to fit our measured energy spectrum for the $^8\mathrm{B}(2^+) \rightarrow {}^8\mathrm{Be}(0^+, \mathrm{g.s.})$ decay signature, we must understand the response of our Si detector to low-energy alpha particles. To do this, we produce 80-200 keV alpha particles with the Terminal Ion Source of the University of Washington Tandem Van de Graaff accelerator. The beam is then scattered by a $\sim 0.6\,\mu\mathrm{g/cm}^2$ gold layer evaporated on a $50\,\mu\mathrm{g/cm}^2$ carbon foil. The silicon detector (Hamamatsu S3204-06) is placed on a rotating stage located at 100 degrees relative to the beam axis. The detector is calibrated with a ^{133}Ba gamma-ray source, with lines at 81, 302, and 356 keV. At each beam energy, the detector can be rotated ± 45 degrees about an axis perpendicular to the scattering axis. The energy thickness of the detector dead layer can be determined from the shift in peak position as a function of detector rotation angle. By subtracting the dead layer energy thickness from the incident alpha-particle energy, we can determine the energy of the alpha particle entering the active region of the detector.

This result is then compared to the difference between the incident and detected alpha-particle energies (with the detector perpendicular to the scattering axis). The difference between this value and the dead-layer thickness is taken to be the measured pulse-height defect (see Fig. 3.6-1). Combining the pulse-height defect with a parametrization of the measured peak shape as a function of incident energy will allow us to predict the expected detector response to an alpha particle with a specified incident energy.

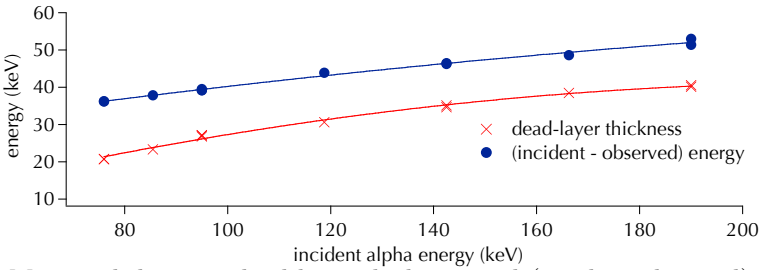

Figure 3.6-1. Measured detector dead-layer thickness and (incident-observed) energy. The difference between the two curves is the pulse-height defect.

[1] CENPA Annual Report, University of Washington (2003) p. 37.

4 Nuclear Structure

4.1 Measurement of ^{40}Ar(p,n) and comparison to ^{40}Ti β decay

M. Bhattacharya,* A. García and C. D. Goodman†

We have determined the Gamow-Teller strength distribution for ^{40}Ar$\rightarrow^{40}$K using the 0° (p,n) reaction. The interest in this particular nucleus comes from its use as a neutrino detector. The Icarus detector now under construction at Gran Sasso will consist of a large-mass (initially 3000 Tons) liquid Ar Time-Projection-Chamber. Icarus is designed principally to look at proton decay and neutrinos from accelerators, but it will also be sensitive to neutrinos with energies above ~ 5 MeV. Although the solar-neutrino oscillation parameters have been determined already from other experiments, there is still strong motivation to understand the efficiency of Icarus for neutrinos with energies between ~ 5 and ~ 50 MeV: Icarus would be sensitive to supernovae neutrinos (SRN).[2] The detection of neutrinos from a supernova explosion in our galaxy would help understand the core collapse mechanism and detecting supernova relic neutrinos (from all supernova that have exploded so far in the Universe) would produce an independent determination of the rate of supernovae explosions.

The efficiency for the process that dominates the detection of neutrinos with energies between ~ 5 and ~ 50 MeV, $\nu_e + ^{40}\mathrm{Ar} \rightarrow e^- + ^{40}\mathrm{K}$, depends on the distribution of weak strength (Fermi and Gamow-Teller) with excitation energy. The Fermi strength is mostly concentrated on a single transition to the Isobaric Analog State (IAS) which is well determined. The distribution of Gamow-Teller strength, $B(\mathrm{GT})$, has been calculated[3] and determined indirectly from the decay of ^{40}Ti.[4] Assuming isospin symmetry and further that no differences are brought by the fact that the daughters of the decay of ^{40}Ti are unbound to proton emission while their analog states in ^{40}K are bound, the distribution of $B(\mathrm{GT})$ from ^{40}Ti should be identical to that from ^{40}Ar.

An additional motivation for our work is the determination of the extent to which charge-exchange reactions can be used to extract Gamow-Teller strength. Knowledge of the latter is important for nucleosynthesis calculations. There is no equivalent tool for measuring GT strength distributions that can be applied over a wide range of nuclei and excitation energies, so it is important to push the accuracy of these measurements as far as possible, to attempt to understand the nature of the uncertainties, and to try to minimize them.

Although we find rough agreement in the integrated strength with respect to the beta-decay measurment we find a strong discrepancy in the ratio between the strengths corresponding to two strongly fed low-excitation lines: $B(\mathrm{GT}, E_x = 2.8\ \mathrm{MeV})/B(\mathrm{GT}, E_x = 2.3\ \mathrm{MeV}) = 0.89 \pm 0.14$ from this work, but $B(\mathrm{GT}, E_x = 2.8\ \mathrm{MeV})/B(\mathrm{GT}, E_x = 2.3\ \mathrm{MeV}) = 1.67 \pm 0.1$ from the beta-decay work. This discrepancy is puzzling and we are investigating its possible origin in collaboration with G. Bertsch.[5]

*Mail Code XD42, Marshall Space Flight Center, Huntsville, AL 35812.
†IUCF, Indiana University, Bloomington, IN 47405.

[2] A. G. Cocco *et al.*, LANL archive:http://xxx.lanl.gov/abs/hep-ph/0408031
[3] W. E. Ormand *et al.*, Phys. Lett. B **345**, 343 (1995).
[4] M. Bhattacharya *et al.*, Phys. Rev. C **58**, 3677 (1998).
[5] Department of Physics, University of Washington, Seattle, WA 98195.

4.2 Mass determination of the lowest $T = 2$ state in ^{32}S using the ^{31}P(p, γ) reaction

E. G. Adelberger, A. García, S. A. Hoedl, S. K. L. Sjue, A. L. Sallaska and S. Triambak

We are presently in the final stages of analysis of the data from ^{31}P(p, γ) to test the Isobaric Multiplet Mass Equation (IMME) for the $A = 32$ multiplet. This involves determination of the excitation energy of the lowest $T = 2$ state in ^{32}S with high precision and accuracy by determining the energies of the decaying gammas from the state of interest.[1] The most important sources of systematic effects in our γ ray energy determination were gain-drifts, Doppler-shifts in the energy calibrations and the misalignment of the Ge detectors at $\pm 90^\circ$. We corrected for gain shifts using a gain correction program that corrected for the shifts periodically after a given time interval with respect to a fixed reference. We performed Monte Carlo simulations[2] of the calibration reactions to calculate the average Doppler shift on the calibration gammas from ^{35}Cl(n, γ) and ^{27}Al(p, γ). One fundamental difference between the ^{35}Cl(n, γ) calibration and the ^{31}P(p, γ) and ^{27}Al(p, γ) reactions was that in the latter, the source of the γ rays was from a target at the center of the target chamber, whereas the ^{36}Cl γ source was a bulk of NaCl outside the chamber, offset by a distance ≈ 12 cm from the center of the chamber. Since gamma ray peak centroids are known to depend on the position of the source with respect to the detector and the γ ray energy,[3] it was important that we test this effect on our ^{35}Cl(n, γ) calibration that produces γ rays with energies upto 8578 keV. To test the effect of peak centroid dependence on source position we fixed a 3.5 μCi ^{56}Co source at $\approx$ 5.0 cm to the detector endcap and took data from ^{35}Cl(n, γ) with the ^{36}Cl gammas incident on the detector at three different angles. We then determined the energy of the 7790 keV γ peak from ^{36}Cl using both the calibration sources. The determined energies were found to agree within 0.2 keV for all three detector orientations.

On taking the weighted mean of the determined γ energies from ^{31}P(p, γ) in both the detectors and correcting for nuclear recoil, we obtain the excitation energy of the lowest $T = 2$ state in ^{32}S to be $E_x = 12048.06 \pm 0.36$ keV. In spite of this being ≈ 3 keV higher than the previously determined value,[4] our results yield good fit to the IMME and solves a discrepancy that previously existed between the IMME-predicted Q_{EC} value for the β^+ decay of ^{32}Ar and the directly determined Q_{EC} value from a recently determined mass[5] of ^{32}Ar. In our measurement, we were limited by the uncertainties in the alignment of our Ge detectors. Our preliminary Monte Carlo results imply that the 8124 keV gamma ray from ^{32}S is Doppler shifted by ≈ 0.35 keV if the detector is mis-aligned by 1° from 90°. We plan to take additional data with the Ge detectors at 0° to the beam, where the Doppler shift is maximum but there is least sensitivity to detector mis-alignment. This will be an additional check on our determined gamma energies and help improve the precision of our measurement.

[1] CENPA Annual Report, University of Washington (2003) p. 39; (2004) p. 39.

[2] CENPA Annual Report, University of Washington (2004) p. 38.

[3] R. G. Helmer, R. J. Gehrke and R. C. Greenwood, Nucl. Instrum. Methods **123**, 51 (1975).

[4] M. S. Antony *et al.* in *Proceedings of the International Conference on Nuclear Physics*, Lawrence Berkeley Laboratory, Berkeley, CA, 1980, Vol. 1.

[5] K. Blaum *et al.*, Phys. Rev. Lett. **91**, 260801 (2003).

4.3 Resonance energies in ^{32}S(p,γ) and calibration of ^{33}Ar beta-delayed spectrum

E. G. Adelberger, O. D. Biesel, A. García, H. E. Swanson and S. Triambak

The energy calibration of the beta-delayed proton spectrum from ^{33}Ar is limited by the precision with which the energies of states in ^{33}Cl have been determined. The calibration of the ^{33}Ar lines plays an important role in determinations[1] of the e,ν correlation from ^{32}Ar.

Consequently we took measurements of ^{32}S(p,γ) concentrating on resonances that are observed in the beta decay of ^{33}Ar. The experiments were performed using the Tandem van de Graaff, using a proton ion source located at the terminal, which allowed for very stable beam currents of up to ≈ 20 μA on target.

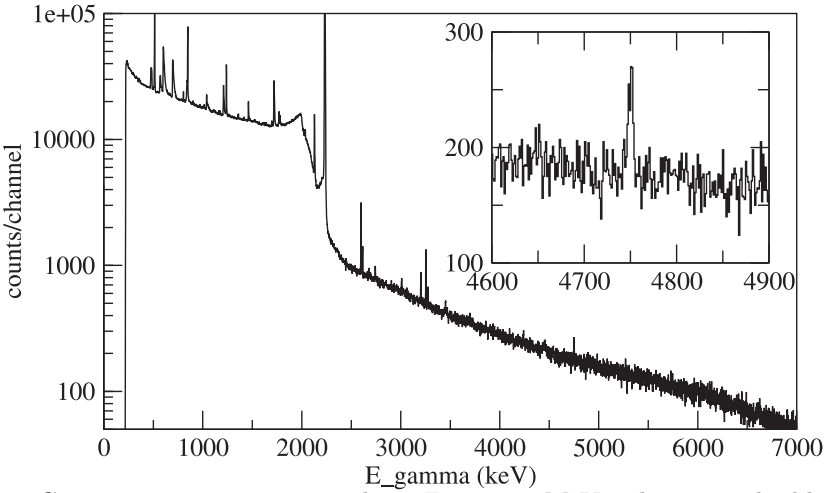

Figure 4.3-1. Gamma spectrum measured at $E_p \approx 3.4$ MeV. The insert highlights the gamma corresponding to the decay of the lowest $T = 3/2$ state to the first excited state in ^{33}Cl.

We are presently analyzing the data: we find rough agreement with previous experiments but get improved precision in the determination of resonance energies. As an example we show the γ-ray spectrum taken at $E_p \approx 3.4$ MeV where we observe the population of the lowest $T = 3/2$ state in ^{33}Cl which subsequently decays to the first excited state. The decay is weak because the $T = 3/2$ state is unbound to proton emission. The fact that gamma decays from the $T = 3/2$ state in ^{33}Cl mainly feed the first excited state is in agreement with the expectation based on isospin symmetry and observation of the analog decays in the mirror nucleus ^{33}P.

[1] E. G. Adelberger *et al.*, Phys. Rev. Lett. **83**, 1299 (1999); M. C. Pyle *et al.*, Phys. Rev. Lett. **88**, 122501 (2002).

4.4 Response function of Si detectors for α particles

H. Bichsel, J. Couture* and A. García

In order to extract the neutrino spectrum from ^{8}B and the beta-neutrino correlation in the decay of ^{8}Li and ^{8}B from the measured energy of the alpha particles (see Section 1.1) following the decays of ^{8}Li and ^{8}B, we need to understand the response of our α counters in the range 1MeV $\leq E_\alpha \leq$ 9MeV. We have made calibration determinations at $E_\alpha \approx 3.2$ and 5.5 MeV, but calculations are essential to interpolate between them.

At this time last year we had produced a Monte-Carlo calculation that used straggling functions. These had to be prepared for specific target thicknesses. So, a calculation of the ionization energy in a detector where particles get stopped was done by first calculating a series of tables of straggling functions for different thicknesses and then using these tables for different thicknesses. The process was involved because the straggling functions needed to be interpolated from one thickness to the other, and the particles we wanted to simulate were moving through varying thicknesses of deadlayers (for example, according to the angle the particles had in coming to the detector).

During the past year we implemented all components of the calculation into a single Monte-Carlo code that uses the single-collision cross section as input and calculates the amount of ionization without any need for going through the intermediate steps of calculating straggling functions and then interpolating. The simulation does not quite reproduce

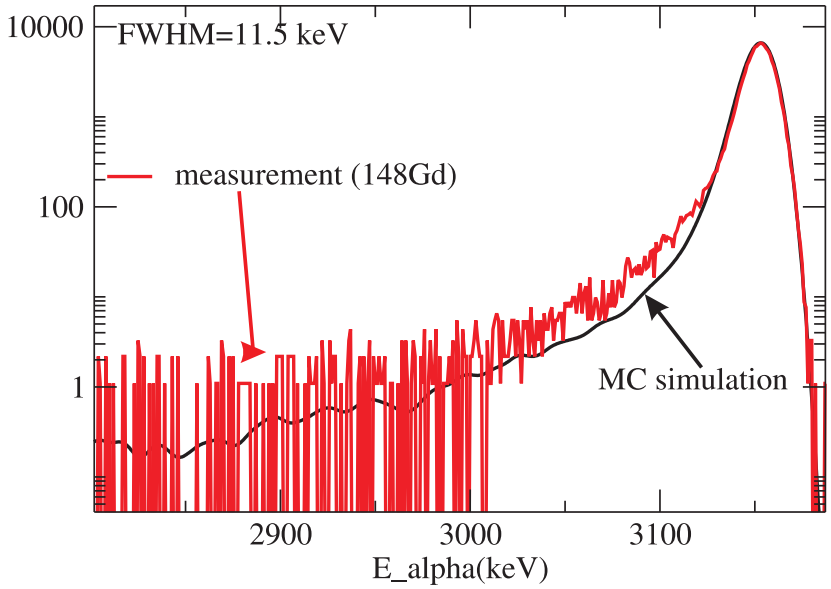

Figure 4.4-1. Measured versus simulated response functions for ^{148}Gd source.

the low energy tail observed with a source, but we suspect these discrepancies are due to inhomogeneities in the source dead layers.

*Department of Physics, Notre Dame University, Notre Dame, IN 46556.

5 Relativistic Heavy Ions

5.1 Summary of event-structure analysis

T. A. Trainor

Previous work has emphasized a phenomenological survey of fluctuation and correlation structure in A-A collisions. We are now emphasizing physical interpretations of those results and connections with previous studies of elementary nuclear collisions in high-energy physics. The analysis of correlations in p-p collisions at RHIC has been very productive for understanding our A-A results, especially the connection between minijet structure in A-A and parton fragment distributions measured in p-p and e-e collisions. With our specialized techniques we are able to study previously inaccessible low-Q^2 partons. Those techniques include autocorrelations applied to angular correlations and transverse rapidity to study transverse momentum correlations. The following is a summary of recent results:

- Hard component in p-p p_t spectra identified with parton fragmentation
- Universal form of single-particle fragmentation functions on transverse rapidity y_t
- Identification of correlations on (y_t, y_t) with two-particle fragmentation functions
- Precision characterization of soft-component (string fragment) correlations
- Generalization of jet morphology (angular correlation) measures to low Q^2
- First low-Q^2 measurement of fragment transverse momentum j_t relative to jet thrust
- First low-Q^2 measurement of parton transverse momentum k_t
- Precision centrality determination of mean participant path length in A-A collisions
- p_t autocorrelations inferred by inversion of $\langle p_t \rangle$ fluctuation scaling in Au-Au collisions
- Deformation of minijet peak in p_t autocorrelation in central Au-Au collisions
- Observation of recoil response of the bulk medium to parton emission in Au-Au collisions
- Energy dependence of minijet production in A-A collisions from 10 to 200 GeV

A broad picture of low-Q^2 parton scattering, dissipation and fragmentation from elementary collisions to central heavy ion collisions is emerging. We are using minimum-bias partons to probe the heavy ion bulk medium just as Brownian motion of probe particles reveals the microscopic structure of ordinary fluids. Our correlation techniques are analogous to those used for cosmic microwave background surveys, and the issues are similar: characterization of temperature/velocity correlation structure reflecting evolution of a complex dynamical system prior to decoupling.

5.2 Soft and hard components of inclusive p_t distributions from RHIC p-p collisions at $\sqrt{s} = 200$ GeV

J. Gans,* R. J. Porter and T. A. Trainor

We have analyzed the shapes of p_t distributions for ten event multiplicity classes from RHIC collisions at $\sqrt{s} = 200$ GeV. The distributions can be decomposed into a soft component S_0 described by a Lévy distribution on transverse mass m_t, $S_0 \equiv A/\{1+\beta(m_t-m_0)/n\}^n$ (or error function on transverse rapidity y_t), and a semi-hard or minijet component H_0 described by a gaussian distribution on y_t and interpreted in terms of minijets as fragments of *minimum-bias* (mainly low-Q^2) partons. Normalized distributions on p_t for the ten multiplicity classes are shown in the first panel of Fig. 5.2-1, with the same soft-component distribution S_0 (solid curve) in each case. When the common S_0 is subtracted from those distributions there results the distributions in the second panel, which are well described by gaussian distributions (solid curves) with shape almost independent of n_{ch}. We have transformed to transverse rapidity $y_t \equiv \ln\{(m_t + p_t)/m_0\}$ as a velocity variable to provide a 'native' description of minijets as hadron fragments from a moving source. The minijet fraction at 200 GeV increases nearly linearly with event multiplicity, and there is evidence for a small but significant third component at smaller y_t which *decreases* with increasing multiplicity.

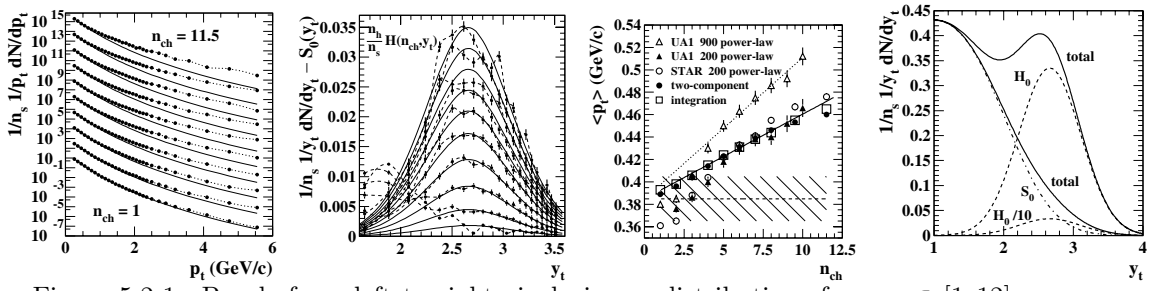

Figure 5.2-1. Panels from left to right: inclusive p_t distributions for $n_{ch} \in [1, 12]$, same on transverse rapidity y_t, soft reference S_0 subtracted to reveal hard components, hard components on logarithmic scale normalized to $n_h = 1$ and compared to hard reference H_0.

The third panel shows trends for ensemble-averaged distribution mean-p_t as a function of event multiplicity. Values based on this two-component model and direct integration of spectra agree and exhibit a linear trend. Values based on a so-called 'power-law' fit to data agree for larger n_{ch} values but disagree significantly at low multiplicity. This behavior was traced to the effect of the low-y_t structure in the second panel on the power-law fit, causing an overestimation of yield in the unobserved region below $p_t = 0.2$ GeV (containing 30% of the yield). The last panel sketches the soft and hard components of the two-component model for minimum-bias events (lower solid curve) and estimates that for events containing at least one semi-hard parton scatter (upper solid curve). The stability of the minijet fragment distribution with event multiplicity indicates that the gaussian distribution on y_t is a valid minimum-bias minijet input for A-A collision models. This previously unobserved hard component and gaussian y_t dependence disagrees with the conventional picture that a 'QCD-inspired power-law' distribution $A/(1 + p_t/p_0)^n$ describes the entire p_t distribution.

*Department of Physics, Yale University, New Haven, CT 06520.

5.3 Transverse rapidity and 1D jet fragmentation functions for e-e and p-p collisions

T. A. Trainor

When a parton (quark or gluon) in a hadron experiences sufficient momentum transfer it fragments into a correlated group of hadrons called a jet. The *fragmentation function* describes the distribution of hadron fragment momenta along the jet axis. Hadron momentum is conventionally normalized by the parton momentum as estimated by E_{jet} (reconstructed jets), $\sqrt{s}/2$ (e^+-e^-) or $Q/2$ (e-p) (*e.g.*, $x = p/E_{jet}$). Alternatively, relative fragment momentum is measured logarithmically by $\xi \equiv \ln(1/x)$. Fragmentation functions for selected jet energies plotted on ξ are shown in the left two panels of Fig. 5.3-1 for p-p and e^+-e^- collisions.

In the first panel, changing the jet angular acceptance (jet cone radius) at fixed E_{jet} causes systematic variation of the low-p_t end of the fragmentation function. In the second panel is shown systematic variation of the fragmentation function with jet energy for e-e collisions. QCD theory (modified leading log approximation or MLLA) is shown as the solid curves, which deviate significantly from data on the low-momentum (right) sides of the peaks.

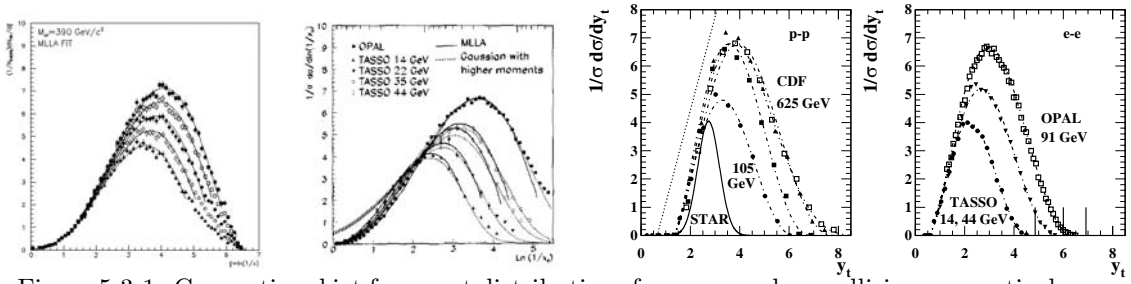

Figure 5.3-1. Conventional jet fragment distributions from p-p and e-e collisions respectively plotted on $\xi \equiv \ln(1/x)$ (left) and replotted on the corresponding rapidity (right).

In connection with our study of two-particle correlations on transverse rapidity (see Sec. 5.4) we have replotted fragmentation functions from several collisions systems on rapidity $y(p; m_0) \equiv \ln\{(\sqrt{p^2 + m_0^2} + p)/m_0\}$, with $y_{max}(X; m_0) \equiv \ln\{(\sqrt{X^2 + m_0^2} + X)/m_0\}$ and $X = E_{jet}$, $\sqrt{s}/2$ or $Q/2$. In that format we find that all fragmentation functions can be described over their entire range by beta distribution $\beta(x; p, q) = x^{p-1}(1-x)^{q-1}/B(p, q)$, with beta function $B(p, q) \equiv \Gamma(p + q)/\Gamma(p)\Gamma(q)$ and parameters $p = 2.85$ and $q = 3.7$. The *standard* beta distribution, conventionally defined on $x \in [0, 1]$, is rescaled to $\beta(y; p, q)$ on $[y_{min}, y_{max}]$, where y_{min} is 0.5 for e-e collisions and 1.5 for p-p collisions, the latter endpoint presumably reflecting the presence of the spectator parton system in the p-p case. The result of a STAR two-component analysis of p-p collisions (see Sec. 5.2) is included in the third panel as the small gaussian (describing *minimum-bias* parton fragments). Systematics in the right two panels imply that the jet multiplicity trend is $\langle n_{ch} \rangle = 1 + A\,(y_{max} - y_{min})^2$ with $A = 0.8$, whereas the MLLA prediction is $\exp\{a \ln(Q/2\Lambda)\}$. We can also represent the most probable point (mode) as $y_{t,peak} = a\,(y_{max} - y_{min}) + y_{min}$, where $a \equiv (p-1)/(p+q-2) = 0.4$. MLLA gives $\xi_p \sim \ln(Q/2\Lambda)$.

5.4 Two-particle correlations on transverse rapidity y_t in p-p collisions at $\sqrt{s} = 200$ GeV

R. J. Porter and T. A. Trainor

Particle pairs from p-p collisions can be separated on azimuth difference variable $\phi_\Delta \equiv \phi_1 - \phi_2$ into *same-side* ($|\phi_\Delta| < \pi/2$) and *away-side* ($|\phi_\Delta| > \pi/2$) pairs. Fig. 5.4-1 shows same-side (left panels) and away-side (right panels) correlations of the form $\Delta\rho/\sqrt{\rho_{ref}}$ (normalized covariance) distributed on transverse rapidity subspace (y_{t1}, y_{t2}). Each pair of panels represents like-sign (LS) and unlike-sign (US) charge combinations respectively. Peak structure can be decomposed into a soft component ($y_t < 2$ for both pair partners) and a hard component ($y_t > 2$ for both partners). Further description of the correlation structure is simplest in terms of sum and difference *diagonals* $y_{t\Sigma} \equiv y_{t1} + y_{t2}$ and $y_{t\Delta} \equiv y_{t1} - y_{t2}$. In the left two panels (same-side) the LS soft component is interpreted as quantum correlations (HBT). The LS hard component is small, and may itself be due to quantum correlations (from parton fragmentation). The US hard component is a peak at $y_t \sim 2.8$ elongated along $y_{t\Sigma}$. The US hard component runs continuously into the US soft component at lower y_t. In the right panels (away side) the hard components in both LS and US panels appear as peaks nearly symmetric about their centers, with rapid falloff below $y_{t\Sigma} \sim 4$ and nearly equal amplitudes. There is a large US soft component from longitudinal string fragmentation due to local charge conservation (producing charge ordering on z).

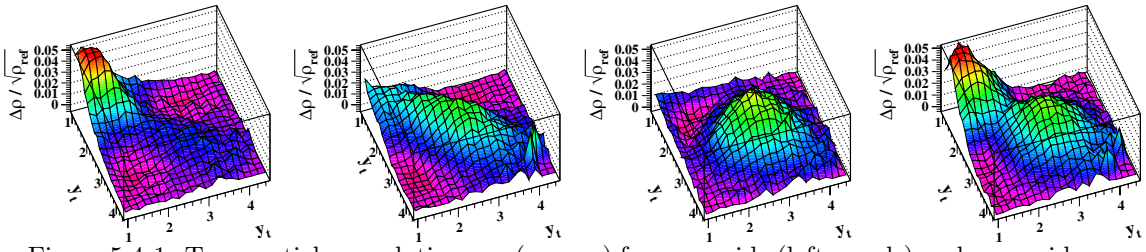

Figure 5.4-1. Two-particle correlations on (y_{t1}, y_{t2}) for same-side (left panels) and away-side (right panel) pairs and for like-sign (LS) and unlike-sign (US) pairs in each case.

The (y_{t1}, y_{t2}) correlations obtained in this study are directly related to our study of correlations on (η, ϕ) with the same p-p data. The soft-component correlations on (η, ϕ) are consistent with previous descriptions in terms of string fragmentation (Lund model). A hard-component angular correlation on (η, ϕ), in the form of a symmetric peak at the origin (jet cone), is consistent with the large transverse velocity of a parton as hadron fragment source. Away-side hard-component correlations properly reflect momentum conservation between scattered partons (dijets). Those hard-component (η, ϕ) systematics, fully consistent with conventional expectations for jet angular correlations, are observed for pairs of particles in this study with *both* particles having p_t as low as 0.5 GeV/c ($y_t \sim 2$), *much lower than observed previously with leading-particle methods, and using no trigger or high-p_t leading particle*. There is essentially no *analysis* bias in the corresponding parton sample.

5.5 2D jet fragmentation functions in p-p collisions at $\sqrt{s} = 200$ GeV

R. J. Porter and T. A. Trainor

Same-side unlike-sign (US) (y_t, y_t) correlations described in the previous article (see Sec. 5.4) can be interpreted in terms of a two-particle fragmentation function. In a related article (see Sec. 5.3) we describe single-particle fragmentation functions plotted on rapidity y (infrared safe), which are analogous to the more conventional form plotted on logarithmic variable $\xi \equiv \ln(Q/2p)$ (not infrared safe), with $Q/2$ the parton momentum. An example from the H1 experiment at HERA is shown in the first panel of Fig. 5.5-1 for two mean values of $Q/2$. In the second panel we sketch a corresponding 2D distribution of fragmentation functions on rapidity *vs* parton momentum in the second panel. The diagonal dotted line represents the parton momentum plotted as a rapidity. The shorter solid diagonal lines parallel to the dotted line represent trends of fragment momenta for increasing fragment multiplicities (integer labels), the longest of those at center representing a pair of fragments each with $\sim 1/2$ the parton momentum. The most-probable ξ value, ξ_p is shown by the upper arrow relating the $Q/2$ locus to the line describing the peaks of the fragmentation functions above $Q/2 \sim 1$.

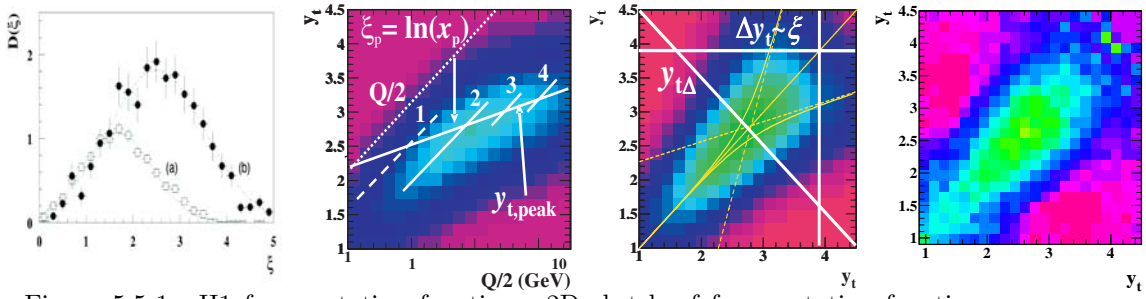

Figure 5.5-1. H1 fragmentation functions, 2D sketch of fragmentation functions, corresponding two-particle distribution, and distribution for same-side US pairs from previous article.

In the third panel we symmetrize the distribution from the second panel because in our (y_t, y_t) analysis instead of correlating fragments with partons we are correlating fragments with fragments in a symmetric way. The yellow loci superposed on that plot indicate the method of constructing the distribution: a gaussian form of constant width relative to the solid curves as centerlines. That illustration can be compared with the fourth plot, which is the data for unlike-sign same-side pairs – the two-particle fragment distribution which corresponds to the symmetrized sketch. The vertical and horizontal white lines in the third panel illustrate the basis for a conventional leading-particle analysis of jet fragmentation: a *conditional* distribution invoking an asymmetric fragment pair – a high-p_t trigger particle and associated particles. The relation of associated to trigger p_t (y_t) is then given by ratio x or logarithmic measure $\xi \sim \Delta y_t$. In the case of low-Q^2 partons, which dominate the minimum-bias parton distribution, the fragment distribution becomes symmetric about the sum diagonal, and the more appropriate variables to measure the distribution are sum and difference rapidities $y_{t\Sigma} \equiv y_{t1} + y_{t2}$ and $y_{t\Delta} \equiv y_{t1} - y_{t2}$.

5.6 Soft components of (η, ϕ) correlations for RHIC data and Pythia Monte Carlo in p-p collisions at $\sqrt{s} = 200$ GeV

R. J. Porter and T. A. Trainor

To isolate the *soft component* of two-particle p-p correlations we define soft pairs as having $y_t < 2$ ($p_t < 0.5$ GeV/c). Fig. 1 shows minimum-bias soft-component correlations (all soft pairs for all multiplicity classes) of the form $\Delta\rho/\sqrt{\rho_{ref}}$ on $(\eta_\Delta, \phi_\Delta)$. Panels in this figure correspond to charge combinations like-sign (LS) and unlike-sign (US), for RHIC data (left panels) and for Pythia simulations (right panels). The first panel is dominated by a 2D gaussian peak at the origin representing quantum correlations (HBT). The US combination in the next panel is dominated by a 1D gaussian peak on η_Δ, arising from local charge conservation during string fragmentation, producing hadron charge ordering along the collision axis. That trend is suppressed near the origin (the depression on azimuth of the η_Δ gaussian) due to local transverse-momentum conservation. The narrow peak at the origin represents electron-positron pairs from photon conversions. Except for the HBT contribution all structure in the soft component is interpreted to result from local measure conservation during string fragmentation. Such 'canonical suppression' is dependent on local particle density.

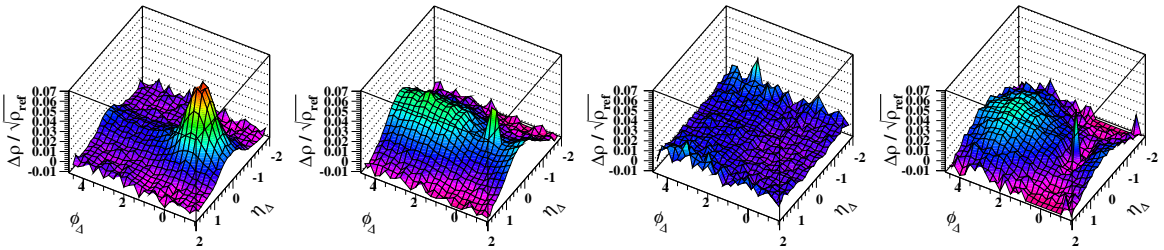

Figure 5.6-1. Two-particle correlations on $(\eta_\Delta, \phi_\Delta)$ for like-sign (LS) and unlike-sign (US) pairs respectively and for data (left panels) and the Pythia Monte Carlo (right panels).

The modeling of the US pair correlation contains two factors. One factor is a 1D peak on η_Δ consistent with a gaussian shape. The other factor is a negative 2D peak at the origin representing local canonical suppression of net transverse momentum. The negative peak has comparable widths on the two difference variables but with a shape that is less peaked than a gaussian. The order of application of those structures is important. The 2D negative same-side peak is imposed on the 1D peak on η_Δ as a form of canonical suppression. That relation is in contrast to the corresponding structure obtained from the Pythia Monte Carlo.

The second two panels show Pythia-6.222 soft-component correlations for LS and US charge combinations. The negligible soft LS correlations for Pythia are not directly comparable to data, because quantum correlations (HBT) which dominate LS structure in the data are not modeled in Pythia. The Pythia US correlations should correspond to data but are quite different. The soft US correlation is a single, broad away-side ($|\phi_\Delta| \sim \pi$) peak, with slightly larger width on ϕ_Δ. That peak shape and position could represent two-body breakup of 'prehadrons,' with a random distribution of source motion. That result conflicts strongly with the structure in the second panel representing charge and transverse-momentum conservation during longitudinal string fragmentation. There appears to be a *qualitative difference* between the Pythia representation of string fragmentation and the physical system.

5.7 $y_{t\Sigma}$ systematics of hard-component correlations on $(\eta_\Delta, \phi_\Delta)$ and low-Q^2 partons in p-p collisions at $\sqrt{s} = 200$ GeV

R. J. Porter and T. A. Trainor

Fig. 5.7-1 (first panel) shows two-particle correlations on transverse-rapidity space (y_{t1}, y_{t2}). The correlation structure is described on sum and difference variables $y_{t\Sigma} \equiv y_{t1}+y_{t2}$ and $y_{t\Delta} \equiv y_{t1}-y_{t2}$. *Inclusive* soft and hard components, representing longitudinal string and transverse parton fragments respectively, are bounded by the broader white lines (lower-left and upper-right regions respectively). Hard-component fractions for an exclusive analysis are defined by the narrower yellow lines (the grid along the sum diagonal). The solid green boxes in the upper-right corner represent regions typically explored in *leading-particle* analyses based on high-p_t 'trigger' particles. The dashed extensions represent cuts for extended leading-particle analyses applied to heavy ion collisions. We summarize here hard-component correlations corresponding to specific regions of that space defined by the grid of rectangles or bins along sum axis $y_{t\Sigma}$ numbered $1, \cdots, 12$.

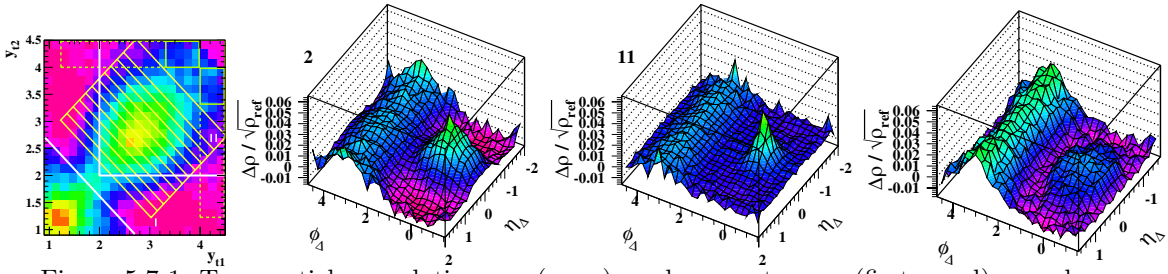

Figure 5.7-1. Two-particle correlations on (y_t, y_t) used as a cut space (first panel), correlations on $(\eta_\Delta, \phi_\Delta)$ for smaller $y_{t\Sigma}$ (second panel) and larger $y_{t\Sigma}$ (third panel) and small-$y_{t\Sigma}$ correlations from Pythia.

The second panel is a joint *auto*correlation (projection by averaging onto difference variables) on angular difference variables $(\eta_\Delta, \phi_\Delta)$ with pairs from the second bin on $y_{t\Sigma}$. The most probable combination is two particles each with $p_t \sim 0.6$ GeV/c. The same-side peak (jet cone) is broad but well-defined. The away-side ridge (particle pairs from dijets) is uniform on η_Δ as expected. This is a remarkable result for particles with such low p_t and illustrates the power of the autocorrelation technique. There is no model dependence or trigger bias other than the cut on $y_{t\Sigma}$. The third panel shows correlations for the 11^{th} bin, corresponding to $p_t \sim 2.5$ GeV/c for each particle. The same-side cone is much narrower, as is the away-side peak on azimuth ϕ. That result is more typical of a leading-particle analysis. The last panel shows results for the Pythia Monte Carlo, also from the second bin on $y_{t\Sigma}$, showing a much broader (especially on η_Δ) and less-defined peak than in the second panel. The general trend of the data, as in the second and third panels, is reduction of peak widths on $(\eta_\Delta, \phi_\Delta)$ with increasing $y_{t\Sigma}$. The angular widths are determined by the mean fragment momentum $\hat{j}_t$ perpendicular to the parton momentum (jet thrust) axis, relative to the particle p_t in the form $\hat{j}_t/p_t$. In following articles we examine the systematics of $\hat{j}_t$ *vs* $y_{t\Sigma}$ separately on η and ϕ for values of parton Q^2 previously inaccessible.

5.8 Jet morphology for low-Q^2 partons from low-p_t angular correlations

T. A. Trainor

Jet structure is characterized in part by two-particle angular correlations of the hadron fragments, both intra-jet (within one jet) and inter-jet (between opposing dijets). The conventional method to describe angular correlations of fragments in the absence of full jet reconstruction is as a *conditional* distribution relative to a leading or trigger particle (*e.g.,* the highest-p_t particle in an event). The distribution of 'associated' particles relative to the trigger particle is an estimator for full jet reconstruction. Angular correlations relative to the trigger reveal peaked angular distributions with widths on η and ϕ. From those widths the mean momenta of particles perpendicular to the jet thrust axis in the two directions is determined. The conventional asymmetric (conditional) expression for $j_{t\phi}$ is

$$\overline{\langle j^2_{t\phi}\rangle} = \frac{\left\langle p^2_{t,assoc}\right\rangle_{SS}}{1+\langle x^2_{at}\rangle}\left\{\left\langle \sin^2(\phi_{ta})\right\rangle_{SS} + 2\left\langle \sin^2(\phi_{ap})\right\rangle\left\langle \sin^2(\phi_{tp})\right\rangle\right\}, \quad (1)$$

where t denotes trigger, a denotes associated, p denotes parton, $x_{ta} = p_{t,assoc}/p_{t,trigger}$ and SS denotes same-side (intra-jet) pairs. For jets from low-Q^2 partons we cannot differentiate trigger and associated particles. The treatment must be symmetric and unbiased. I define a more general, symmetrized expression as

$$\overline{\langle j^2_{t\phi}\rangle} = \frac{(m_\pi/2)^2\exp\{y_{t\Sigma}\}}{2\cosh\{y_{t\Delta}\}}\left\{\left\langle \sin^2\left(\phi_\Delta/\sqrt{2}\right)\right\rangle_{SS} + 2\left\langle \sin^2\left(\phi_\Delta/2\sqrt{2}\right)\right\rangle^2_{SS}\right\}, \quad (2)$$

where $y_{t\Sigma}$ and $y_{t\Delta}$ are sum and difference variables on transverse rapidity space (y_{t1}, y_{t2}), and $\phi_\Delta \equiv \phi_1 - \phi_2$ is the difference variable on pair space (ϕ_1, ϕ_2). A similar expression can be defined for the angular width and j_t on η_Δ.

The inter-jet angular correlation on azimuth of particle pairs from opposed jets (dijets) is wider than the width of intra-jet azimuth correlations. The excess width or 'k_t broadening' is attributed to the transverse momenta k_t of partons prior to scattering, which produces an *acoplanarity* of the two jets with respect to the collision axis. The conventional form based on a trigger particle is

$$\left\langle z^2\right\rangle\left\langle k^2_{t\phi}\right\rangle = \frac{\left\langle p^2_{t,assoc}\right\rangle_{SS}}{1+\langle x^2_{at}\rangle}\,\frac{\left\{\langle \sin^2(\phi_{ta})\rangle_{AS} - \langle \sin^2(\phi_{ta})\rangle_{SS}\right\}}{1-2\langle \sin^2(\phi_{ta})\rangle_{SS}}, \quad (3)$$

where z is an estimate of ratio $p_{t,trigger}/p_{t,parton}$ and AS denotes away-side (inter-jet) pairs. The symmetrized equivalent is

$$\left\langle z^2\right\rangle\left\langle k^2_{t\phi}\right\rangle = \frac{(m_\pi/2)^2\exp\{y_{t\Sigma}\}}{2\cosh\{y_{t\Delta}\}}\,\frac{\left\{\left\langle \sin^2\left(\phi_\Delta/\sqrt{2}\right)\right\rangle_{AS} - \left\langle \sin^2\left(\phi_\Delta/\sqrt{2}\right)\right\rangle_{SS}\right\}}{1-2\left\langle \sin^2\left(\phi_\Delta/\sqrt{2}\right)\right\rangle_{SS}}. \quad (4)$$

The symmetrized expressions are used in the following studies (see Sec. 5.9 and 5.11) to extract jet transverse momenta from angular correlations in p-p collisions for previously inaccessible low-Q^2 partons.

5.9 j_t systematics for low-Q^2 partons from hadron fragment angular widths on azimuth and pseudorapidity in p-p collisions at $\sqrt{s} = 200$ GeV

R. J. Porter and T. A. Trainor

We fit same-side ($|\phi_\Delta| < \pi/2$) angular correlations (jet cone) for 12 pair classes defined as intervals on $y_{t\Sigma}$ with a 2D Gaussian and extract widths on pseudorapidity and azimuth for like-sign (LS), unlike-sign (US) and total (CI) pairs. Those widths are plotted in the first two panels of Fig. 5.9-1 *vs* $\exp\{-y_{t\Sigma}/2\} \propto 1/\sqrt{p_{t1}\, p_{t2}}$, that is, proportional to the inverse geometric mean of the pair momenta. The corresponding mean particle p_t is given at the top of the first panel. The dashed diagonal lines in the first two panels represent '$\hat{j}_t$ scaling' – assuming $\hat{j}_t$ ($r.m.s.$ j_t) is independent of hadron momentum, and expected to be the limiting case for larger p_t. We observe a dramatic departure from that expectation for these low fragment momenta ($p_t < 2.5$ GeV/c). However, with the autocorrelation technique we observe that jet structure is very well defined, even down to hadron pairs with particle $p_t \sim 0.35$ GeV/c. The hatched regions to the left in those panels show the values measured for minimum-bias hard component hadrons, which are weighted toward lower p_t.

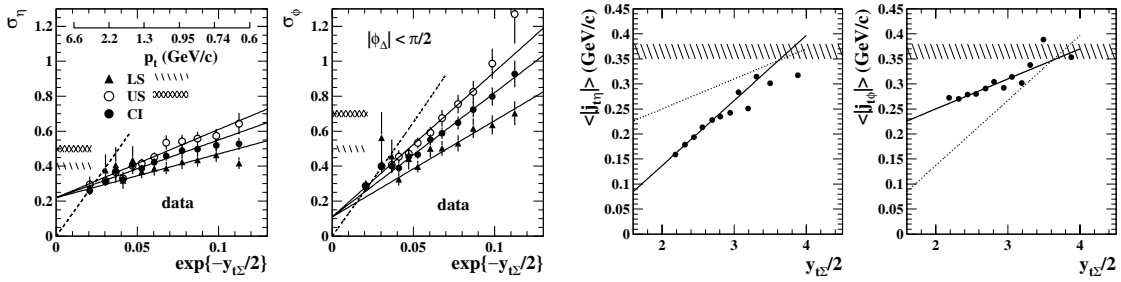

Figure 5.9-1.

By applying the formula

$$\overline{\langle j_{tx}^2 \rangle} = \frac{(m_\pi/2)^2 \exp\{y_{t\Sigma}\}}{2\cosh\{y_{t\Delta}\}} \left\{ \left\langle \sin^2\left(x_\Delta/\sqrt{2}\right)\right\rangle_{SS} + 2\left\langle \sin^2\left(x_\Delta/2\sqrt{2}\right)\right\rangle_{SS}^2 \right\} \qquad (1)$$

with the values of $(y_{t\Sigma}, y_{t\Delta})$ defined on the (y_{t1}, y_{t2}) cut space we obtain j_t values for $x = \eta$, ϕ from the corresponding angular widths. We observe a strong decrease in both momentum components with decreasing $y_{t\Sigma}$ (parton Q^2). We also observe substantial differences in the j_t values in η and ϕ directions, converging however to the 'j_t scaling' expectation at larger $y_{t\Sigma}$ (hatched bands). The asymmetry about the thrust axis observed for these low-p_t fragments (the difference in $\hat{j}_t$s for η and ϕ) is much larger than measured at LEP by the so-called 'Major' statistic (representing net eccentricity of transverse momentum components relative to thrust axis). It is notable that the orientation of the j_t asymmetry (major axis in the (ϕ, p_t) plane) is parallel to the 'contact' plane of the parton collision. That orientation is opposite to what is found for low-p_t jet fragments in central heavy ion collisions, as described in the following article.

5.10 j_t orientation for low-Q^2 parton fragments and broadening of the minijet peak on pseudorapidity in central Au-Au relative to p-p collisions

T. A. Trainor

Having obtained angular widths on η and ϕ for low-Q^2 partons from p-p collisions, and previously from central Au-Au collisions, we can compare the j_t values for η and ϕ in the two cases. We previously observed that the same-side minijet angular correlation in Au-Au collisions is dramatically broadened on η with increasing centrality and significantly narrowed on ϕ.[1] We now compare the Au-Au angular correlations (at $\sqrt{s} = 130$ GeV) directly with angular correlations for p-p minimum-bias collisions (at $\sqrt{s} = 200$ GeV), and interpret the widths of the minijet peak in terms of j_t. The energy difference (130 *vs* 200) should not interfere with qualitative comparison and interpretation of the width evolution.

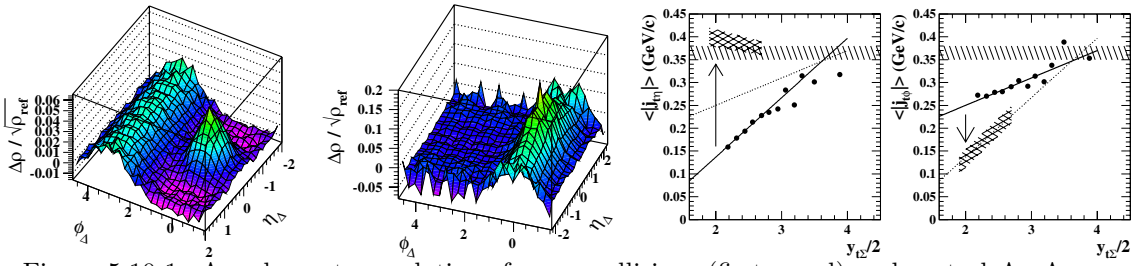

Figure 5.10-1. Angular autocorrelations for p-p collisions (first panel) and central Au-Au collisions (second panel), and corresponding inferred $\hat{j}_{t\eta}$ (third panel) and $\hat{j}_{t\phi}$ (fourth panel) momentum components from corresponding angular widths

Fig. 5.10-1 shows in the first panel minimum-bias p-p angular correlations, in the second panel Au-Au angular correlations for central collisions, and in the last two panels the $\hat{j}_t$ distributions on $y_{t\Sigma}/2$ from the previous article, with additional hatched regions representing the heavy ion angular correlation widths suitably converted. The away-side azimuth correlation for central Au-Au is negligible once the sinusoid for elliptic flow has been subtracted, as in this case.

The p-p widths in the first panel are $\sigma_\eta = 0.5$ and $\sigma_\phi = 0.8$. The widths for Au-Au central collisions in the second panel are $\sigma_\eta = 1.37$ and $\sigma_\phi = 0.55$. The latter translate to the added crosshatched regions in the last two panels. We observe that the roles of η and ϕ are interchanged as p-p $\rightarrow$ central Au-Au. The larger $\hat{j}_t$ value on *azimuth* ϕ in p-p is reduced to the p-p pseudorapidity η value in central Au-Au, whereas the smaller $\hat{j}_t$ value on *pseudorapidity* η in p-p increases dramatically to exceed the high-p_t *in vacuo* p-p value in central Au-Au. The latter trend suggests that fragments of low-Q^2 partons acquire some fraction of the longitudinal Hubble expansion velocity of the bulk medium during fragmentation. The parton fragmentation process is strongly modified by the medium.

[1] CENPA Annual Report, University of Washington (2004) p. 52.

5.11 k_t systematics for fragmentation of low-Q^2 partons from jet angular widths on azimuth in p-p collisions at $\sqrt{s} = 200$ GeV

R. J. Porter and T. A. Trainor

Prior to a p-p collision, partons within the nucleons are distributed on transverse momentum k_t. If two partons collide, exchanging some momentum q, the momentum components k_t for the two partons are manifested statistically in the form of a jet acoplanarity: away-side (interjet) fragment angular correlations on azimuth are then broadened relative to same-side (intrajet) azimuth correlations. We measure the angular width of the *away-side* azimuth correlation of hadron pairs ($|\phi_1 - \phi_2| > \pi/2$) and compare it with that of the same-side azimuth correlation to infer the mean transverse momentum k_t of partons prior to scattering. The first panel of Fig. 5.11-1 shows angular widths of away-side correlations as a function of the geometric mean of hadron p_t in the form $\exp\{-y_{t\Sigma}/2\}$. That form is proportional to the inverse of the *geometric* mean p_t of the fragments. The dashed line represents the 'k_t scaling' that might be expected if k_t were independent of fragment p_t or parton Q^2. The hatched region represents the widths for minimum-bias hadron fragments, which favor the small-p_t region. The second panel represents the Pythia Monte Carlo. The main difference is substantially smaller widths.

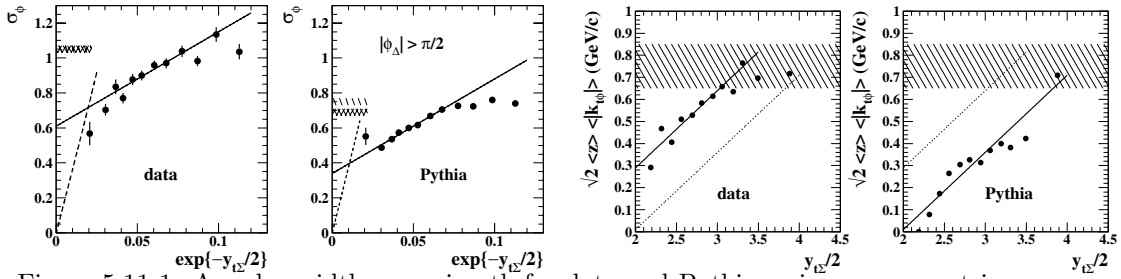

Figure 5.11-1. Angular widths on azimuth for data and Pythia *vs* inverse geometric mean particle p_t in the form $\exp\{-y_{t\Sigma}/2\}$, and corresponding inferred k_t values.

We then convert the angular widths to k_t values according to the symmetrized formula

$$\left\langle z^2 \right\rangle \left\langle k_{t\phi}^2 \right\rangle = \frac{(m_\pi/2)^2 \exp\{y_{t\Sigma}\}}{2\cosh\{y_{t\Delta}\}} \frac{\left\{ \left\langle \sin^2\left(\phi_\Delta/\sqrt{2}\right)\right\rangle_{AS} - \left\langle \sin^2\left(\phi_\Delta/\sqrt{2}\right)\right\rangle_{SS} \right\}}{1 - 2\left\langle \sin^2\left(\phi_\Delta/\sqrt{2}\right)\right\rangle_{SS}}, \qquad (1)$$

where z estimates the mean value of the ratio of 'trigger particle' momentum to parton momentum. At larger p_t that value is approximately 0.75, but is a falling function of p_t for smaller p_t as in this case. We observe that below $y_{t\Sigma}/2 \sim 3.3$ (hadron $p_t \sim 2$ GeV/c) the k_t values fall below the k_t scaling trend (dashed band) to an increasing degree with smaller $y_{t\Sigma}$ (smaller Q^2). The Pythia numbers are substantially displaced below the data, corresponding to the trend for angular widths.

5.12 Away-side (y_{t1}, y_{t2}) correlations and the *other* k_t broadening in p-p collisions at $\sqrt{s} = 200$ GeV

T. A. Trainor

As noted in the previous article, conventional k_t broadening refers to jet acoplanarity and results in increase of the away-side or inter-jet azimuthal angular correlation width relative to the same-side or intra-jet width. We now consider the effect on y_t correlations of the initial-state parton k_t. The first panel of Fig. 5.12-1 shows the same-side US (y_t, y_t) correlation for p-p collisions, narrowly distributed on difference variable $y_{t\Delta}$. In the next panel we show the correspondent for away-side LS pairs. The away-side hard component is the same for LS and US pairs, and the LS combination essentially eliminates the string fragment soft component. The away-side distribution is very different: broad on $y_{t\Delta}$ and terminating at $y_{t\Sigma} \sim 4$.

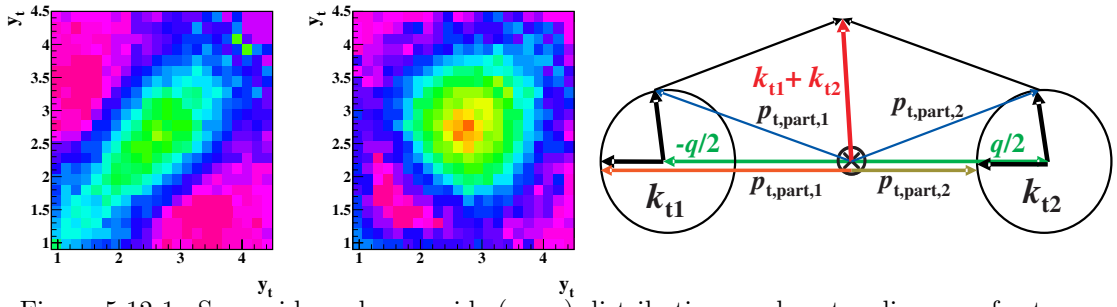

Figure 5.12-1. Same-side and away-side (y_t, y_t) distributions and vector diagrams for two k_t orientations with respect to parton momentum transfer q.

The explanation for that difference can again be described in terms of k_t broadening, but of a different kind. In the rightmost panel is a vector diagram showing the addition of parton k_t and momentum transfer q to form parton transverse momenta $p_{t,part,1}$ and $p_{t,part,2}$. The effect of k_t on hadron correlations is maximal when the two parton k_ts are parallel, which we assume here (obviously, the two vectors are randomly oriented for each parton collision, and we consider mean behaviors). In the conventional k_t-broadening picture the k_ts (black vectors vertical in the diagram) are pictured normal to the momentum transfer vector (green $q/2$ horizontal vectors). The result is the acoplanarity of the parton vectors as shown by the blue arrows and k_t broadening of the away-side azimuth correlation.

However, in an alternative configuration the k_ts are oriented parallel to the momentum transfer (black vectors horizontal in the diagram). The result is *unequal* red and olive parton momentum vectors. Since the initial-state parton k_t is distributed nearly independently of parton momentum transfer (by hypothesis), if the momentum transfer (Q^2) decreases, the relative effect, the asymmetry in the parton momenta relative to the mean, becomes large. Since $y_{t\Delta}$ is essentially the log of the fragment p_t ratio this alternative form of k_t broadening implies increasing distribution width on $y_{t\Delta}$ with decreasing $y_{t\Sigma}$, as observed in the second panel. A further consequence of k_t oriented parallel to parton momentum transfer is that for small enough Q^2 one of the partons is *stopped* while the other is accelerated to external fragmentation. The result is monojet emission at low Q^2. That would explain the absence of away-side hadron correlations below $y_{t\Sigma} \sim 4$. The monojet momentum is supplied by the longitudinal spectator system (in the form of the k_t), and that system recoils collectively.

5.13 $p_t \otimes p_t$ correlations on $(\eta_\Delta, \phi_\Delta)$ in p-p collisions at $\sqrt{s} = 200$ GeV

C. Han* and T. A. Trainor

We have previously inverted $\langle p_t \rangle$ fluctuation scale dependence to obtain joint p_t autocorrelations on $(\eta_\Delta, \phi_\Delta)$. The integral equation which relates fluctuations to correlations is

$$\Delta\sigma^2_{p_t:n}(m\,\epsilon_\eta, n\,\epsilon_\phi) \equiv 4\sum_{k,l=1}^{m,n} \epsilon_\eta\epsilon_\phi\, K_{mn;kl}\, \Delta\rho(p_t:n; k\epsilon_\eta, l\epsilon_\phi)/\sqrt{\rho_{ref}(n; k\epsilon_\eta, l\epsilon_\phi)}. \quad (1)$$

The autocorrelation density ratio $\Delta\rho/\sqrt{\rho_{ref}}$ can also be obtained by direct formation of pair ratios. The basic correlation measure for a pair of bins (a, b) is

$$\overline{(p_t - n\hat{p}_t)_a (p_t - n\hat{p}_t)_b}/\sqrt{\bar{n}_a\, \bar{n}_b} \quad (2)$$

where the overline is the average over an event ensemble and $\hat{p}_t$ is the ensemble-average mean p_t. That quantity is within a factor Pearson's correlation coefficient for bin pair (a, b), with number variances in the denominator replaced by their Poisson-equivalent mean multiplicities. To form the joint autocorrelation on $(\eta_\Delta, \phi_\Delta)$, averages of that quantity over bin pairs separated on (η, ϕ) by specific differences form the autocorrelation histogram.

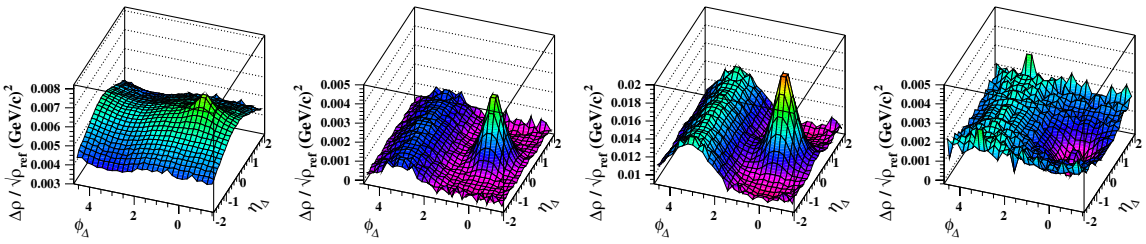

Figure 5.13-1.

In Fig. 5.13-1 the left three panels are joint autocorrelations for three multiplicity classes of p-p collisions at $\sqrt{s} = 200$ GeV and charged particles in the STAR η acceptance $|\eta| < 1$: respectively 2-4, minimum-bias and greater than 9 for the three panels. The same-side jet cone and away-side ridge are quite apparent in the center two panels, as for number correlations, but the peaks are sharper (non-Gaussian). For the lowest multiplicity class on the left, the jet cone is just barely visible on a soft background. We expect, on the basis of the two-component analysis of n_{ch} dependence of p-p p_t distributions, that the frequency of hard scattering in p-p collisions increases nearly linearly with n_{ch}. The results for p_t correlations are roughly consistent with that trend. The rightmost panel shows the CD = LS - US charge-pair combination for the same multiplicity class as the third panel. The peak is negative as expected and quite broad, much broader than the peak for the CI = LS + US combination in the third panel. That shape is consistent with charge conservation being most important for the lowest-p_t parton fragments having the largest angular spread. The peak amplitude [0.0045 (GeV/c)^2] and widths ($\sigma_{\eta_\Delta} = 0.53$ and $\sigma_{\phi_\Delta} = 0.72$) for the minimum-bias class in the second panel agree very well with p_t correlations for the most peripheral centrality of Au-Au collisions (80-90%) obtained by fluctuation inversion, providing an excellent consistency check on the inversion method (see Sec. 5.16).

*Presently at City of Hope National Medical Center, 1500 E. Duarte Road, Duarte, CA 91010.

5.14 Power-law centrality and Hijing Au-Au collisions at $\sqrt{s_{NN}} = 200$ GeV

D. J. Prindle and T. A. Trainor

The power-law centrality treatment is based on the observation that the minimum-bias distribution $d\sigma/dn_{ch}$ plotted *vs* n_{ch} on a log-log format exhibits linear or *power-law* behavior, with slope -3/4. That trend suggested that plotting $1/\sigma_0\, d\sigma/dn_{ch}^{1/4}$ *vs* $n_{ch}^{1/4}$ should be approximately constant. Particle-production physics should then be manifested in small deviations from the power-law trend, which would then be more accessible. The minimum-bias distribution in its conventional semi-log format is plotted in the first panel of Fig. 5.14-1 for Hijing with jet quenching turned off and on (the latter extending to larger n_{ch}). The second panel shows the same data replotted in the power-law format. That format has two advantages: 1) the physical information is visually accessible on a linear scale, and 2) the half-maximum points at the two ends denoted n_p and n_0 are estimators for the correspondents on n_{ch} of participant numbers $n_{part}/2 = 1$ (p-p collisions) and $n_{part}/2 \simeq 197$ ($b = 0$ Au-Au collisions). Those endpoints constrain the relation of n_{ch} to the A-A collision geometry at both ends of the distribution. The result is a precise relation between collision impact parameter b and particle multiplicity n_{ch}.

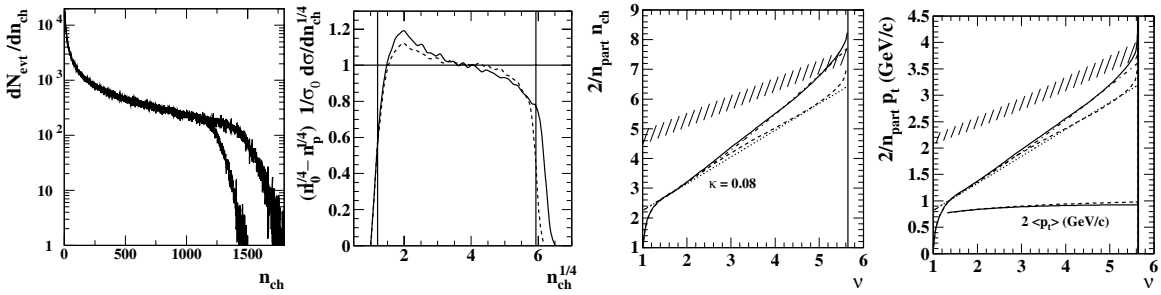

Figure 5.14-1. Minimum-bias distribution in conventional semi-log format and power law format, and particle-number and p_t production *vs* mean participant path length ν in Hijing Au-Au collisions.

The same treatment can be applied to distributions on participant number and binary-collisions number in a Glauber simulation. In each case the parameters n_{part} and $\nu \equiv 2n_{binary}/n_{part}$ can be related to collision impact parameter b. ν estimates the average path-length of a participant nucleon in units of number of encountered nucleons. That quantity is a purely geometric estimator not linked to a nuclear cross section, related in meaning however to the similar quantity conventionally used to measure centrality in p-A collisions. Combining power-law analysis of Glauber Monte Carlo and data one then has precise relations among n_{part}, ν and n_{ch} which were used to produce the third and fourth panels of the figure. The dashed curves are for quench-off Hijing collisions and the solid curves for quench-on collisions. The dotted and dash-dot lines provide visual straight-line references for the data curves. The vertical solid lines estimate the maximum ν value for Au-Au collisions, corresponding to $b = 0$ and $n_{part}/2 \sim 197$. By this analysis we have determined the distribution on centrality measure ν of produced particle multiplicity and transverse momentum p_t per participant. The hatched bands summarize observed data distributions for 130 and 200 GeV Au-Au collisions. There are significant differences between Hijing and data.

5.15 Transverse momentum correlations inferred from $\langle p_t \rangle$ fluctuations in Au-Au collisions at $\sqrt{s} = 200$ GeV from the Hijing Monte Carlo

Q. J. Liu,* D. J. Prindle and T. A. Trainor

We inverted the scale dependence of $\langle p_t \rangle$ fluctuations from Hijing-1.37 collisions to construct joint p_t autocorrelations on pseudorapidity and azimuth angle difference variables. Fig. 5.15-1 shows autocorrelations for central 0-15% collisions and two Hijing configurations: quench-off and quench-on (first and second panels). The autocorrelations have similar features: a same-side ($|\phi_\Delta| < \pi/2$) peak and an away-side ($|\phi_\Delta| > \pi/2$) ridge. The same-side peak (jet cone) is identified with fragments from *minimum-bias* partons (minijets) – no high-p_t trigger condition was imposed. Variation of the near-side peak with centrality is limited. For quench-off collisions there is a modest increase in peak amplitude and small symmetric decrease in peak widths with increasing centrality. For quench-on collisions those trends are reversed. Amplitudes and widths from model fits are plotted in the third and fourth panels *vs* centrality measure ν, which estimates mean participant path length in number of encountered nucleons. Lines are drawn to guide the eye, with the constraint that quench-off and quench-on parameters should extrapolate to the same value for $\nu = 1$ (p-p collisions).

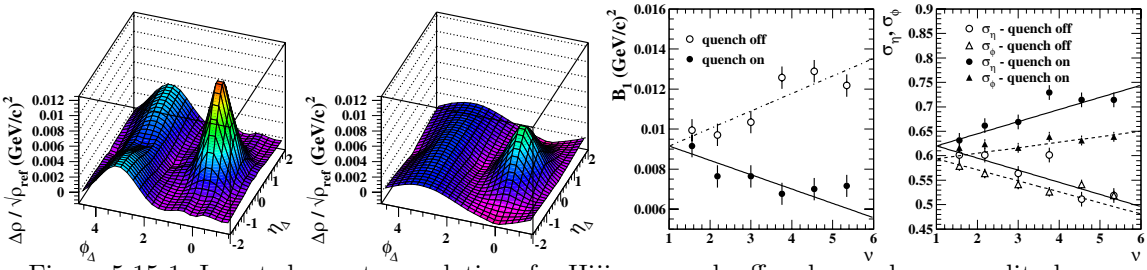

Figure 5.15-1. Inverted p_t autocorrelations for Hijing quench off and quench on, amplitudes of the near-side peak for the two cases, and corresponding widths.

We expect minijet production to follow binary-collision scaling: an increase with centrality nearly proportional to mean path length ν. The near-side peak amplitude in the p_t autocorrelation should then be proportional to ν, but the observed increase is much slower (note the offset zero in the third panel). Autocorrelation changes in response to jet quenching are closer to expectations. With quenching invoked the near-side amplitude is significantly reduced relative to quench-off, to an extent proportional to ν. The linear dependence on ν of jet-quenching effects is expected for this model. While ν estimates mean initial-state path length for participant nucleons it is also proportional to the average distance through the medium traversed by an outgoing parton. The detailed centrality dependence of minijet correlations in Hijing seems inconsistent with expectations for binary-collision scaling. The near-side peak amplitude for quench-off collisions, representing hard parton scattering, increases by only 30% from p-p ($\nu = 1$) to central Au-Au, where one would expect a $4\times$ increase for binary-collision scaling. The near-side peak width variations with centrality are small and symmetric on $(\eta_\Delta, \phi_\Delta)$. These Hijing simulation results provide a valuable reference for heavy ion collision data from RHIC. We have introduced a novel analysis technique which reveals in heavy ion collisions new transverse-momentum correlation structures related to parton scattering, in-medium parton energy loss and parton fragmentation.

*Presently at University of Science and Technology of China, Department of Modern Physics, Hefei, Anhu, 230026, People's Republic of China.

5.16 $\langle p_t \rangle$ fluctuation scale dependence and inversion to p_t autocorrelations for RHIC Au-Au collisions at $\sqrt{s} = 200$ GeV

Q. J. Liu,* D. J. Prindle and T. A. Trainor

The scale dependence of $\langle p_t \rangle$ fluctuations for Au-Au collisions at $\sqrt{s_{NN}} = 200$ GeV has been inverted to obtain p_t autocorrelations on pseudorapidity and azimuth angle difference variables. Fig. 5.16-1 (first panel) shows the scale variation of $\langle p_t \rangle$ fluctuations up to the limiting STAR acceptance for central Au-Au collisions at $\sqrt{s_{NN}} = 200$ GeV. The second panel shows the corresponding 2D autocorrelation inferred from the fluctuation scale dependence by inverting an integral equation and subtracting three azimuthal multipole components consisting of monopole (constant offset), dipole $\cos(\phi_\Delta)$ and quadrupole $\cos(2\phi_\Delta)$. The residual autocorrelation retains three localized structures: a same-side positive peak, a same-side negative peak (apparent as the regions of *negative* correlation immediately adjacent to the positive peak on ϕ_Δ) and an away-side peak. For the more central collisions we observe that the same-side positive peak is substantially elongated along η_Δ and significantly *narrowed* along ϕ_Δ (a similar effect was observed for number correlations). Those three correlation structures are of primary interest in connection with minijet dissipation in A-A collisions.

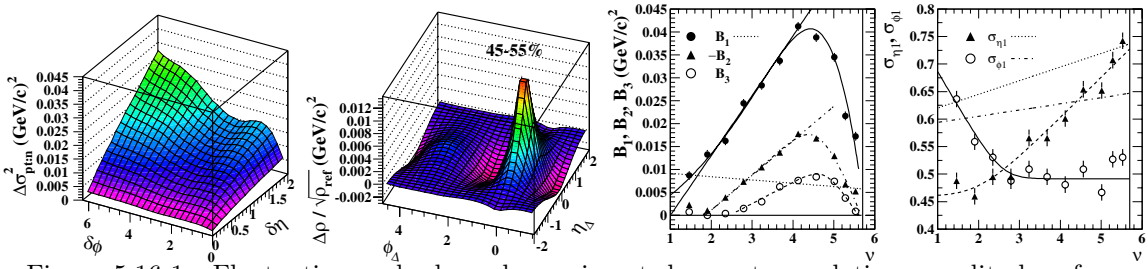

Figure 5.16-1. Fluctuation scale dependence, inverted p_t autocorrelation, amplitudes of three peak features and angular widths of same-side positive peak.

The three peak features vary strongly in shape and amplitude with collision centrality, as shown in the third and forth panels. Autocorrelations for a range of centralities were fitted with the sum of a near-side positive peak B_1, a near-side negative peak B_2 (signed number) and an away-side peak B_3. Best-fit amplitudes for all peaks and widths for the near-side positive peak are plotted in the last two panels *vs* mean participant path length ν. The peak amplitudes increase with centrality to a maximum and then decrease sharply for the most central collisions. The near-side positive-peak width on η_Δ increases monotonically with centrality, while that on ϕ_Δ decreases. The width trends are qualitatively similar to equivalent measurements of angular (number) correlations where a large width increase on η_Δ was interpreted as due to strong coupling of low-p_t partons to the longitudinally-expanding colored medium. An equivalent analysis of $\langle p_t \rangle$ fluctuations for Hijing collisions (see Sec. 5.15) reveals qualitatively different centrality dependence for the Monte Carlo. The perturbative treatment of parton energy loss in Hijing appears to disagree strongly with the observed process for the minimum-bias partons which dominate p_t correlations in Au-Au collisions. RHIC data, in contrast to Hijing, indicate that the final-state multiplicity fraction derived from minijets grows very strongly with centrality in RHIC collisions.

*Presently at University of Science and Technology of China, Department of Modern Physics, Hefei, Anhu, 230026, People's Republic of China.

5.17 Recoil of the bulk medium in Au-Au collisions at $\sqrt{s_{NN}} = 200$ GeV

D. J. Prindle and T. A. Trainor

We have inverted $\langle p_t \rangle$ fluctuations from Au-Au collisions to obtain p_t autocorrelations (see Sec. 5.16). We can decompose those autocorrelations into multipole components (sinusoids depending only on azimuth) which we subtract, and a residual distribution which contains three peak features. We examine the properties of those peaks with a detailed model fit. In Fig. 5.17-1 first panel is a p_t autocorrelation for 20-30% central Au-Au collisions. The autocorrelation is fitted with the model function defined in Eq. (1), a sum of near-side positive peak B_1, near-side negative peak B_2 (signed number) and away-side peak B_3, each with the same form

$$F = \sum_{i=1}^{3} B_i \exp\left\{ - \left| \frac{\eta_\Delta}{\sqrt{2}\,\sigma_{\eta i}} \right|^{\tau_{\eta i}} - \left| \frac{\phi_\Delta - \delta_{i3}\,\pi}{\sqrt{2}\,\sigma_{\phi i}} \right|^{\tau_{\phi i}} \right\}, \tag{1}$$

where δ_{i3} is a Kronecker delta. That function includes exponents τ as shape parameters. In contrast to a gaussian ($\tau \equiv 2$), which best describes near-side peaks for number autocorrelations, best-fit exponents for these p_t autocorrelations were found to be $\tau_{\eta 1} = \tau_{\eta 3} = \tau_{\phi 1} = 1.5 \pm 0.1$, with $\tau_{\phi 2} = 2.5 \pm 0.1$, $\tau_{\phi 3} = 1.9 \pm 0.1$ and $\tau_{\eta 2} = 1.7 \pm 0.1$ (for all centralities). Widths for near-side negative and away-side peaks varied nearly linearly over the ranges $0.75 < \sigma_{\eta 2} < 1.1 \pm 0.1$, $0.9 < \sigma_{\eta 3} < 1 \pm 0.1$, $\sigma_{\phi 2} \sim 2.1 \pm 0.2$ and $2.4 > \sigma_{\phi 3} > 1.5 \pm 0.1$.

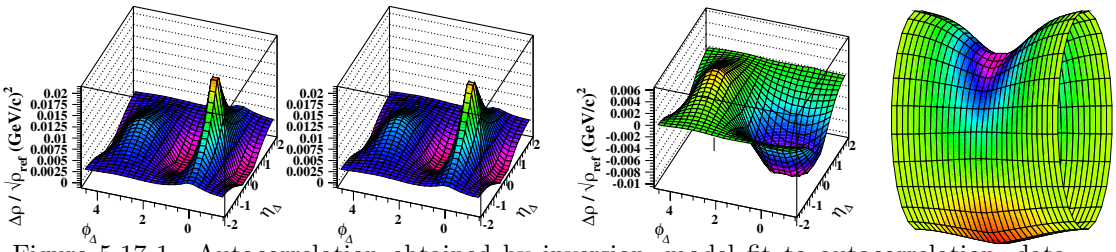

Figure 5.17-1. Autocorrelation obtained by inversion, model fit to autocorrelation, data autocorrelation with positive same-side peak subtracted and the same in cylindrical format.

The model function for data in the first panel is shown in the second panel. The fit is excellent: the residuals are a few percent of the positive same-side peak amplitude. In the third panel we show the data distribution in the first panel minus the model representation of the same-side positive peak in the second panel. The negative same-side peak has a very different structure on azimuth from the same-side positive peak subtracted; it is much broader and flatter. Thus, the 'cross-talk' between positive and negative peaks in the fit is negligible. That distribution can also be plotted in a cylinder format, as shown in the fourth panel. In that format the structure is very suggestive of recoil of the bulk medium in response to the parton represented by the fragments in the positive same-side peak. If that interpretation is correct, we then observe what happens to the 'away-side' jet in the more central Au-Au collisions. The momentum is absorbed by the medium, which is reflected in its collective transverse velocity distribution. That distribution affects the hadrons produced from the bulk medium in the form of red shifts (the negative same-side peak) and blue shifts (the positive away-side peak) of the local event-wise p_t spectrum.

5.18 Energy dependence of $\langle p_t \rangle$ fluctuations from $\sqrt{s_{NN}} = 10$ to 200 GeV

Q. J. Liu,* D. J. Prindle, R. L. Ray† and T. A. Trainor

We have determined the $\sqrt{s_{NN}}$ (N-N CM collision energy) dependence of $\langle p_t \rangle$ fluctuations in heavy ion collisions from SPS to RHIC energies. Shown in Fig. 5.18-1 (left panel) is the dependence of $\langle p_t \rangle$ fluctuations on collision centrality ν, which estimates the mean participant-nucleon path length in number of encountered nucleons. Measurements are shown for six energies, the lowest two representing Pb-beam data at fixed-target beam energies 80 and 158 GeV/nucleon (labeled with corresponding CM energies) and the upper four being STAR data at CM energies 20, 62 130 and 200 GeV. The next panel presents $\langle p_t \rangle$ fluctuation scale dependence on pseudorapidity bin size $\delta\eta$ for those energies. The third panel shows fluctuation amplitudes at the STAR detector acceptance scale and for the most central A-A collisions at the six collision energies. The solid curve represents the trend $\ln\{\sqrt{s_{NN}}/10.5\,\mathrm{GeV}\}$ which describes the data well. SSC-corrected data have had 3 MeV/c subtracted based on the inset in the second panel which reveals a small-scale contribution due to quantum and Coulomb correlations. We attribute the remaining large-scale (LSC) fluctuations to minijets based on other studies (see Sec. 5.16 and 5.15). The first panel reveals that fluctuations for peripheral collisions ($\nu \sim 1 - 2.5$) saturate with increasing energy by 62 GeV, whereas fluctuations for the more central collisions continue to increase monotonically with increasing energy.

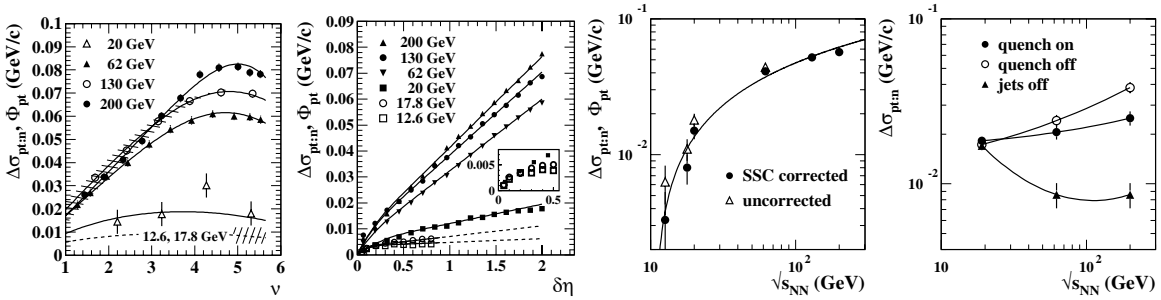

Figure 5.18-1. STAR and CERES $\langle p_t \rangle$ fluctuation (1) centrality ν and (2) scale $\delta\eta$ dependence. Energy dependence of large-scale correlations (LSC) for (3) data and (4) Hijing.

The right-most panel shows comparable results for Hijing Monte Carlo events with jet quenching (in-medium parton dissipation) on, off and with jet production turned off. We note a very different energy dependence for Hijing. In particular we observe that $\langle p_t \rangle$ fluctuations at 20 GeV are dominated by non-jet phenomena (string fragmentation). We infer from correlation studies (directly and by fluctuation inversion) that the principal mechanism for $\langle p_t \rangle$ fluctuations at RHIC is minijets. Thus, the energy dependence of the LSC component of those fluctuations is of considerable interest: what is the energy trend of hard scattering down to the lowest relevant collisions energies? We observe an apparent threshold for *observable* minijet production at about 10 GeV and monotonic increase thereafter, perhaps as $\ln\{\sqrt{s_{NN}}/10.5\,\mathrm{GeV}\}$. We observe a suggestion of saturation with increasing energy for the more peripheral A-A collisions, and presumably for p-p collisions as well.

*Presently at University of Science and Technology of China, Department of Modern Physics, Hefei, Anhu, 230026, People's Republic of China.

†Department of Physics, University of Texas, Austin, TX 78712.

5.19 Solving the RHIC HBT puzzle with chiral symmetry restoration

J. G. Cramer and G. A. Miller*

Many of the "signals" from analysis of Au+Au collisions at RHIC suggest that a quark gluon plasma (QGP) has been created in the initial stages of the collision. A major problem with such an interpretation has been that a QGP scenario would require a large source that has expanded for a long time before freeze out and has a long duration for emission of pions. On the other hand, analysis of RHIC data using HBT interferometry has been interpreted as indicating a relatively small unexpanded source with a very short pion emission duration. In the literature, this conundrum has been called the "RHIC HBT Puzzle".

In an effort to understand the origins of this problem, we undertook a new approach to RHIC physics that required the application of quantum wave mechanics and the nuclear optical model to the medium produced by the colliding systems. We formulated a new relativistic quantum mechanical description of the collision medium that included collective flow as well as absorption and refraction in a complex potential. We solved the Klein-Gordon wave equations for pions in the medium and calculated overlap integrals with these wave functions to obtain predictions of pion spectra and HBT radii. This numerical calculation was placed under the control of a Marquardt-Levenberg chi-squared minimization program that varied the 12 model parameters to obtain the best fit to STAR $\sqrt{s_{NN}}$=200 GeV Au+Au pion spectrum[1] and HBT radii.[2]

Our initial expectation was that the imaginary part of the optical potential would be important for simulating pion absorption, while the real potential with its refractive effects was included mainly for formal reasons. To our surprise, when the fitting began the real potential grew deeper and deeper as the fit improved, until it was essentially as deep as the pion mass. This result suggested to us that the pion must be losing mass in the hot dense medium of the collision because chiral symmetry had been partially restored in the medium. Therefore, we gave the optical potential the momentum dependence that is expected to describe a system in which chiral symmetry has been restored. The result of this inclusion was spectacular. Remarkably good fits to the STAR data, giving a chi-squared of about 3.7 per data point and 5.6 per degree of freedom, were obtained. These fits are shown in Fig. 5.19-1 and Fig. 5.19-2.

These results have now been published in Physical Review Letters[3] and already have been cited in the APS Physics News Update[4] and the Wall Street Journal.[5] Our results have provided a solution to the RHIC HBT Puzzle: the pion source at RHIC appears small and short in duration in HBT interferometry because it is being viewed through a distorted glass. Roughly half of the pions are absorbed, with those surviving emitted primarily from a "bright ring" near the outer surface of the medium. Moreover, the emerging pions must regain their

*Department of Physics, University of Washington, Seattle, WA 98195.

[1] J.Adams, *et al.*, Phys. Rev. Lett. **92**, 112301 (2004).

[2] J. Adams, *et al.*, Phys. Rev. C, submitted for publication, 2004; nucl-ex/0411036.

[3] J. G. Cramer, G. A. Miller, J. M. S. Wu and J-H. Yoon, Phys. Rev. Lett. **94**, 102302 (2005).

[4] P. Schewe and B. Stein, Physics News Update 723 #2, March 2005.

[5] S. Begley, Wall Street Journal, page B1, April 1, 2005.

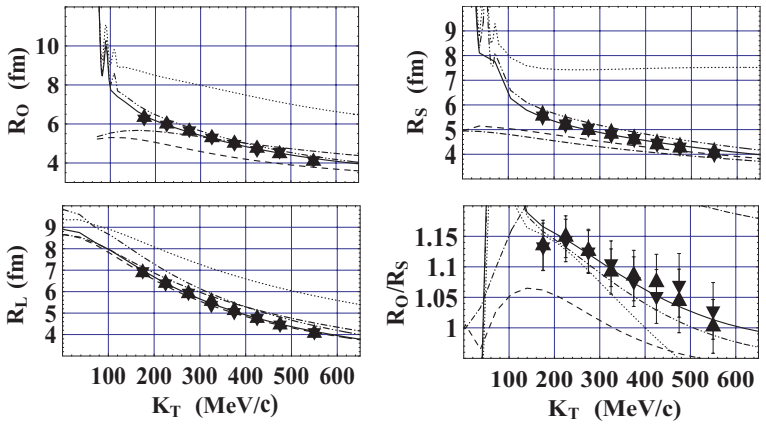

Figure 5.19-1. (color online) HBT Radii R_s, R_o, R_l and the ratio R_o/R_s; Data: ∇ (green) $\Rightarrow \pi^+\pi^+$; $\triangle$ (red) $\Rightarrow \pi^-\pi^-$. Curves: solid (black) $\Rightarrow$ full calculation; dotted (green) $\Rightarrow \eta_f = 0$ (no flow); dashed (red) $\Rightarrow$ Re[U]=0 (no refraction); dot-dashed (blue) $\Rightarrow U$=0 (no potential), double-dot-dashed (magenta) $\Rightarrow$ substituting Boltzmann for Bose-Einstein thermal distribution. Insets show predictions of low-K_T resonance behavior in R_o and R_s.

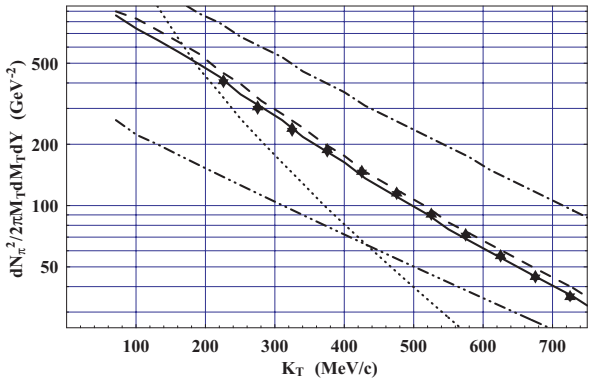

Figure 5.19-2. (color online) Pion momentum spectrum. Data: ∇ (green) $\Rightarrow \pi^+$; $\triangle$ (red) $\Rightarrow \pi^-$. Inset is low-K_T prediction.

mass by expending a sizable fraction of their kinetic energy in climbing out of the very deep well made by the real potential. When these effects are properly taken into account, the pion source size and emission duration are consistent with a QGP scenario. Further, in most lattice gauge studies of heated and compressed nuclear matter the chiral phase transition and the transition to a quark-gluon plasma occur under about the same conditions. Our inferred observation of a chiral phase transition at RHIC is therefore consistent with the presence of a quark-gluon plasma transition in RHIC collisions.

In closing, we note that this work represents the first direct observation of a chiral phase transition in a multiparticle system. The only other experimental support of chiral symmetry restoration comes from the structure of highly excited states of the nucleon. Therefore, we have developed a new tool for relativistic heavy ion physics, which we plan to use for investigating the onset and properties of chiral symmetry restoration as a function of energy and centrality in relativistic heavy ion collisions, using data at the very wide range of energies and systems that has already been provided by experiments at the AGS, SPS, and RHIC.

5.20 Pion entropy and phase space density in NA49 collisions

J. G. Cramer and the NA49 Collaboration*

Experiment NA49 at the CERN SPS has studied fixed-target Pb+Pb collisions at ^{208}Pb beam energies of 20, 30, 40, 80, and 158 GeV/A, corresponding to $\sqrt{s_{NN}}$ values of 6.3, 7.6, 8.8, 12.3 and 17.3 GeV, respectively. It is of considerable interest to use these data to study the energy dependence of the average pion phase space density $< f >$ and the total pion entropy dS_π/dy. During the past year we have begun such an analysis. Fig. 5.20-1 and Fig. 5.20-2 show two examples of preliminary results from this program.

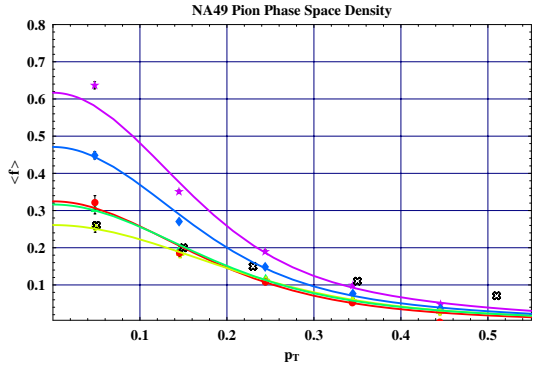

Figure 5.20-1. Average pion phase space density $< f >$ for central Pb+Pb collisions (0-10% of σ_T) with $\mid y \mid$<0.5. Symbols: E_{Lab} = 158 GeV/A (star), 80 GeV/A (diamond), 40 GeV/A (triangle), 30 GeV/A (plus), 20 GeV/A (circle). The curves are produced by fits to the pion spectra and HBT radii. The open X symbols show the results of a previous analysis of phase space density at 158 GeV/A.[1]

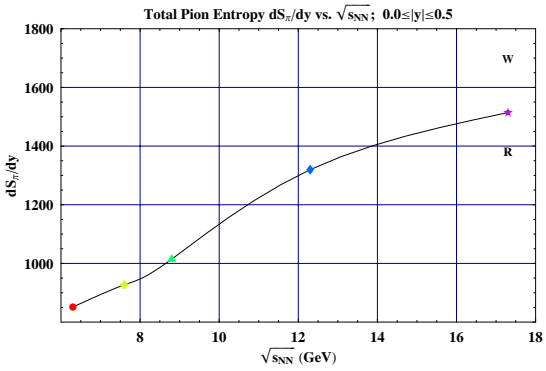

Figure 5.20-2. Total pion entropy dS_π/dy vs. $\sqrt{s_{NN}}$ for central Pb+Pb collisions (0-10% of σ_T) with $\mid y \mid$<0.5. Symbols: E_{Lab} = 158 GeV/A (star), 80 GeV/A (diamond), 40 GeV/A (triangle), 30 GeV/A (plus), 20 GeV/A (circle). The black curve is a spline fit. The "R" and "W" symbols are indications of the systematic errors implicit in the procedures used.

The next step in this program will be to use more recent NA49 HBT analysis and to compare the results with predictions from the quantum mechanical opacity calculations described in Sec. 5.19.

*See the NA49 web site at http://na49info.cern.ch/

[1] D. Ferenc, U. Heinz, B. Tomášik, U.A. Wiedemann, and J. G. Cramer, Phys. Letters B **457**, 347 (1999).

5.21 Pion entropy and phase space density in RHIC collisions

J. G. Cramer and the STAR HBT Physics Working Group*

The system entropy is of considerable interest in RHIC collisions because it is expected to be qualitatively larger for an initial quark gluon plasma than for an initial hadron gas. The average pion phase space density $\langle f \rangle$, estimated by combining the pion momentum spectrum and the HBT correlation function, can be used to estimate the entropy per particle S_π/N of the colliding system at freeze out. The relation for converting $f \equiv f(\vec{p}.\vec{r})$ to entropy per particle is:

$$S_\pi/N = \frac{\int [(f+1)\log(f+1) - f\log(f)]\, d\vec{r}\, d\vec{p}}{\int f\, d\vec{r}\, d\vec{p}} \qquad (1)$$

To make use of this relation, we assume that $f(\vec{p},\vec{r})$ is proportional to $\langle f \rangle$ and has the radial shape and radius momentum dependence given by the HBT analysis, and that the source is azimuthally symmetric. We then need the functional dependence of $\langle f \rangle$ with respect to p_T for all values of p_T, and for this we use fits to the pion spectra and corrected momentum volume. We perform the integrals of Eqn. 1 to obtain the entropy per particle S_π/N for each centrality. We obtain the total pion number by integrating the pion spectra and multiply this quantity by S_π/N for each centrality to obtain the total pion entropy dS_π/dy.

The STAR data from Au+Au collisions at $\sqrt{s_{NN}} = 130$ GeV has been analyzed with this technique and was reported last year. We have continued these studies of pion entropy and phase space density in RHIC collisions. Our present focus is to apply the opacity model described in Sec. 5.19 to the phase space density and entropy of the system and to compare the phase space density and entropy obtained from the above procedures with those of the model calculations. This work is in its initial stages, but shows promise of providing fresh insights into the mechanisms involved in RHIC collisions. In particular, we would like to gain better understanding of the relation between entropy production and chiral symmetry breaking in the evolution of RHIC collisions.

[1] See the HBT PWG web site at http://connery.star.bnl.gov/STAR/html/hbt_l

5.22 Review of particle identification for STAR-TPC

H. Bichsel

A review of "Particle identification with ionization measurements" has been written during the past year. It is being revised with the help of several colleagues.

The current version PIDN9ME.pdf can be accessed at

www.star.bnl.gov/∼bichsel/PIDN9MAR05.

6 Electronics, Computing, and Detector Infrastructure

6.1 Electronic equipment

G. C. Harper, A. W. Myers and T. D. Van Wechel

The electronics shop provided design and construction services of new laboratory electronic equipment, as well as maintenance and repair of existing CENPA electronics. The electronics shop supported ongoing efforts for SNO in Seattle as well as on-site support at Sudbury, Ontario, Canada.

Other projects undertaken by the electronics shop include the following:

1. The generating voltmeter (GVM) electronics were updated. The new design uses an integrated synchronous demodulatator to provide full wave rectification of the 800 Hz sine wave from the GVM stator. The rectified signal is filtered and buffered to drive the cable to the energy controller in the control room. The new design provides improved performance, especially at low terminal voltages, where the previous circuit was non-linear, and was blind to terminal voltages below about 160 kV.

2. A random rate pulse generator has been designed and constructed to be used in dead-time measurements of the SNO NCD data acquisition system. The principle of operation is based on the statistical probability of a random noise signal exceeding a given voltage level. The pulser consists of a random noise generator whose RMS voltage amplitude is regulated. A discriminator triggers a one-shot when the amplitude of the noise signal exceeds the level provided by the rate setpoint DAC. The level of the rate setpoint DAC, determines the mean rate of the output pulses. This unit outputs both a TTL and an amplitude settable negative output pulse. This pulser should also have uses for other experiments.

3. Additional stand-alone versions of the emiT charge sensitive preamplifiers have been constructed for use by the KATRIN and emiT experiments.

4. Updates have been made in the logic for the FPGA firmware of the SNO NCD GTID board, the ADC Shaper boards, and for the APOLLO Command Module board.

5. The characteristics of the analog electronic elements of the SNO NCD system string are presently being measured and analyzed.

6. New fiber optic (F/O) transmitter-receiver printed circuit boards were designed and built to replace the original boards of the F/O telemetry system on the injector deck.

7. The original speed control electronics, that utilized vacuum tubes and thyratrons, for the lathe in the main machine shop have been redesigned and replaced. The new circuit utilizes an op-amp driving a power MOSFET to set the field current of the lathe motor.

6.2 Improvements to the ORCA DAQ system

J. A. Detwiler, M. A. Howe, F. McGirt,[†] K. Rielage, J. F. Wilkerson and J. Wouters[†]

The Object-oriented Real-time Control and Acquisition (ORCA) system is an application software tool-kit that is designed for quickly building flexible data acquisition systems. In addition to being installed as the SNO NCD production DAQ system (see Sec. 2.10), ORCA is currently in use for several different development efforts including the KATRIN beta-decay experiment (see Sec. 2.13) and a small animal PET scanner at the University of Washington's Medical Imaging Lab. Since ORCA has been extensively described in past CENPA Annual Reports,[1] only the most recent developments will be described in this report.

Extensive profiling of ORCA was done to highlight bottlenecks in both the data readout and processing code that lead to a number of low-level code changes to optimize ORCA. Also, the user interface and data processing sections were separated into different threads to further improve performance. The data file format was redesigned to use an XML header and the raw data record format was changed to make it easier to design external analysis programs. A data explorer was implemented that can walk thru data files record by record and the plotting subsystem was enhanced to allow multiple data sets per plot with multiple regions of interest. Also, readout gates can now be defined for creating gated histograms.

A new driver was developed for the SBS/Bit3 810 PCI-to-VME interface card that is backward compatible with the older 617/62x series of cards. This allows ORCA to run on machines that only have PCI-X slots, such as the new Mac G5. Support was added for the industry standard M-Module carrier board, but the only M-Module that is currently supported is the M321 stepper motor controller. In addition, support was added for VME-based embedded CPUs, i.e. the Motorola MVE167. A general eCPU readout code was developed that is currently in use in the NCD experiment and can easily be expanded for the readout of any ORCA supported cards.

One big advance for ORCA was the development of a driver for a PCI-to-CAMAC interface. Software modules were developed for the following objects: CAMAC crate, PCI/CAMAC card, CC32 Crate adapter, Ortec AD413A, Ortec AD811 octal ADC, LeCroy 2249A integrating charge ADC, and the LeCroy 2551 12-channel Scaler. Work is progressing on code to support other cards, such as the XIA Digital Gamma Finder card.

We have also developed a cross-platform software framework, called "OrcaRoot", that interfaces ORCA with the ROOT analysis toolkit. OrcaRoot provides an object-oriented C++ framework for decoding an ORCA data stream via either a diskfile or a network socket and automatically writing the data records into a ROOT file, creating histograms, TTrees, or whatever the user desires, on-the-fly. This allows the data to be viewed immediately in the ROOT environment, providing users with extensive diagnostic and analysis capabilities. OrcaRoot is general enough to allow for more advanced processing as well, and can serve as the foundation of an online monitoring system, or even a full analysis framework.

[†]Los Alamos National Laboratory, Los Alamos, NM 87545.

[1]CENPA Annual Report, University of Washington (2001) p. 83; (2002) p. 81; (2003) p. 70; (2004) p. 66.

6.3 Laboratory computer systems

M. A. Howe, R. J. Seymour and J. F. Wilkerson

This year again saw continuous incremental upgrades or replacements of existing systems. Our expansion was focused on on-line disk storage, processor and operating system adjustments.

We have added two 64-bit dual-processor AMD Opteron systems. One is installed as a network-attached storage (NAS) 4 terabyte RAID system, the other is delegated as a compute server. Both are dedicated to the SNO collaboration.

The RAID system consists of sixteen 250 gigabyte SATA disks on two 8-port Adaptec hardware RAID cards. The cabinet can hold 24 disks, and is already equipped with a third RAID controller for easy expansion. The operating system is on a separate RAID 1 subsystem. Although we initially installed Red Hat Enterprise Linux 3 AS (RHEL3), that operating system's lack of official support for filesystems larger than 1 terabyte prompted us to quickly switch to Fedora Core 3 (FC3).

The dual-Opteron compute server also started as RHEL3, but application compatibility issues and the desire for a common platform caused us to eventually convert it to FC3 as well.

Our dual-processor 1 GHz Pentium III system was upgraded from Red Hat v7.3 to FC3.

As other desktop machines are added or replaced, our "standard issue" continues to be a $700 2.8 or 3.0 GHz generic Pentium Windows XP PC, frequently created as dual-boot with Fedora.

Our computing and analysis facility consists of:
- A mix of Linux systems, RedHat v7.3 through v9.0 and FC3
- Twin dual-processor DEC/Compaq/HP Unix AlpherServer 4000s
- Two VMS/Vaxes and two VMS Alphas for "legacy" computing.
- The SNO, NCD, KATRIN and emiT groups rely upon Macintosh systems.
- Our SunBlade 100 workstation serves CADENCE circuit design, analysis and layout duties.
- A VAXstation is the Linac and Vacuum systems' control and display system.
- Two desktop JAM acquisition and analysis systems, plus two laptops for taking to other installations.
- Although not directly used by Lab personnel, we provide co-location services for the Institute for Nuclear Theory and the Physics Nuclear Theory group in the form of one VMS Alphastation 500. The Astronomy Department has located a 64-processor Xeon-based Beowulf cluster in our machine room.

7 Accelerator and Ion Sources

7.1 Injector deck and ion sources

G. C. Harper, A. W. Myers, T. D. Van Wechel and D. I. Will

There was no new development for the terminal ion source. The Pyrex discharge bottle, Al canal, BN canal insulator, and o-rings were all replaced as required for standard servicing. After ten years of operation the RF oscillator tubes were found to be weak and unreliable. These two tubes were replaced. The source now runs at a lower pressure and with greater stability and reliability.

The fiber optic (F/O) telemetry system on the injector deck has been marginally reliable for the last several years. New F/O transmitter-receiver printed circuit boards (which implement the Hewlett Packard HFBR series F/O components) were designed and built. The ANAC 700 series ADC-DAC and interface units were retrofitted to house these boards. All of the glass infrared F/O cables were replaced with visible light, PiFax plastic fibers with HFBR compatible connectors. The new system is rugged, serviceable, reliable, and requires no alignment.

The sputter source was cleaned once this year. It has since operated for 27 days of molecular physics research by Professor Emeritus Robert Vandenbosch. Patterns of both production and breakup for molecular clusters of the general formula $Cs_iAl_jI_k$ (for total mass $\leq$ 540 amu) have been investigated and recorded. These ions are produced by using Cs to sputter pellets containing Al powder and either iodine or an iodide. After acceleration by the elevated injector deck, breakup occurs in our windowless gas target and analysis is via electrostatic deflector with a channeltron as the detector. Details of this technique were described previously.[1]

[1] R. Vandenbosch, D. I. Will, C. Cooper, B. Henry and J. F. Liang, Chem. Phys. Lett **274**, 112 (1997).

7.2 Van de Graaff accelerator operations and development

J. F. Amsbaugh, G. C. Harper, A. W. Myers, T. D. Van Wechel and D. I. Will

The tandem was entered eight times this year. The terminal ion source (TIS) and the foil stripper were exchanged during two openings as were spiral inclined field tube #3 and the KN straight tube. The electrostatic deflector supplies were either tested, repaired, or replaced during six tank openings. The machine was entered three times to change TIS ion species and change gradient. The RF source was serviced during two of the entries and the oscillator repaired during one of the entries.

Last year several problems with the TIS were related to failures in the electrostatic deflector high voltage power supplies. We installed a rugged power supply scheme using adequate transient suppression and potted power supplies. The new package has been in place and operational since September 2004.

A new GVM circuit utilizing a balanced demodulator was installed this year. The old circuit was linear down to about 165 kV where it zeroed and GVM regulation below that point was not possible. The new circuit is linear from 0 V to 10 MV. It has been used successfully with a 77 keV $^4He^+$ beam.

The x-rays produced in the spiral inclined field tube #1 region have been further localized. Two additional adjacent column planes were set to half value resistance. The tandem was at one time conditioned up to 8.5 MV this year. The tube continues to emit x-rays but the level has been substantially reduced.

During the 12 months from April 1, 2004 to March 31, 2005 the tandem pellet chains operated 805 hours, the SpIS 175 hours, and the DEIS 89 hours. Additional statistics of accelerator operations are given in Table 7.2-1.

ACTIVITY SCHEDULED	**DAYS SCHEDULED**	**PERCENT of AVAILABLE TIME**
Molecular research, deck ion sources only	27	7
Nuclear physics research, deck ion sources	1	1
Nuclear physics research, terminal ion source	80	22
Subtotal, molecular or nuclear physics research	108	30
Machine development, maintenance, or crew training	93	25
Grand total	201	55

Table 7.2-1. Tandem Accelerator Operations April 1, 2004 to March 31, 2005.

7.3 Safety and waste disposal

K. J. Higgins, E. P. Lemagie, D. I. Will and J. P. Will

During the past year one of us has taken Laboratory Safety Standard Compliance, and two have taken MYCHEM training for use of the new chemical inventory system, both courses offered by UW Environmental Health and Safety. Within CENPA thirteen individuals received instruction during twenty three individual and small group training sessions in aspects of safety, procedures, and waste disposal for fluoride, lanthanum, lithium, and solvents. The chemical inventory was completely updated.

During 2003 two of us were trained in shipping hazardous materials. In the past year three shipments of potentially hazardous material occurred. Two were properly labeled and documented. The third was eventually determined to be nonhazardous.[1]

Eight waste collection requests were submitted and picked up. These included 88 items weighing 2434 kg. The most significant items by weight were used lubricating and vacuum oils, remaining lead plating supplies, dead batteries, and exhausted circuit board etchant.[2]

[1]Thanks to Matt Moeller of UW Environmental Health and Safety (EH&S).

[2]Thanks to Erin McKeown, John Houck, Perris Dean, John Wallace, and Sheila Lockwood of UW EH&S.

8 The Career Development Organization: year five

M. K. Bacrania, T. Butler, M. L. Leber, N. S. Oblath and L. C. Stonehill,

The Career Development Organization for Physicists and Astronomers (CDO)[3] at the University of Washington is a graduate student organization that helps physics and astronomy students find employment after graduation. Historically, CENPA has been very well-represented in the CDO's membership and leadership. This year, the CDO President is once again a CENPA student and there are three new CDO members from CENPA. Building on previous years,[4] the CDO has organized the very successful Fourth Annual Networking Day event this year.

The Fourth Annual Networking Day was held on November 9th, 2004. The Networking Day provides opportunities for students to make contacts outside academia and to present their research to interested employers. The focus of Networking Day is on allowing the students to present their strengths, which is different from a typical job fair, where the employers are doing the majority of the presentation. This helps many companies that don't traditionally employ physicists to see the diverse skills that physics and astronomy students possess. As a result of this year's Networking Day, three job offers have been made to student presenters so far.

The CDO identified several goals for this year's Networking Day, including restructuring the lab tours to make them an integral part of the event, improving the quality of the student talks, increasing representation of national labs and local companies, and boosting undergraduate participation. By offering this year's lab tours right after lunch, we greatly increased the attendance, and we received very positive and enthusiastic feedback about the lab tours. We held two preparation sessions to help improve the quality of the student talks: a seminar on how to give a good job talk, and a mandatory practice session where presenters received feedback from each other on the effectiveness of their talk and presentation style. As a result of the improved student preparation, this year's talks were presented smoothly and directed to the right audience. The participation of national labs and local employers in Networking Day was increased this year, with nearly half of the 15 companies coming from Washington state and four labs represented, but we would like to continue to improve in this area next year. The one goal that we did not meet this year was to draw in more undergraduates: only two of the 22 student presenters were undergraduates. Next year we will emphasize internships as well as jobs, and we will work closely with the physics undergraduate advising office to attract more undergraduates to Networking Day.

This year, the CDO is also planning several career seminars, starting with a presentation about physics careers in medical imaging. The CDO has also been working to recruit new members and to gather ideas from a broader cross-section of the physics and astronomy students. In addition, the CDO is working to strengthen ties with the Department of Physics and the Visiting Committee, a group of alumni and others interested in the future path of the department.

[3] http://students.washington.edu/cdophys

[4] CENPA Annual Report, University of Washington, (2004) p. 72.

9 CENPA Personnel

9.1 Faculty

Eric G. Adelberger	Professor	
Hans Bichsel	Affiliate Professor	
John G. Cramer	Professor	
Peter J. Doe	Research Professor	
Hans Eggers[1]	Visiting Scholar	
Joseph Formaggio	Research Assistant Professor	
Alejandro Garcia	Professor	
Jens H. Gundlach	Research Associate Professor	
Isaac Halpern	Professor Emeritus	
Blayne R. Heckel	Professor	
R.G. Hamish Robertson	Professor;	Scientific Director
Kurt A. Snover	Research Professor	
Derek W. Storm	Research Professor;	Executive Director
Thomas A. Trainor	Research Professor	
Robert Vandenbosch	Professor Emeritus	
William G. Weitkamp	Professor Emeritus	
John F. Wilkerson	Professor	

9.2 Postdoctoral Research Associates

Cristina Bordeanu
Jason Detwiler
Chunhui Han[2]
Seth Hoedl
C.D. Hoyle
Sean McGee
Daniel Melconian
Keith Rielage
Stephan Schlamminger

[1]University of Stellenbosch, Victoria Street, 7600 Stellenbosch, South Africa.
[2]Presently at the City of Hope National Medical Center, 1500 E. Duarte Road, Duarte, CA 91010.

9.3 Predoctoral Research Associates

Minesh Bacrania
Ted Cook
Claire Cramer
Charles Duba
Charles Hagedorn
Dan Kapner
Michelle Leber
Kathryn Miknaitis
Hans Pieter Mumm[2]
Anne Sallaska
Christopher Spitzer
Matthew Swallows
Todd Wagner

Ki-Young Choi
G. Adam Cox
Rory Donovan[1]
William Clark Griffith[1]
Robert Johnson
Kareem Kazkaz
Frank Marcoline
Erik Mohrmann
Noah Oblath
Sky Sjue
Laura Stonehill
Smarajit Triambak
Brandon Wall

9.4 Research Experience for Undergraduates participants

Hal Finkel[3]
Van Nguyen[5]
Patrick Young[7]

Justin Lowrey[4]
Tabitha Spencer[6]

[1]Department of Physics, University of Washington, Seattle, WA 98195.
[2]Presently at NIST, 100 Bureau Drive, MS8461, Gaithersburg, MD 20899.
[3]Department of Physics, Drexel University, Philadelphia, PA 19104.
[4]Department of Physics, University of Texas, Austin, TX 78705.
[5]Department of Physics, San Diego State University, San Diego, CA 92105.
[6]Department of Physics, Ursinus College, Collegeville, PA 19426..
[7]Department of Physics, Linfield College, McMinnville, OR 97128.

9.5 Professional staff

The professional staff are listed with a description of their recent major efforts.

John F. Amsbaugh	Research Engineer	Mechanical design, vacuum systems
Tom H. Burritt	Research Engineer	Construction SNO NCD's
Gregory C. Harper	Research Engineer	Electronic and mechanical design Accelerator upgrades and operation
Mark A. Howe	Research Engineer	Software for DAQ, control systems
R. Jefferson Porter[1]	Visiting Staff	STAR analysis
Duncan J. Prindle, Ph.D.	Research Scientist	Heavy ion software
Richard J. Seymour	Computer Systems Manager	
H. Erik Swanson, Ph.D.	Research Physicist	Precision experimental equipment
Timothy D. Van Wechel	Electronics Engineer	Analog and digital electronics design
Brandon Wall[2]	Research Scientist- Engineer Assistant	SNO operation
Douglas I. Will	Research Engineer	Cryogenics, ion sources

9.6 Technical staff

James Elms	Instrument Maker
David Hyde	Instrument Maker
Allan Myers	Electronics Technician
Hendrik Simons	Instrument Maker, Shop Supervisor

9.7 Administrative staff

Barbara J. Fulton	Administrator
Kate J. Higgins	Fiscal Specialist

[1] 3233 210th St. Bothell, WA 98021.
[2] Graduate Student, CENPA.

9.8 Part Time Staff

Brian Allen
Ashley Batchelor
Owen Biesel
Jeremy Borden[1]
Rogan Carr[1]
David Crompton[1]
Suzanne Hayward
Gregory Hodges[1]
Emily Lemagie
Mara Lemagie [1]
Christy McKinley[1]
Kamil Michnicki
Jessica Mitchell
Michael Nickerson
Dejan Nikic
Braxton Osting[1]
Patrick Peplowski[1]
Shuji Uehara [1]
Mark Wehrenberg
Jonathan Will

[1]Left during 2004.

Published papers:

"Thoughts about nanodosimetry," H. Bichsel, Adv. Quantum Chem. **46**, 329 (2004).

"SNO II: Salt strikes back. An update from the Sudbury Neutrino Observatory," J. A. Formaggio, invited talk, *5th International Workshop on Neutrino Factories and Superbeams, NuFACT'03*, Columbia University, New York, NY, June, 2003, published in AIP Conference Proceedings, **721**, 183 (2004).

"Backgrounds to sensitive underground experiments," J. A. Formaggio and C. J. Martoff, Ann. Rev. Nucl. and Part. Sci. **54**, 361 (2004).

"Double beta decays and solar neutrinos with Mo-100," H. Ejiri and the MOON Collaborators,* Czech. J. Phys. **54**, B317 (2004).

"Sudbury Neutrino Observatory neutral current detector acquisition software overview," M. A. Howe, G. A. Cox, P. J. Harvey, F. McGirt, K. Rielage, J. F. Wilkerson and J. M. Wouters, *Proceedings of IEEE Nuclear Science Symposium and Medical Imaging Conference (NCC-MIC) 2003*, Portland, OR, October, 2003, published in IEEE Transactions on Nucl. Sci. **51**, (3) 878 (2004).

"Sudbury Neutrino Observatory neutral current detectors signal readout system," G. A. Cox and the SNO Collaborators,* *Proceedings of IEEE Nuclear Science Symposium and Medical Imaging Conference (NCC-MIC) 2003*, Portland, OR, October, 2003, published in IEEE Trans. Nucl. Sci. **51**, 2227 (2004).

"New determination of the ^{7}Be$(p,\gamma)^8$B S-factor," A. R. Junghans, E. C. Mohrmann, K. A. Snover, T. D. Steiger, E. G. Adelberger, J. M. Casandjian, H. E. Swanson, L. Buchmann, A. M. Laird, S. H. Park and A. Zyuzin, Nucl. Phys. A **746**, 210c (2004).

"Weak interactions and fundamental symmetries with rare isotopes," A. García, Nucl. Phys. A **746**, 298c (2004).

"Search for the ^{8}B$(2^+) \rightarrow {}^8$Be(0^+) ground-state transition," M. K. Bacrania, D. W. Storm and R. G. H. Robertson, Nucl. Phys. A **746**, 463c (2004).

"The new Seattle-TRIUMF ^{7}Be$(p,\gamma)^8$B S-factor determination," A. R. Junghans, E. C. Mohrmann, K. A. Snover, T. D. Steiger, E. G. Adelberger, J. M. Casandjian, H. E. Swanson, L. Buchmann, A. M. Laird, S. H. Park and A. Zyuzin, Nucl. Phys. B **138**, 112 (2005).

"Spectroscopy of low energy solar neutrinos by MOON: Mo Observatory Of Neutrinos," R. Hazama and the MOON Collaborators,* Nucl. Phys. Proc. Suppl. **138**, 102 (2005).

"The proposed Majorana Ge-76 double-beta decay experiment," C. E. Aalseth and the Majorana Collaborators,* Nucl. Phys. Proc. Suppl. **138**, 217 (2005).

"MOON (Mo Observatory Of Neutrinos) for double beta decay," M. Nomachi and the

Moon Collaborators,* Nucl. Phys. Proc. Suppl. **138**, 221 (2005).

"Pion entropy and phase space density in RHIC collisions," J. G. Cramer and the STAR Collaborators,* *Proceedings of the 2nd Warsaw Meeting on Particle Correlations and Resonances in Heavy Ion Collisions*, October 2003, Warsaw, Poland, published in Nukleonika **29**, Supp. 2, S41 (2004).

"The Majorana neutrinoless double-beta decay experiment," C. E. Aalseth and the Majorana Collaborators,* Phys. Atom. Nucl. **67**, 2002 (2004), [Yad. Fiz. **67**, 2025 (2004)].

"Kaon production and kaon to pion ratio in Au + Au collisions at $\sqrt{s_{NN}} = 130$ GeV," C. Adler and the STAR Collaborators,* Phys. Lett. B **595**, 143 (2004), (nucl-ex/0206008).

"Solar neutrinos from CNO electron capture," L. C. Stonehill, J. A. Formaggio and R. G. H. Robertson, Phys. Rev. C **69**, 015801 (2004) (hep-ph/0309266).

"Production of e+e- pairs accompanied by nuclear dissociation in ultra-peripheral heavy ion collision," J. Adams and the STAR Collaborators,* Phys. Rev. C **70**, 031902 (2004).

'Transverse momentum fluctuations in nuclear collisions at 158 AGeV," T. Anticic and the NA49 Collaborators,* Phys. Rev. C **70**, 034902 (2004), (hep-ex/0311009).

"Comment on 'Electromagnetic dissociation of ^{8}B and the astrophysical S-factor for ^{7}Be$(p,\gamma)^8$B'," K. A. Snover, A. R. Junghans and E. C. Mohrmann, Phys. Rev. C **70**, 039801 (2004).

"Rapidity and centrality dependence of proton and anti-proton production from Au-197 + Au-197 collisions at $\sqrt{s_{NN}} = 130$-GeV," J. Adams and the STAR Collaborators,* Phys. Rev. C **70**, 041901 (2004), (nucl-ex/0306029).

"Photon and neutral pion production in Au+Au collisions at $\sqrt{s_{NN}} = 130$ GeV," J. Adams and STAR Collaborators,* Phys. Rev. C **70**, 0401008 (2004), (nucl-ex/0401008).

"Centrality and pseudorapidity dependence of charged hadron production at intermediate P_T in Au+Au collisions at $\sqrt{s_{NN}} = 130$ GeV," J. Adams and the STAR Collaborators,* Phys. Rev. C **70**, 044901 (2004), (nucl-ex/0404020).

"Measurements of transverse energy distributions in Au+Au collisions at $\sqrt{s_{NN}} = 200$ GeV," J. Adams and STAR Collaborators,* Phys. Rev. C **70**, 054907 (2004).

"Pseudorapidity asymmetry and centrality dependence of charged hadron spectra in d+Au Collisions at $\sqrt{s_{NN}} = 200$ GeV," J. Adams and the STAR Collaborators,* Phys. Rev. C **70**, 064907 (2004).

"Transverse-momentum dependent modification of dynamic texture in central Au+Au collisions at $\sqrt{s_{NN}} = 200$ GeV," J. Adams and the STAR Collaborators,* Phys. Rev. C **71**, 031901 (2004).

"Submillimeter tests of the gravitational inverse-square law," C. D. Hoyle, D. J. Kapner,

B. R. Heckel, E. G. Adelberger, J. H. Gundlach, U. Schmidt and H. E. Swanson, Phys. Rev. D **70**, 042004 (2004).

"Electron Antineutrino Search at the Sudbury Neutrino Observatory," B. Aharmim and the SNO Collaborators,* Phys. Rev. D **70**, 093014 (2004), (hep-ex/ 0407029).

"Constraints on nucleon decay via 'invisible' modes from the Sudbury Neutrino Observatory," S. N. Ahmed and the SNO Collaborators,* Phys. Rev. Lett. **92**, 102004 (2004), (hep-ex/0310030).

"Cross sections and transverse single-spin asymmetries in forward neutral pion production from proton collisions at $\sqrt{s}$ = 200-GeV," J. Adams and the STAR Collaborators,* Phys. Rev. Lett. **92**, 171801 (2004), (hep-ex/0310058).

"Measurement of the total active ^{8}B solar neutrino flux at the Sudbury Neutrino Observatory with enhanced neutral current sensitivity," S. N. Ahmed and the SNO Collaborators,* Phys. Rev. Lett. **92**, 181301 (2004), (nucl-ex/0309004).

"Multi-strange baryon production in Au-Au collisions at $\sqrt{s_{NN}}$ = 130 GeV," J. Adams and the STAR Collaborators,* Phys. Rev. Lett. **92**, 182301 (2004), (nucl-ex/0307024).

"Azimuthally sensitive HBT in Au+Au collisions at $\sqrt{s_{NN}}$ = 200 GeV," J. Adams and the STAR Collaborators,* Phys. Rev. Lett. **93**, 012301 (2004), (nucl-ex/0312009).

"Lambda and anti-lambda production in central Pb-Pb collisions at 40-A GeV, 80-A GeV and 158-A GeV," T. Anticic and the NA49 Collaborators,* Phys. Rev. Lett. **93**, 022302 (2004), (nucl-ex/0311024).

"Azimuthal anisotropy and correlations at large transverse momenta in p+p and Au+Au collisions at $\sqrt{s_{NN}}$ = 200 GeV," J. Adams and the STAR Collaborators,* Phys. Rev. Lett. **93**, 252301 (2004).

"Reconciling Coulomb dissociation and radiative capture experiments," H. Esbensen, G. F. Bertsch and K. A. Snover, Phys. Rev. Lett. **94**, 042502 (2005).

"Open charm yields in d+Au collisions at $\sqrt{s_{NN}}$ = 200 GeV," J. Adams and the STAR Collaborators,* Phys. Rev. Lett. **94**, 062301 (2005).

"Quantum opacity, the RHIC HBT puzzle, and the chiral phase transition," J. G. Cramer, G. A. Miller, J. M. S. Wu and J-H. Yoon, Phys. Rev. Lett. **94**, 102302 (2005).

"Testing the gravitational inverse-square law, E. Adelberger, B. Heckel and C. D. Hoyle, Phys. World **18**, 41 (2005).

"emiT: An apparatus to test time-reversal invariance in polarized neutron decay," H. P. Mumm, A. Garcia, L. Grout, M. Howe, L. P. Parazzoli, R. G. H. Robertson, K. M. Sundqvist, J. F. Wilkerson, S. J. Freedman, B. K. Fujikawa, L. J. Lising, M. S. Dewey, J. S. Nico, A. K. Thompson, T. E. Chupp, R. L. Cooper, K. P. Coulter, S. R. Hwang, R. C. Welsh, L. J. Broussard, C. A. Trull, F. E. Wietfeldt and G. L. Jones, Rev. Sci. Instrum.

75, 5343 (2004).

Papers submitted or to be published 2005:

"Phi meson production in Au+Au and p+p collisions at $\sqrt{s_{NN}}$ =200 GeV," J. Adams and the STAR Collaborators,* to be published in Phys. Lett. B.

"Azimuthal anisotropy in Au+Au collisions at $\sqrt{s_{NN}}$ = 200 GeV," J. Adams and the STAR Collaborators,* submitted to Phys. Rev. C, (nucl-ex/0409033).

"Electron energy spectra, fluxes, and day-night asymmetries of ^{8}B solar neutrinos from the 391-day salt phase SNO data set," B. Aharmim and the SNO Collaborators,* submitted to Phys. Rev. C, (nucl-ex/0502021).

"Pion interferometry in Au+Au collisions at $\sqrt{s_{NN}}$ = 200 GeV," J. Adams and the STAR Collaborators,* submitted to Phys. Rev. C, (nucl-ex/0411036).

"K(892)* resonance production in Au+Au and p+p ccollisions at $\sqrt{s_{NN}}$ = 200 GeV at STAR," J. Adams and the STAR Collaborators,* accepted by Phys. Rev. C for publication, (nucl-ex/0412019).

"Two-particle correlations on transverse momentum and minijet dissipation in Au-Au collisions at $\sqrt{s_{NN}}$ = 130 GeV," J. Adams and the STAR Collaborators,* submitted to Phys. Rev. Lett., (nucl-ex/0408012).

"Hadronization geometry and charge-dependent number autocorrelations on axial momentum space in Au-Au collisions at $\sqrt{s_{NN}}$ = 130 GeV," J. Adams and the STAR Collaborators,* submitted to Phys. Rev. Lett., (nucl-ex/0406035).

"Production of e^+e^- pairs accompanied by nuclear dissociation in ultra-peripheral heavy ion collision," J. Adams and the STAR Collaborators,* submitted to Phys. Rev. Lett., (nucl-ex/0404012).

"Multiplicity and pseudorapidity distributions of photons in Au + Au collisions at $\sqrt{s_{NN}}$ = 62.4 GeV," J. Adams and the STAR Collaborators,* submitted to Phys. Rev. Lett., (nucl-ex/0502008).

"Minijet deformation and charge-independent two-particle correlations on momentum subspace (eta,phi) in Au-Au collisions at $\sqrt{s_{NN}}$ = 130 GeV," J. Adams and the STAR Collaborators,* submitted to Phys. Rev. Lett., (nucl-ex/0411003).

"Distributions of charged hadrons associated with high transverse momentum particles in pp and Au+Au Collisions at $\sqrt{s_{NN}}$ = 200 GeV," J. Adams and the STAR Collaborators,* submitted to Phys. Rev. Lett., (nucl-ex/0501016).

"Rapidity and centrality dependence of proton and anti-proton production from Au+Au collisions at $\sqrt{s_{NN}}$ = 130 GeV," STAR Collaborators,* submitted to Phys. Rev. Lett.,

(nucl-ex/0306029).

"Conceptual design for a Deep Underground Science and Engineering Laboratory Cascades," W. Haxton, J. Wilkerson, R. A. Robertson and R. J. Guardia, accepted paper, *2005 Rapid Excavation and Tunneling Conference*, to be published.

9.9 Invited talks, abstracts and other conference presentations:

"A place in the Sun for the neutrino," R. G. H. Robertson, Invited talk, Stuart Freedman Festschrift, University of California, Berkeley, CA, Jan. 2004.

"Where do we find SNO in April?" R. G. H. Robertson, Invited talk, Kuniharu Kubodera Festschrift, University of South Carolina, Columbia, SC, April 2004.

"A Li-based detector for solar neutrinos," R. G. H. Robertson, Invited presentation, Solar Neutrino Working Group Meeting of the APS, Princeton, NJ, April 2004.

"Time reversal violation in neutron beta decay: The emiT experiment," J. F. Wilkerson, Invited talk, *Precision Measurements with Slow Neutrons*, National Institute of Science and Technology, Gaithersburg, MD, April 2004.

"Tests of Newton's Inverse-Square Law: Probing the true geometry of the universe," E. G. Adelberger, Plenary talk, American Physical Society, Denver, Colorado, April 2004, Bull. Am. Phys. Soc. **49**, No. 2, 24 (2004), Session A1.

"Torsion balance tests of gravity and other small forces at short distances," J. H. Gundlach, Invited talk, American Physical Society, Denver, Colorado, April 2004, Bull. Am. Phys. Soc. **49**, No. 2, 30 (2004), Session B9.

"Measurement of the day-night effect in the salt phase of SNO," K. Miknaitis, American Physical Society, Denver, Colorado, April 2004, Bull. Am. Phys. Soc. **49**, No. 2, 32 (2004) Session B10.

"The emiT experiment: A search for time reversal invariance violation in polarized neutron beta decay," H. P. Mumm, American Physical Society, Denver, Colorado, April 2004, Bull. Am. Phys. Soc. **49**, No. 2, 46 (2004) Session D2 4.

"Short-range tests of Newton's Inverse Square Law," D. Kapner, American Physical Society, Denver, Colorado, April 2004, Bull. Am. Phys. Soc. **49**, No. 2, 53 (2004) Session D9.

"Weak Equivalence Principle Tests using a rotating torsion balance," K.-Y. Choi and the EotWash Collaboration, American Physical Society, Denver, Colorado, April 2004, Bull. Am. Phys. Soc. **49**, No. 2, 53 (2004) Session D9 5.

"Data acquisition system for the NCDs at SNO," G. A. Cox, American Physical Society, Denver, Colorado, April 2004, Bull. Am. Phys. Soc. **49**, No. 2, 175 (2004) Session W9 5.

"Initial data from the SNO NCD array," L. C. Stonehill, American Physical Society, Denver, Colorado, April 2004, Bull. Am. Phys. Soc. **49**, No. 2, 175 (2004) Session W9 6.

"The decade of the neutrinos," J. A. Formaggio, *APS Northwest Meeting, 2004*, Moscow, ID, May 2004.

"Does Galactic matter obey the equivalence principle?" S. Schlamminger, *APS Northwest Meeting, 2004*, Moscow, ID, May 2004.

"The Sudbury Neutrino Observatory," J. F. Wilkerson, Invited Plenary Talk, *Neutrino 2004*, Paris, France, June 2004.

"Installation and operation of the SNO neutral current detector array," J. Heise, S. McGee and K. Rielage Poster presentation, *Neutrino 2004*, Paris, France, June 2004.

"Muons in SNO," J. A. Formaggio, *Neutrino 2004*, Paris, France, June 2004.

"The Majorana experiment: A search for neutrinoless double-beta decay," K. Kazkaz, *Neutrino 2004*, Paris, France, June 2004.

"Measurement of the day-night effect in the salt phase of SNO," K. K. S. Miknaitis, *Neutrino 2004*, Paris, France, June 2004.

"The physics of SNO," J. A. Formaggio, *Aspen Neutrino Workshop, 2004*, Aspen, CO, July 2004.

"The ^{7}Be(p,γ)^{8}B astrophysical S-factor," K. A. Snover, A. R. Junghans, E. C. Mohrmann, T. D. Steiger, E. G. Adelberger, J. M. Casandjian, H. E. Swanson, L. Buchmann, S. H. Park, A. Zyuzin and A. M. Laird, *Proceedings of the 8th Nuclei in the Cosmos Conference*, July 2004, Vancouver, BC, Nucl. Phys. A, to be published.

"Direct neutrino mass measurement at the Karslruhe Tritium Neutrino Experiment (KATRIN)," S. McGee, *Proceedings of the 8th Nuclei in the Cosmos Conference*, July 2004, Vancouver, BC, Nucl. Phys. A, to be published.

"The neutrino programs at Sudbury and Seattle" and "Status of the KATRIN tritium beta decay experiment," P. J. Doe, *Asian Pacific Workshop on Neutrinos in Nuclear Physics 2004*, Osaka University, Laboratory of Nuclear Studies, Osaka, Japan, July 2004.

"Neutrinoless double beta-decay Working Group Update," J. R. Wilkerson, *Deep Underground Science and Engineering Meeting*, Berkeley, CA, August 2004.

"Solar neutrino physics and SNO," J. F. Wilkerson, Invited Lecture, at the *DPG Summer School on Neutrino Physics: from the Laboratory to the Cosmos*, Bad Honnef, Germany, September 2004.

"Deep Underground Science and Engineering Laboratory - Cascades," J. F. Wilkerson, *Invited Presentation and Roundtable Discussion*, Community Stakeholders Group, Leavenworth, WA, October 2004.

"National Underground Science and Engineering Laboratory," J. W. Wilkerson, Invited Presentation, *Wenatchee Chapter of the Washington Society of Professional Engineers*, Wenatchee, WA, November 2004.

"How many spatial dimensions does the Universe have–really?" E. G. Adelberger, public "Einstein Year" Lecture, University of Kentucky, Lexington, KT February 2005.

"Fragmentation of the molecular cluster C-60." Invited talk, R. Vandenbosch, *American Chemical Society Meeting*, San Diego, CA, March 2005.

*UW collaborators for the various CENPA research groups are listed below (April 1, 2004 - March 31, 2005):

KATRIN: P. J. Doe, J. A. Formaggio, M. Leber, S. McGee, K. Rielage, R. G. H. Robertson and J. F. Wilkerson

Majorana: J. A. Detwiler, P. J. Doe, J. A. Formaggio, K. Kazkaz, M. G. Marino, S. McGee, R. G. H. Robertson and J. F. Wilkerson

Moon: P. J. Doe, R. G. H. Robertson and J. F. Wilkerson

RHIC: H. Bichsel, J. G. Cramer and T. A. Trainor

SNO: G. A. Cox, J. A. Detwiler, P. J. Doe, C. A. Duba, J. A. Formaggio, S. McGee, K. K. S. Miknaitis, N. S. Oblath, K. Rielage, R. G. H. Robertson, L. C. Stonehill, B. L. Wall and J. F. Wilkerson

9.10 Degrees Granted, Academic Year, 2004-2005

A Test of Time Reversal Violation in Neutron Beta Decay, Hans Pieter Mumm (2004).

Limiting CP Violation Through a Search for a Permanent Electric Dipole Moment of Mercury 199 Atoms, William Clark Griffith (2005).